Development and validation of an X-ray model for an Elekta Precise multileaf collimator to be used in Monte Carlo dose calculations

By

Jacobus Johannes Lodewikus Smit

Thesis submitted to comply with the requirements for the MMedSc degree in the Faculty of Health Sciences, Medical Physics Department, at the University of the Free State, South Africa

UNIVERSITY OF THE FREE STATE
UNIVERSITEIT VAN DIE VRYSTAAT
YUNIVESITHI YA FREISTATA

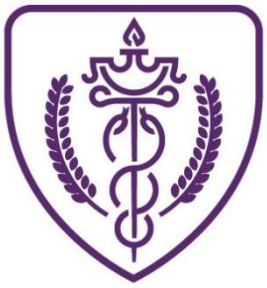

January 2015

Study leader: Dr FCP du Plessis

Table of contents

Chapter 3 - Materials & Methods

List of abbreviations

2D	Two dimensions
3D	Three dimensions
AAA	Anisotropical analytical algorithm
BEV	Beam-eye-view
CAX	Central beam axis
CDF	Cumulative density function
CH	Condensed history
CRT	Conformal radiation therapy
CSDA	Continuously slowing down approximation
CT	Computed tomography
d_{max}	Depth of maximum dose
dpi	dots per inch
ECUT	Electron cut-off energy
EE	Electron equilibrium
FS	Field size
FWHM	Full width at half maximum
GUI	Graphical user interface
IMRT	Intensity-modulated radiation therapy
LEE	Lateral electron equilibrium
Linac	Linear accelerator

LS	Least square
MC	Monte Carlo
MLC’s	Multileaf collimators
MeV	Mega electron volt
MU	Monitor unit
MV	Megavolt
OF	Output factor
PCUT	Photon cut-off energy
PDD	Percentage depth dose
PDF	Probability density function
QA	Quality assurance
RNG	Random number generator
ROI	Region of interest
RT	Radiation therapy
SS	Step-and-shoot
SSD	Source-to-surface distance
SW	Sliding window
TPS	Treatment planning system
VMAT	Volumetric-modulated arc therapy
WT	Water tank

Chapter 1 – Introduction

The discovery of X-rays in 1895 by Wilhelm Röntgen created worldwide excitement in the development of machines to use X-rays for diagnostic, as well as for treatment of cancer, purposes[1]. Radiation therapy (RT) machines or linear accelerators (Linac's) and radiation dose delivering methods have steadily improved over the decades. Advances in computer technology and radiation physics during the 1970's made it possible to apply radiation more precisely. With the use of computed tomography (CT) images to construct a patient model the tumor's location can be accurately mapped in three-dimensions (3D). Radiation beams are shaped to the geometry of the tumor and are delivered from several directions. This type of treatment is known as conformal radiation therapy (CRT)[2]. Later, with the advancements in computing developments and software, each beam's intensity was modified to the size and depth of the tumor. This type of treatment is called intensity-modulated radiation therapy (IMRT) and is used more commonly[3]. Volumetric-modulated arc therapy (VMAT) is a next generation RT technique that delivers the treatment dose in uninterrupted arc(s) around the patient, thus reducing treatment delivery times compared to CRT and IMRT[4].

1.1: Intensity-Modulated Radiation Therapy (IMRT)

The modulated intensity of the RT beams has the potential to spare adjoining normal tissue to a greater extent compared to CRT, due to high dose gradients that are achieved. Because of this, in principle, an increased dose of radiation can be delivered to the tumor. In order to produce and shape these IMRT beams, multileaf collimators (MLC's) are used to conform the photon beam onto the tumor and shield normal tissue during treatment[5].

1.2: Multileaf Collimators (MLC's)

MLC's are computer-controlled and constructed out of high density tungsten alloy leaves. To produce the IMRT and VMAT beams, each leaf's position is determined using an inverse planning dose calculation algorithm and a leaf sequencer algorithm. During radiation treatment, the MLC's move to create different intensities of photon fluence within the tumor in order for the whole tumor to be irradiated at different gantry angles. A much higher radiation dose may be given to a tumor volume using this technique[6]. However, during IMRT the dose to normal surrounding tissue also increases. The spread of low doses to normal tissue is an ongoing struggle. Using step-and-shoot (SS) IMRT delivery mode, the MLC leaf positions are fixed for each segment, and for the next segment the leaf positions change. With sliding window (SW) IMRT and VMAT delivery modes, the leaf positions continuously adjust during treatment delivery[7]. The gantry rotates at various speeds during VMAT, while the gantry stays fixed at predetermined positions while delivering radiation during SS and SW modes. In order to determine or calculate the absorbed dose to the tumor, various algorithms exist, i.e. anisotropic analytical algorithm (AAA), convolution/superposition, collapsed-cone and Monte Carlo (MC)[8]. Electron equilibrium (EE) breakdown causes inaccuracy in analytical dose calculation in heterogeneous media. This is due to lack of secondary electron transport modelling that can be handled with MC[9]. Dose calculation methods based on energy deposition kernels, point spread functions and pencil beams used in convolution/superposition methods also have limitations in the absence of EE[10,11,12,13,14]. The AAA, a 3D pencil beam convolution/superposition dose calculation model, is based on MC generated kernels[15]. Fogliata *et al*[16] benchmarked AAA dose calculations against measured data. The largest discrepancies were found in small photon fields with a wedge included. The collapsed cone convolution algorithm is inaccurate in regions where EE is absent. EE breakdown occurs for dose calculations involving small fields in close vicinity lung/soft tissue and bone/soft tissue interfaces[17].

1.3: Monte Carlo (MC) Simulations

MC simulation methods are regarded as the golden standard for dose calculations[18]. MC simulations replicate individual particle tracks using random numbers and absorption cross-sections to sample dynamic variables from probability density functions[19]. The physical laws required for these simulations are well known, and our computer resources are capable of performing the simulations in a manageable and practical time frame. Thus, MC based radiation transport is best suited to perform absorbed dose calculations. Several MC codes exist for dose calculations, e.g. GATE, FLUKA, IDEAL-DOSE, PENELOPE, BrachyDose, BEAMnrc and DOSXYZnrc.

The GATE (**G**eant4 **A**pplication for **T**omographic **E**mission) code is based on the general purpose GEANT4 toolkit for applications in external beam nuclear medicine, RT, brachytherapy, intraoperative RT, hadrontherapy and *in vivo* dose monitoring[20]. FLUKA (**FLU**ktuierende **KA**skade) is a general purpose code for particle interaction and transport for radiation protection studies at high energy accelerators[21]. The IDEAL-DOSE code is used for microdosimetry[22]. PENELOPE (**P**enetration and **ENE**rgy **LO**ss of **P**ositrons and **E**lectrons) is a general purpose code for coupled electron-photon transport simulation in arbitrary materials and complex quadric geometries[23]. The BrachyDose, BEAMnrc and DOSXYZnrc codes are based on the EGSnrc (**E**lectron **G**amma **S**hower) code system. BrachyDose is used for brachytherapy sources dosimetry[24]. BEAMnrc is used for modeling RT sources, i.e. Linac's and kilovoltage units[25,26]. DOSXYZnrc is used for 3D dose calculation[27]. The EGSnrc code system is the package for the simulation of coupled electron-photon transport based on MC method. EGSnrc incorporates the implementation of the condensed history technique for charged particle transport simulation and accurate low energy cross sections. EGSnrc is an improved and extended version of the older EGS4 and original EGS packages which were developed at Stanford Linear Accelerator Center (SLAC)[28].

Tyagi *et al* used MC simulations to model the geometry of 120 leaf MLC's for IMRT purposes for a Varian™ 21 EX (Varian Medical Systems, Palo Alto, CA, USA) Linac[29]. Dosimetric comparisons

were made to homogeneous phantom geometry measurements under different IMRT delivery circumstances. Sikora *et al* also used MC simulations to create a virtual source model of a mini MLC of an Elekta Beam Modulator™ (Elekta Oncology Systems, Crawley, UK) for intensity modulated radiosurgery treatments[30]. Both achieved overall agreement results within 2% / 2mm Gamma index evaluation.

1.4: Source Modelling

Virtual source models consist of analytical equations to replicate the photons' energy spectrum and fluence generated from the Linac treatment head[31,32]. An advantage of virtual source models is that it reduced simulation time in order to achieve faster results. The disadvantage in achieving faster results can be that important scatter is missing for accurate dose distributions. Multiple-sources are mostly used in source models, as the components in the treatment head increases the complexity of the models. Single target source models usually fail to compensate for scattered photons that are generated by the various components in the head, as the findings by Yan *et al*[33] show. They compared three different source models with diode array measurements in order to find an appropriate head scatter source model for fast and accurate planar dose calculations for IMRT. They found the best agreement using the two-source model (primary target point source and flattening filter extra-focal source) in comparison to the three-source model (primary target point source, primary collimator and flattening filter extra-focal sources) and single-source model (target point source). The three-source and single-source models underestimated head scatter for various symmetric rectangular and asymmetric fields. Measured-driven models, where the development of models are derived solely from measurements, will be used in this study[34].

Fluence source models are also found in treatment planning systems (TPS), such as Varian's Eclipse™, Elekta's XiO® and Monaco®, in order for the algorithms to calculate the absorbed dose as accurately as possible to a Linac's commissioned data[35].

1.5: GAFCHROMIC® EBT2 film

GAFCHROMIC® EBT2 film (International Specialty Products, Wayne, NJ, USA) is a radiochromic film which has been developed specifically for dosimetry purposes in the RT environment[36].

EBT2 film is self-developing, thus requires no post-exposure chemical processing in a darkroom; can easily be handled under interior light exposures; can be cut into smaller pieces of any shape; its composition is nearly tissue equivalent; is energy independent and can be immersed in water phantoms for hours due to its water resistant properties. The film is widely used for quality assurance (QA) purposes, whether for depth-dose and profile data acquisition or IMRT treatment plan verification[37,38]. The film can be scanned using commercial document scanners and analyzed by using imaging processing software. This film will be used to acquire dose data for MLC-shapes in RW3 (PTW, Freiburg, Germany) water equivalent material.

1.6: Aim of study

The aim of this research project is to continue the development of a suitable MC photon source model for the Elekta^{TM} Precise Linac for IMRT verification and QA purposes, and to validate the model to film and water tank measurements. In order to achieve this, the following objectives are listed:

(1) To set up a GAFCHROMIC® EBT2 film calibration procedure since it is going to be used to measure irregular MLC-collimated photon fluence maps produced by the Linac.

(2) To modify the MC photon source model of the MLC Linac where necessary.

(3) To compare water tank dose measurement profiles produced by the Linac with MC simulated dose data for single regular and irregular MLC shaped fields.

Chapter 2 – Theory

2.1: Physical Linac Head Configuration

The accelerated particles in a photon radiation treatment Linac are electrons. Electrons are injected by an electron gun into a special waveguide, and are accelerated there by the local electric field component of microwaves. It is steered and focused by electro-magnetic coils to get a narrow electron beam that hits a thin target, which is generally a tungsten alloy. The collision of the electron beam with this target generates Bremsstrahlung photons. Due to the megavolt energy, the beam is directed into the forward direction. Fig. 2.1 shows the configuration of components inside the treatment head of an Elekta™ Precise Linac, according to the IEC 60601 standards[39].

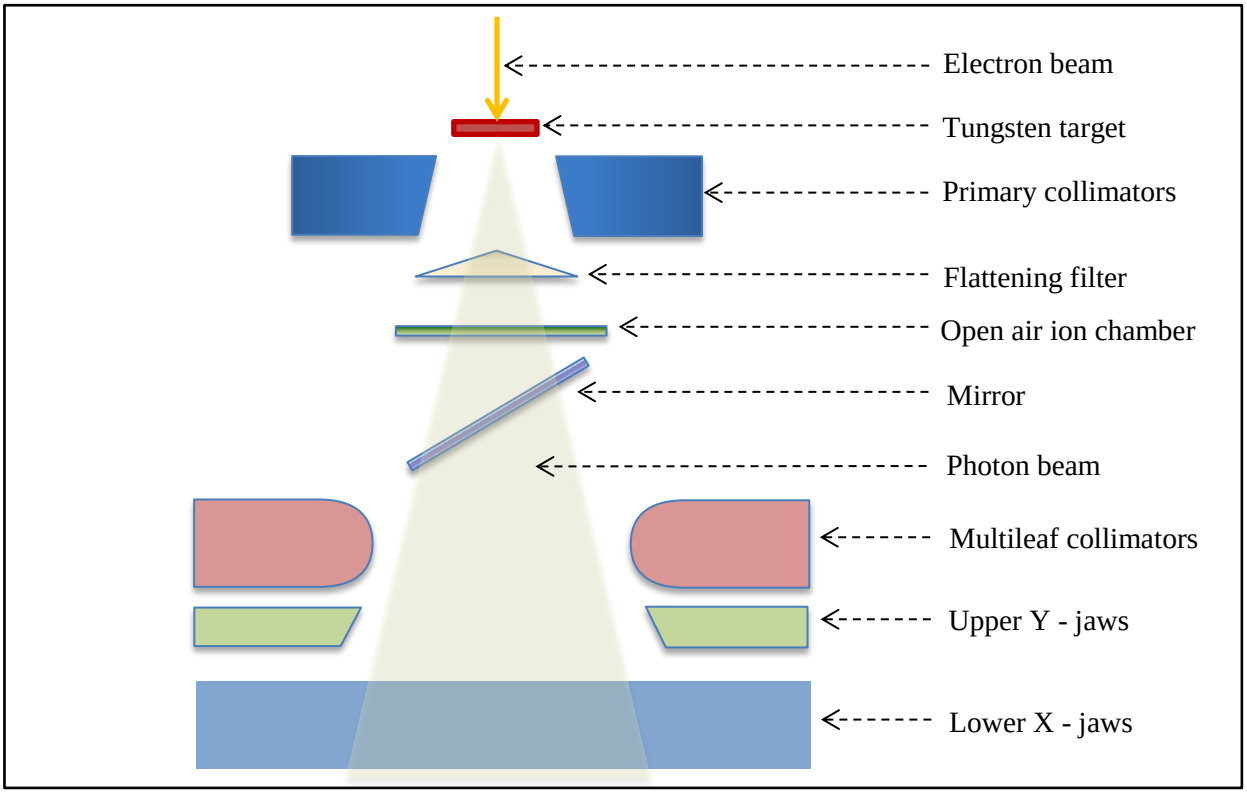

Fig. 2.1: Head configuration for an Elekta™ Precise Linear accelerator (Linac) according to IEC 60601.

The photon fluence from the target is initially truncated by the primary collimator into a circular shape and field. It is then attenuated by a flattening filter, which is thicker on the central beam axis (CAX) and thinner at larger radii. This shape creates a uniform photon fluence distribution at about 10 cm depth in water. The field of the photon fluence is further defined by secondary collimators, e.g. the jaws which are thick metal slabs. MLC's are finer instrumented leaf-like collimators. They are both manufactured from a tungsten, nickel and cobalt alloy. The photon beam also interacts with the air along its path to the patient surface, which generates contamination electrons that contribute to surface dose.

All the particles can be obtained through an accurate simulation of the Linac head in the BEAMnrc MC code. This, however, takes additional time to obtain phase space data for further simulation in the DOSXYZnrc code. In a phase space, every parameter or variable of the system is represented as an axis of a multidimensional space[40]. The variables of particles simulated include the charge, energy, direction of the path and the position of the particles. This is where the power of a representative source model lies which forms the heart of this research project. We would like to replicate the actual photon beam, with its contamination electrons, to be able to model an Elekta^{TM} Precise Linac. The source model that is going to be developed and studied will take each exposed component in the Linac head (Fig. 2.1) into account.

2.2: Source Modelling

The source model of the Elekta^{TM} Precise Linac head consists of mathematical equations in order to replicate the photons' energy spectrum and fluence field for various photon energy beams produced by the machine. An additional energy spectrum and fluence for contaminated electrons is used for proper surface dose simulations. The development of the source model was initiated by retired Prof. Casper

Willemse, who made it available for us to continue the development of the model in order to use it for QA and patient verification purposes.

2.2.1: Photon energy spectrum

The photon energy spectrum, $\Phi_p(E,r)$, in the model is based on the modified Schiff formula[41,42] and is a function of beam energy (E) and off-axis distance (r). It has a dependency on the shape of the flattening filter in the off-axis direction due to beam softening. The photon energy spectrum is shown in Eq. 1.

$$\Phi_p(E,r) = \frac{1}{E}\left[\left(1-\frac{E}{E_0}\right)\cdot\left(\ln\eta(E)-1\right)+\alpha(r)\cdot\left(\frac{E}{E_0}\right)^2\cdot\left(\ln\eta(E)-0.5\right)\right]\cdot e^{-\mu_W(E)t_W}\cdot e^{-\mu_{Fe}(E)t_{Fe}(r)} \quad \text{(Eq. 1)}$$

with E_0 the maximum electron energy in mega electron volt (MeV) falling onto the tungsten target. μ_W and μ_{Fe} are the energy dependent linear attenuation coefficients for tungsten and iron respectively. t_W and t_{Fe} are the respective thicknesses for the tungsten target and stainless steel flattening filter. t_{Fe} is a radial dependent function and $\eta(E)$ is an energy dependent parameter and is expressed as follows:

$$\eta(E) = \left[\sqrt{\left[\frac{0.511\cdot E}{2E_0(E_0-E)}\right]^2+\left[\frac{Z_W^{1/3}}{111.0}\right]^2}\right]^{-1} \quad \text{(Eq. 2)}$$

with Z_W the atomic number of tungsten with a value of 74 and 111.0 is Schiff's constant.

The radial dependence of parameter α is approximated by a linear function:

$$\alpha(r) = 0.3566 - 0.0087r \quad \text{(Eq. 3)}$$

$\alpha(r)$ accounts for off-axis beam softening. The thickness of the tungsten target (t_W) has a constant value of 0.04 cm. The radial dependent thickness profile of the 6 and 8 megavolt (MV) flattening filter is approximated by the following polynomial function:

$$t_{Fe} = 2.5528 - 0.010221r - 0.016438r^2 + 0.00078417r^3 - 0.000010411r^4 \quad \text{(Eq. 4)}$$

For the 15 MV beam it is:

$$t_{Fe} = 4.8183 - 0.1927r - 0.0114r^2 + 0.0007412r^3 - 0.0000101r^4 \quad \text{(Eq. 5)}$$

Using Eq. 4 and 5, the thickness profiles of the flattening filter for 6, 8 and 15 MV are shown in Fig. 2.2.

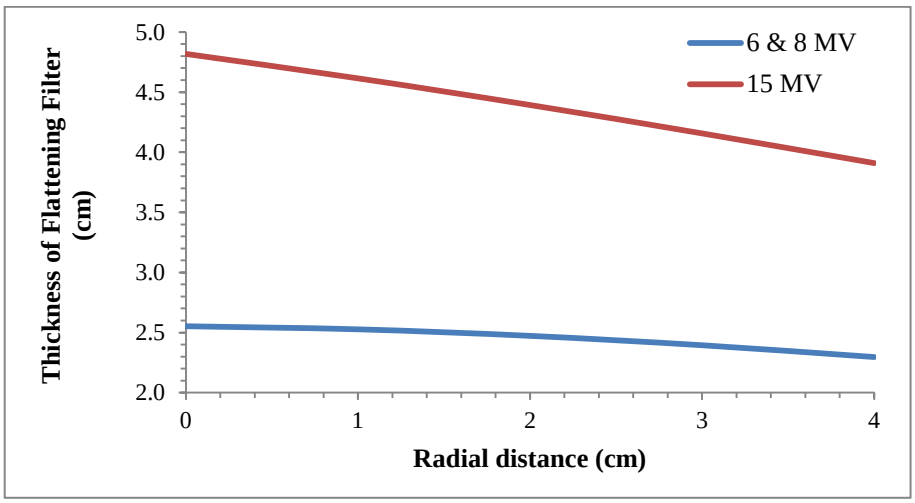

Fig. 2.2: Thickness profiles of flattening filter for 6, 8 and 15 MV beams.

The total linear attenuation coefficients for tungsten and iron (μ_W and μ_{Fe}) were obtained from the National Institute of Standards and Technology's database[43,44], and are shown in Fig. 2.3.

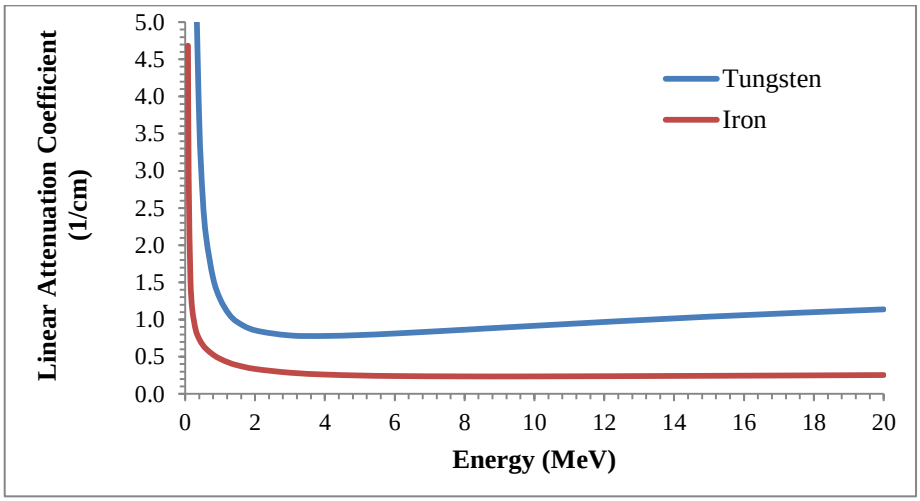

Figure 2.3: Linear attenuation coefficients for tungsten and iron at various energies.

Eq. 1 was used to calculate the photon energy spectra for 6 MV at various radial distances (r). These are shown in Fig. 2.4. From Fig. 2.4, the profile at radial distance of 4 cm has a higher number of photons of lower energy components than the profile at the CAX (r = 0 cm) due to beam hardening effect from the flattening filter near the CAX. Beam hardening is the process where the average energy of an X-ray beam is increased by means of filtering out the low-energy photons[45]. Thus, as the flattening filter's thickness decreases further away from the central axis, less low-energy photons are filtered out of the beam.

The spectral dependence on beam energy is calculated from Eq. 1. Photon energy spectrum profiles located on the central axis are shown in Fig. 2.5 for 6, 8 and 15 MV beams.

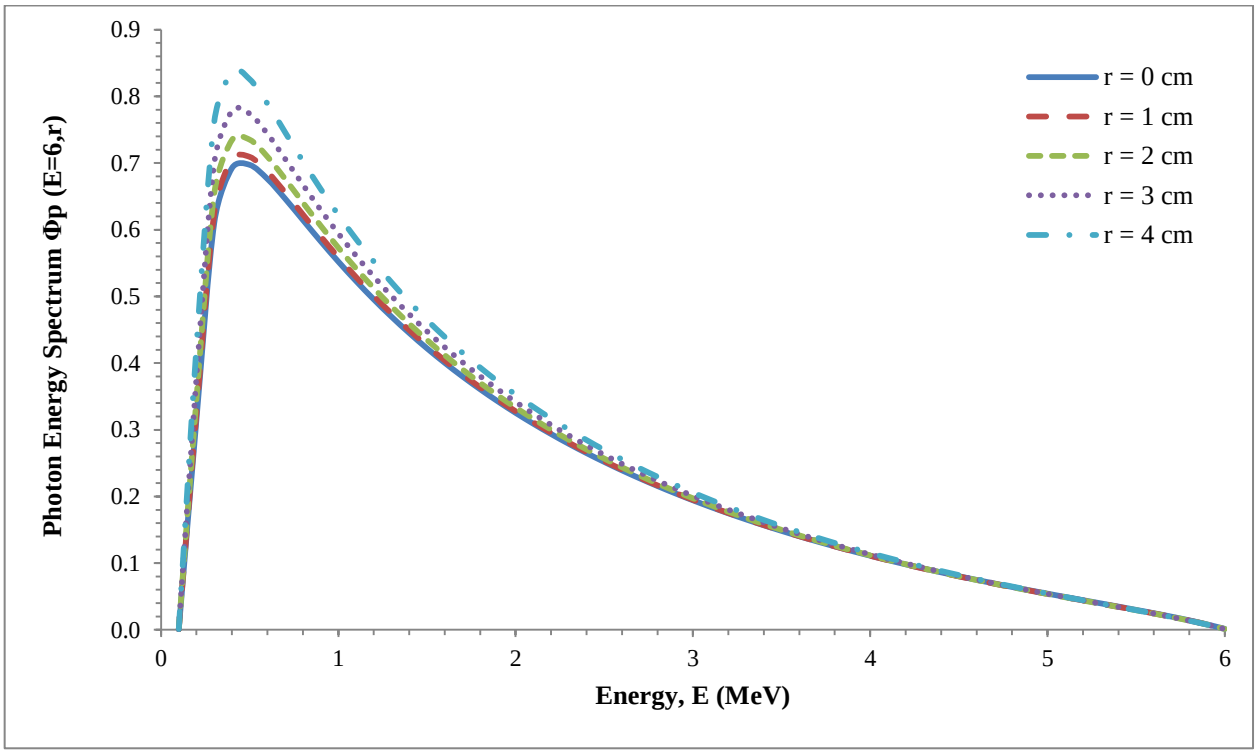

Fig. 2.4: Photon energy spectrum profiles for 6 MV beam at various radial distances (r). As *r* increases, so do the low energy components increases to model off-axis beam softening.

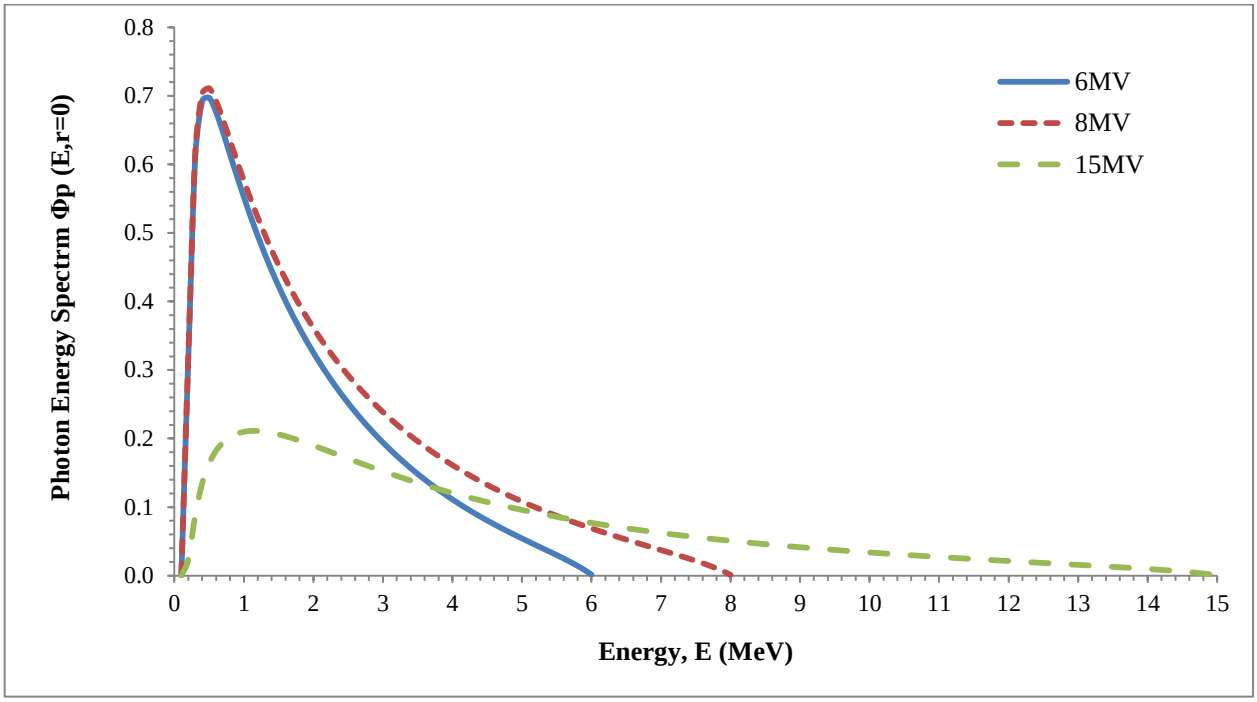

Fig. 2.5: Photon energy spectrum profiles for 6, 8 and 15 MV beams at the central axis (r = 0 cm), as calculated with Eq. 1.

2.2.2: Contamination electron energy spectrum

In theory the contamination electron energy spectrum can be deduced from the difference between a clinical depth dose and a pure photon beam. Fig. 2.6 illustrates this. The pure beam in Fig. 2.6 is represented by a MC simulated depth dose profile from a $20\times20cm^2$ aperture FS, while the clinical beam is the measured depth dose profile of the same aperture size for a 15 MV beam. From Fig. 2.6 it is clear that dose is required in the build-up region, thus contamination electrons for the source model are necessary. Electrons lose approximately 2 MeV/cm in water. Thus, the dose difference curve from Fig. 2.6 is displayed in Fig. 2.7 as an energy spectrum. The spectrum can be divided into energy bins, and from these an approximation (Eq. 6) for an energy spectrum is obtained.

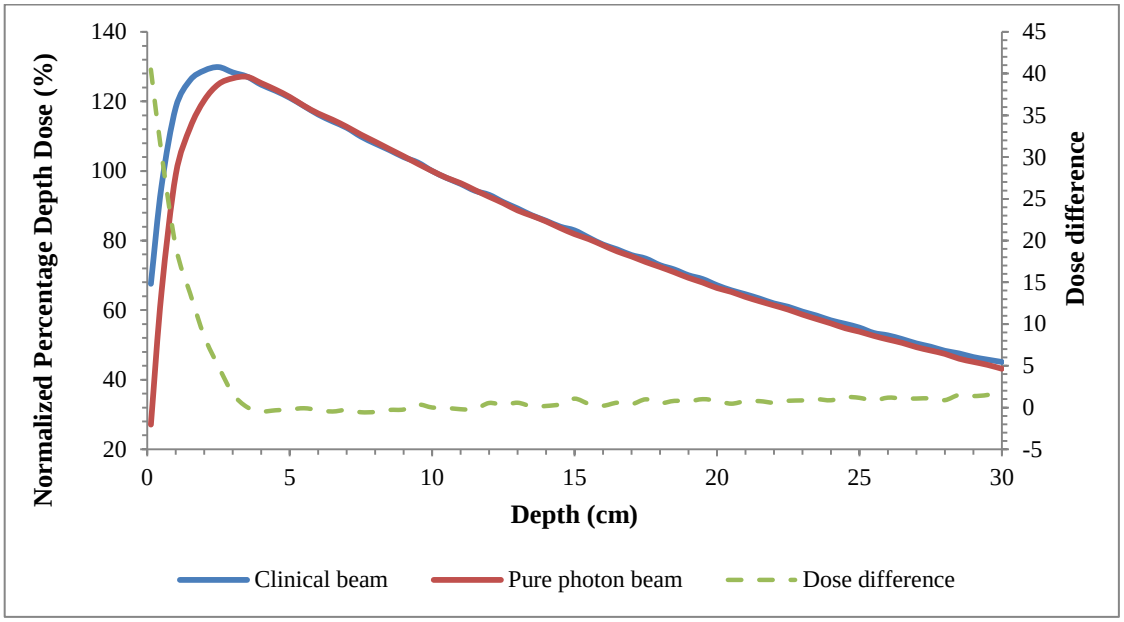

Fig. 2.6: Percentage depth dose (PDD) comparison between measured a clinical beam and a pure photon beam for a 15 MV 20×20 cm^2 square field aperture. The green dash curve is the difference in dose between the data sets.

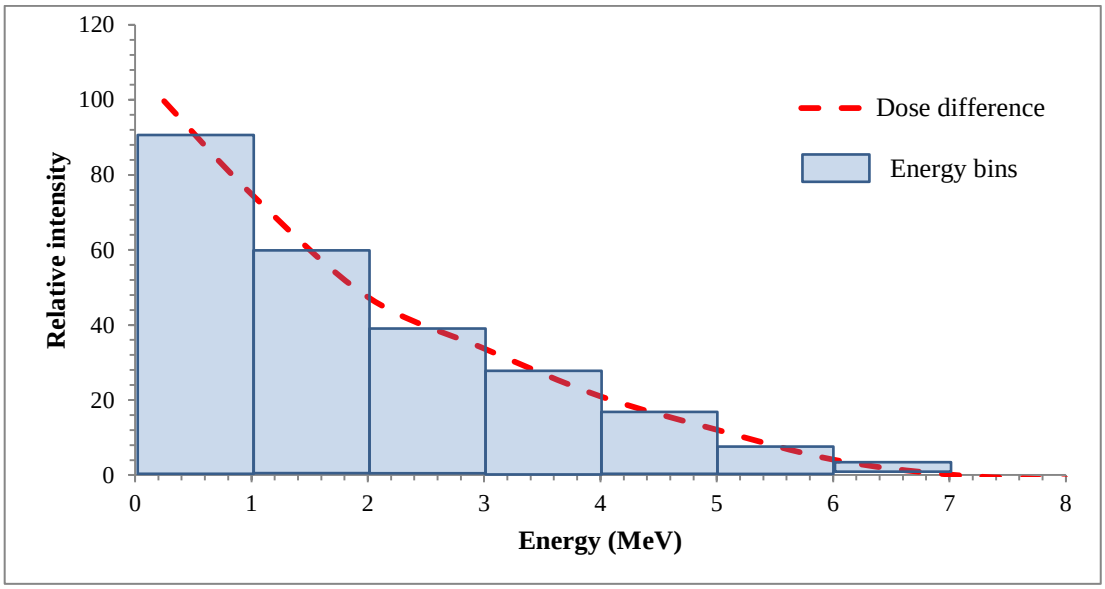

Fig. 2.7: Energy spectrum of the dose difference profile, with the energy bins for acquiring an approximation for the energy spectrum for the contamination electrons.

The following approximation for contamination electron energy spectrum for 15 MV obtained is used:

$$\Phi_e(E) = 235.5 - 156.7E + 46.84E^2 - 6.8977E^3 + 0.4866E^4 - 0.0131E^5 \qquad \text{(Eq. 6)}$$

with $1 \le E \le E_{max}$ and is shown in Fig. 2.8.

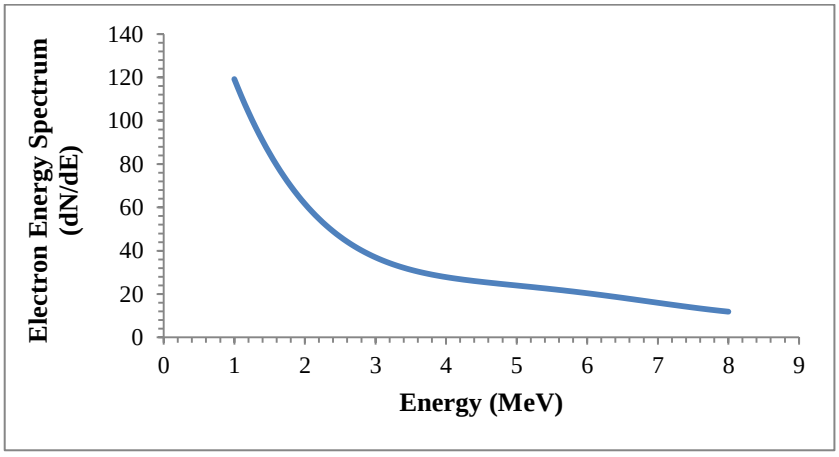

Fig. 2.8: Electron energy spectrum profile for 15 MV beam.

As a test a 15 MV 20×20 cm^2 source file, consisting entirely out of electrons, was simulated and its percentage depth dose (PDD) curve was compared to the dose difference curve (green curve in Fig. 2.6) and the comparison is displayed in Fig. 2.9 below. The comparison in Fig. 2.9 indicates that the electron spectrum approximation is suitable for additional dose in the build-up region of a depth dose curve.

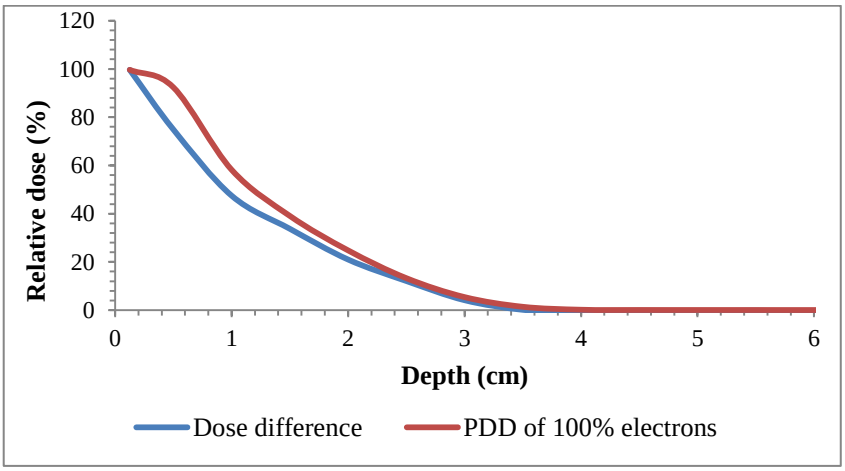

Fig. 2.9: Comparison of dose difference from build-up electron depth dose with the PDD of 15 MV 20×20 cm^2 square aperture consisting solely out of electrons.

2.2.3: Photon fluence

Photon fluence can be defined as the number of photons that fall onto a cross-sectional area of an imaginary sphere[46]. In this model, the Linac components that are exposed by the primary beam can alter the fluence at a certain plane downstream of the beam. Effects of the target, primary collimator, flattening filter, XY jaws, and the MLC's are taken into account for the shape and intensity of the final exit fluence field.

2.2.3.1: Target fluence

The fluence generated by the target (φ_{target}) is approximated by a Gaussian function as shown below:

$$\phi_{target} = p_j \cdot e^{-\frac{r^2}{\sigma_4^2}} \qquad \text{(Eq. 7)}$$

where parameters p_j is the amplitude of the function's peak, r is the radial distance and σ_4 is the full width at half maximum (FWHM) of the Gaussian. Fig. 2.10 illustrates target fluence profiles for various σ_4 values. As σ_4 increases, the FHWM of the Gaussian target fluence decreases. Thus the target fluence further from the CAX is lower.

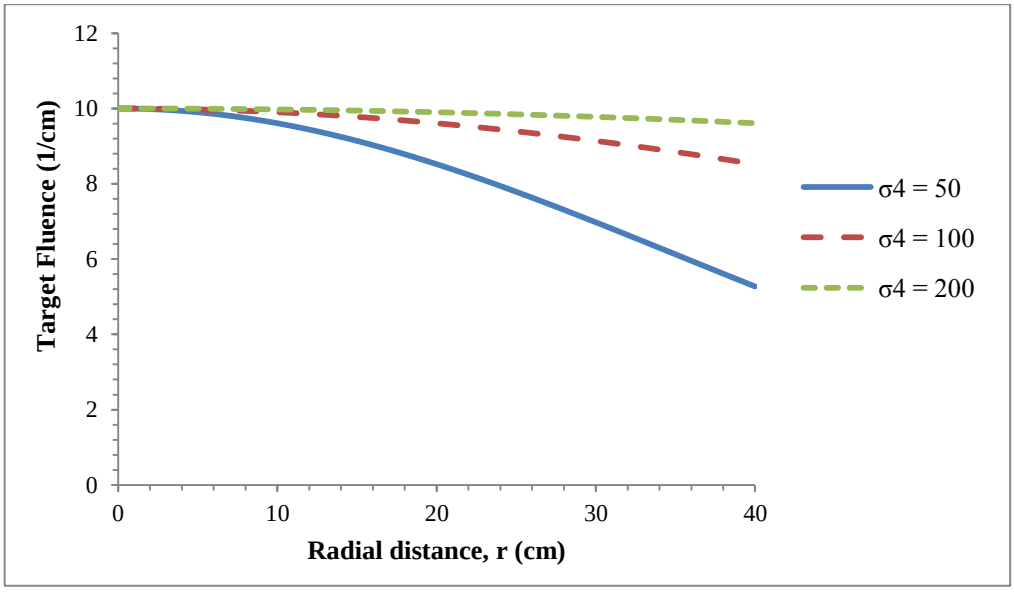

Fig. 2.10: Target fluence profiles for various σ_4 values.

2.2.3.2: Primary collimator effect on target fluence

The truncation effect of the primary collimator is modeled by an error function and the scatter behind it is added as an exponential decreasing function, and is shown as follows:

$$\phi_{pc} = \left[\phi_{target} \cdot erf(x_3, \sigma_1)\right] + \left[1 - erf(x_3, \sigma_1)\right] \cdot \left[p_h \cdot e^{-\mu_1 (r - x_3)} + const\right] \qquad \text{(Eq. 8)}$$

with p_h the amplitude of the decreasing function, μ_1 the 'decay' coefficient, x_3 is the radial position of the field's edge and *const* is an integer parameter.

The error function is calculated numerically via a method published by Khan et al[47] and is shown as follows:

$$erf(x_3, \sigma_1) = 0.5\left(1 - \sqrt{1 - e^{-1.245(x - x_3)^2 / \sigma_1^2}}\right) \qquad \text{(Eq. 9)}$$

with σ_1 the FWHM of the Gaussian function. Here x_3 is the field size width spanned by the primary collimator without any secondary field defining devices.

Changing the σ_1 parameter will have an influence in the penumbra width of the truncation effect of the collimator. To decrease the penumbra, σ_1 should be made smaller, illustrated in Fig. 2.11.

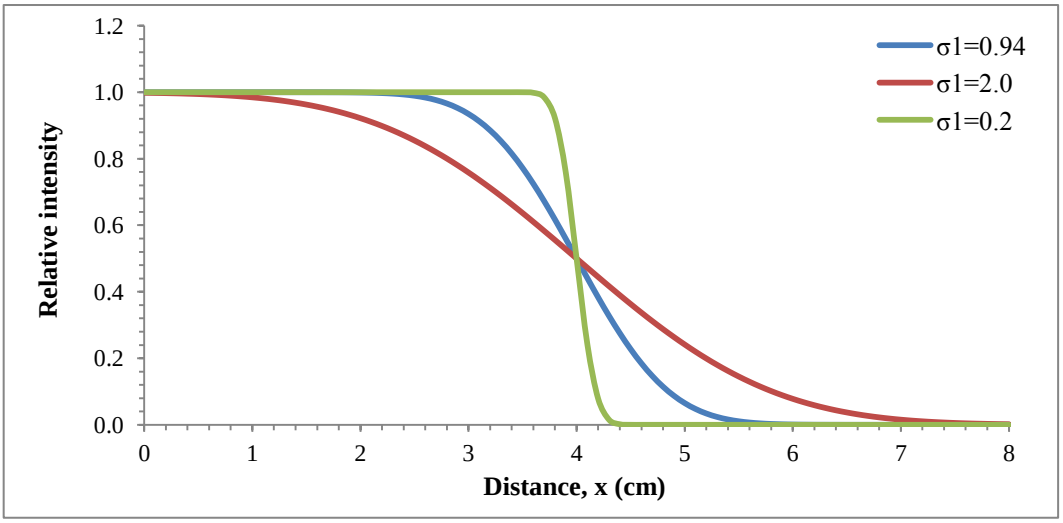

Fig. 2.11: Various values of the σ_1 parameter to change the penumbra effect of primary collimator. This is calculated with Eq. 9 for x_3 = 4 cm.

The inverse of the error function from Eq. 9 is written as follows:

$$1-erf\left(x_3,\sigma_1\right)=0.5\left(1+\sqrt{1-e^{-1.245(x-x_3)^2/\sigma_1^2}}\right) \qquad \text{(Eq. 10)}$$

The error function, along with its inverse (Eq. 10), is displayed in Fig. 2.12. As an example, the inverse error function was plotted with the exponential decreasing function in Eq. 8 using the parameters listed in Table 2.1 to create the primary collimator fluence profile (Φ_{pc}), displayed in Fig. 2.12.

Table 2.1: Parameters used for obtaining primary collimator fluence profile

Parameter	Value	Equation used in
p_j	10.00	7
σ_4	150.00	7
x_3	27.90	8, 9, 10
σ_1	0.94	8, 9, 10
p_h	4.00	8
μ_1	0.33	8

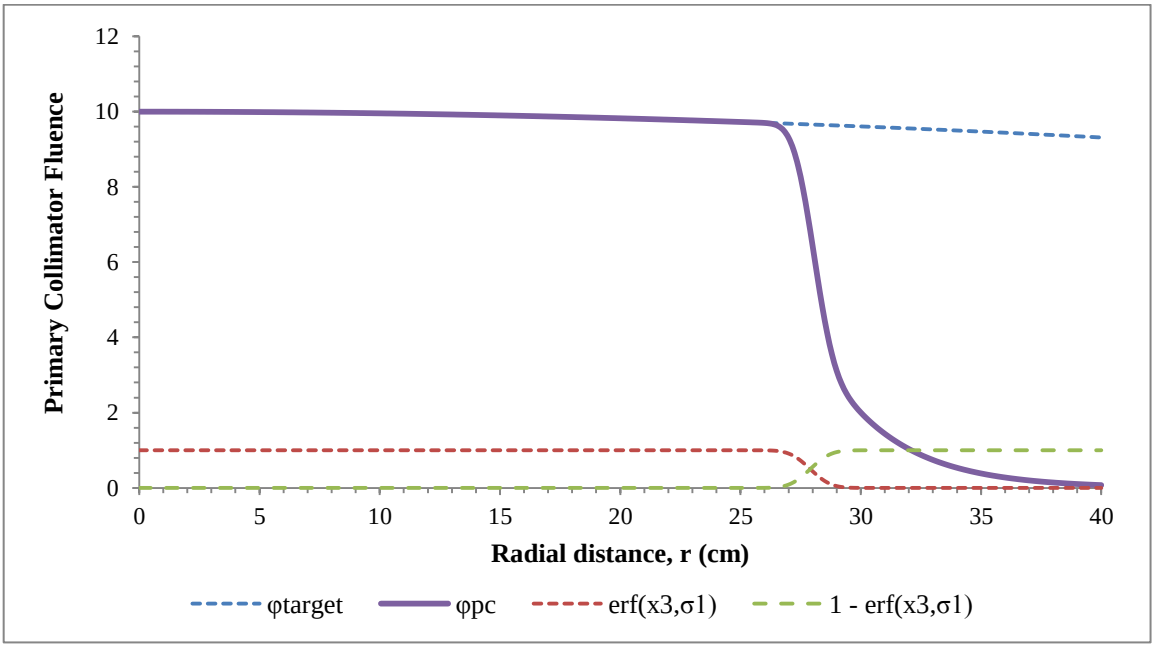

Fig. 2.12: Primary collimator fluence (Φ_{pc}) profile. The error function (red dash line) is responsible for the truncation effect of the target fluence profile (blue dash line) to create Φ_{pc} profile (purple solid line). Also shown is the inverse error function (green dash line)

2.2.3.3: Flattening filter fluence

The transmission by the flattening filter is approximated with an exponential:

$$ff = e^{-\mu_2 \cdot t_{Fe}} \qquad \text{(Eq. 11)}$$

with μ_2 the attenuation coefficient and t_{Fe} the thickness of the flattening filter, which is a function of radial distance (r) from the CAX.

For the 6 and 8 MV energy beams, the flattening filter thickness profile is approximated with the following polynomial function:

$$t_{Fe} = 2.2302 - 0.02r - 0.011r^2 + 0.00029r^3 \qquad \text{(Eq. 12)}$$

For the 15 MV energy beam, the profile has the following function:

$$t_{Fe} = 4.8183 - 0.05r - 0.0314r^2 + 0.0015412r^3 - 0.0000201r^4 \qquad \text{(Eq. 13)}$$

The flattening filter transmission profiles for 6, 8 and 15 MV energy beams are calculated with Eq. 11, 12 and 13 with μ_2 = 0.16 cm^{-1} and is shown in Fig. 2.13.

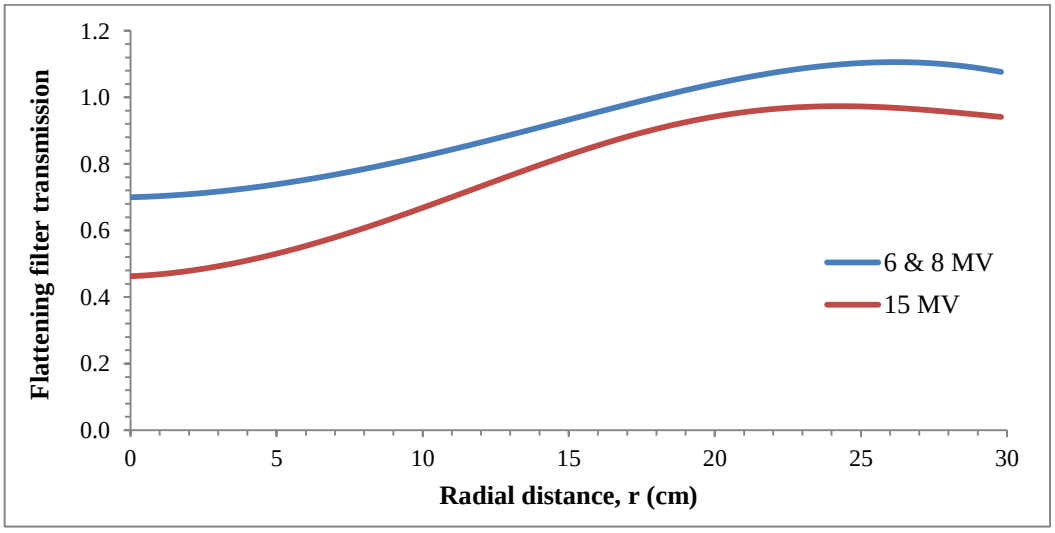

Fig. 2.13: Transmission profiles for the flattening filter for 6, 8 and 15 MV beams at a plane 52 cm below the target (source scoring plane).

The total fluence at the scoring plane can now be written as:

$$\phi_{pc+ff} = \phi_{pc} \cdot ff \qquad \text{(Eq. 14)}$$

This takes the primary collimator and transmission of the flattening filter into account.

The combined primary collimator and flattening filter fluence profiles for 6, 8 and 15 MV energy beams were calculated with Eq. 14 and are displayed in Fig. 2.14. 3D profiles of the combined primary collimator and flattening filter fluence profiles for 6, 8 and 15 MV energy beams were plotted using an IDL Graphical User Interface (GUI) and are displayed in Fig. 2.15.

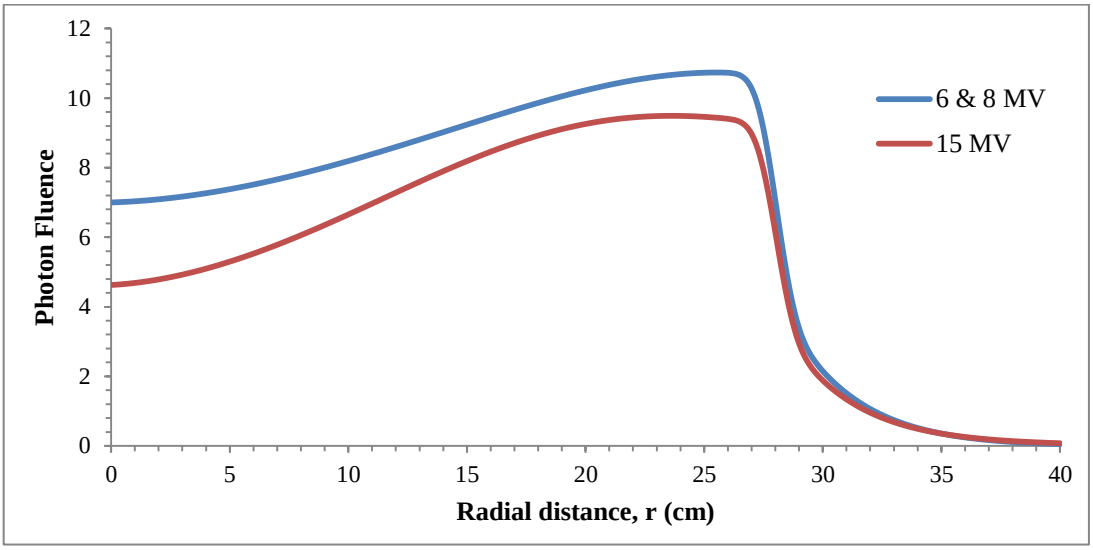

Fig. 2.14: Combination of primary collimator and flattening filter fluence profiles for 6, 8 and 15 MV beams.

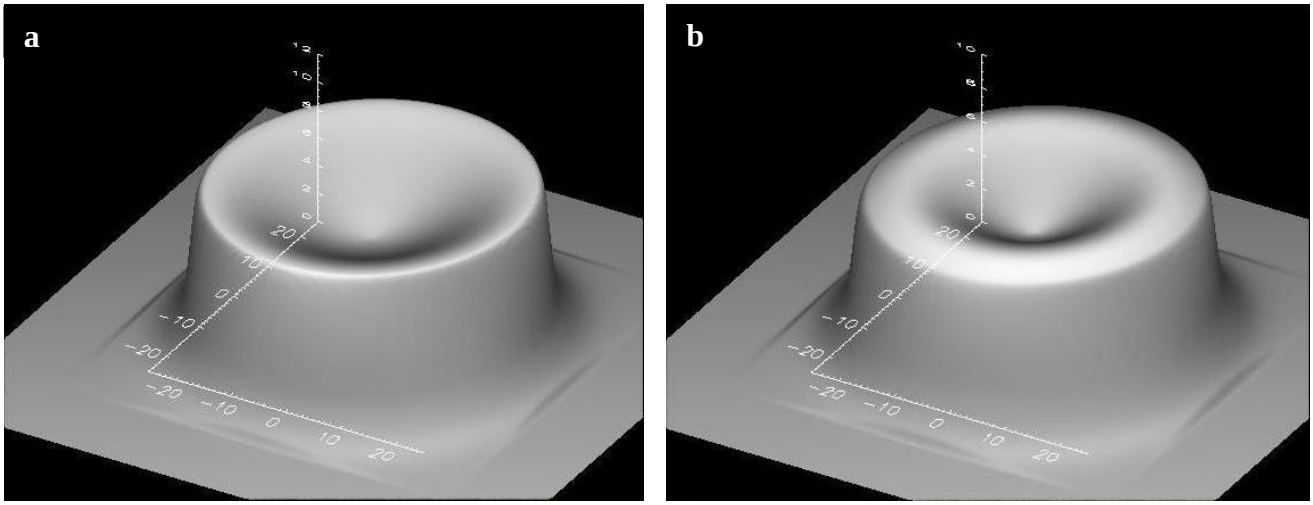

Fig. 2.15: 3D profiles of the combined primary collimator and flattening filter fluence for (a) 6, 8 and (b) 15 MV energy beams generated in the GUI.

2.2.3.4: X and Y collimator fluence

The modulation of the fluence by the independent X1 collimator (jaw) is modelled as follows:

$$\phi_{X1} = 1 - erf(x1, \sigma) \qquad \text{(Eq. 15)}$$

where $x1$ is the position of X1 jaw and σ is the FWHM of the Gaussian function leading to the error function describing the jaw fluence perturbation.

The modulation of the fluence behind the independent X1 jaw is modelled as follows:

$$\phi_{X1} = [1 - erf(x1, \sigma)] + transmission \times e^{-\mu_{out}|x-x1|} \qquad \text{(Eq. 16)}$$

where *transmission* is the maximum transmitted fluence and μ_{out} is the exponential decreasing function describing the fluence behind the X jaw and is expressed as follows:

$$\mu_{out} = 0.165 + 0.65e^{-0.05 \times X\_FS} \qquad \text{(Eq. 17)}$$

with *X_FS* the field size in the X-direction. The exponential decreasing function represents the transmission through the jaws as well as scatter into the outside of the open field.

Similar functions are used to represent ϕ_{X2}, ϕ_{Y1} and ϕ_{Y2} fluence profiles for X2, Y1 and Y2 jaws respectively.

The net effect of the exit fluence of the four independent jaws is then calculated as:

$$\phi_{XY} = \phi_{X1} \cdot \phi_{X2} \cdot \phi_{Y1} \cdot \phi_{Y2} \qquad \text{(Eq. 18)}$$

and the total fluence under the jaws as:

$$\phi_{pc+ff+jaws} = \phi_{pc} \cdot ff \cdot \phi_{XY} \qquad \text{(Eq. 19)}$$

Using the parameters from Table 2.2 and substituting them into Eq. 15 to 17, the photon fluence profiles of X1 jaw for 6, 8 and 15 MV energy beams are calculated and are displayed in Fig. 2.16. Fig. 2.17 is a 3D representation of the X1 jaw fluence profile generated in IDL for the 6 MV energy beam.

Table 2.2: Parameters used for obtaining independent collimator (jaw) fluence profiles for the X1 jaw

Parameter	Value	Equation used in
σ	0.15	15, 16
x_1	10.00	15, 16
transmission	0.04	16
μ_{out}	0.40	16

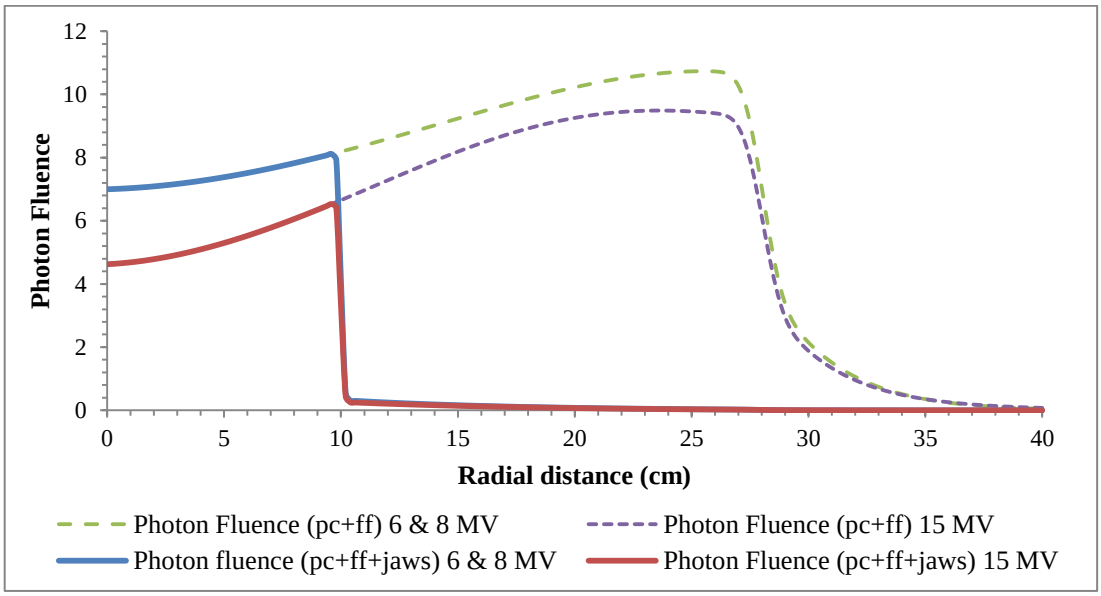

Fig. 2.16: Combination of primary collimator, flattening filter and jaws fluence profiles for 6, 8 and 15 MV beams.

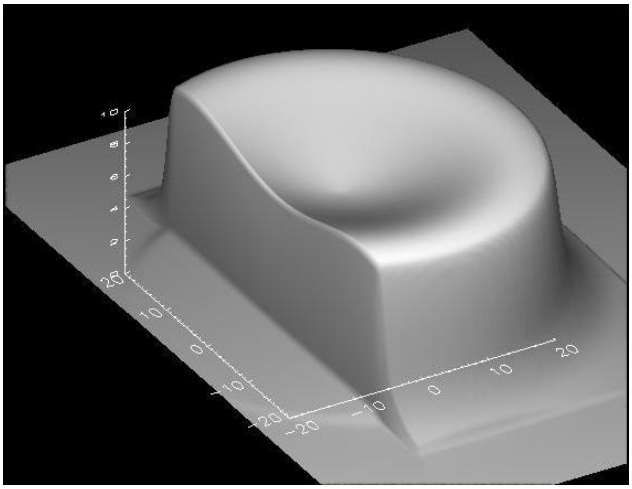

Fig. 2.17: 3D profiles of the combined primary collimator, flattening filter and X1 jaw fluence at the exit plane located 52 cm below the target for 6 MV energy beam generated in the IDL developed GUI.

Fig. 2.18 (a) shows a 3D representation of the combined primary collimator, flattening filter and X1 and Y1 jaws photon fluence profile, with X1 and Y1 both at -10.0 cm positions for 6 MV energy beam. In Fig. 2.18 (b) X2 and Y2 jaws are included at +10.0 cm positions, thus displaying the combined XY jaws, along with the primary collimator and flattening filter, photon fluence.

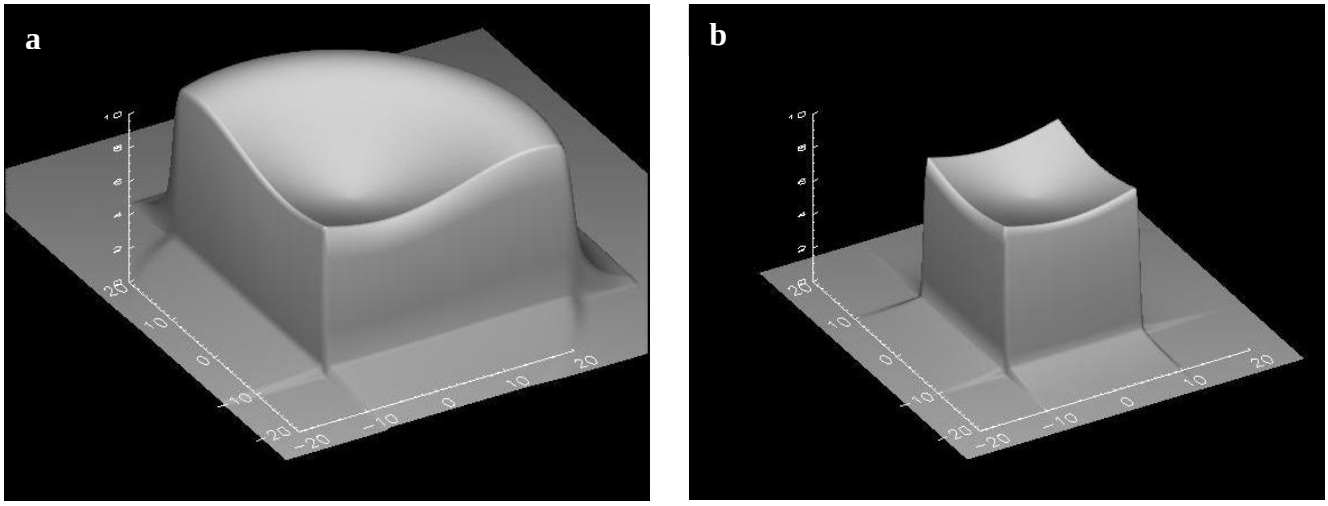

Fig. 2.18: 3D profiles of the combined primary collimator, flattening filter and (a) X1 and Y1 (b) XY fluence profiles generated in the GUI.

2.2.3.5: Multileaf collimator (MLC) fluence

The modulation of the fluence by a single MLC leaf is treated in a similar way as that for a single jaw. For example, the fluence profile due to one edge of the leaf in the X-direction is modelled by:

$$\phi_{mlcx1} = 1 - erf(mlcx1, \sigma_{xmlc}) \quad \text{(Eq. 20)}$$

with the leaf tip at $x1$ and σ_{xmlc} the FWHM of the Gaussian derivative of the error function. The fluence under the leaf in the X-direction is modelled by:

$$\phi_{mlcx1} = [1 - erf(mlcx1, \sigma_{xmlc})] + trans\_mlc \times e^{-\mu_{out\_xmlc}|x - mlcx1|} \quad \text{(Eq. 21)}$$

for $x < mlcx1$. The *trans_mlc* parameter represents the transmission through the leaf; μ_{out_xmlc} is expressed as follows:

$$\mu_{out\_xmlc} = 0.165 + 0.65e^{-0.05 \cdot xleft} \quad \text{(Eq. 22)}$$

with *xleft* the *x*-position the MLC leaf on the left bank. The exponential function represents the transmission as scatter from outside the open field into the leaf shadow.

Similar functions are used to model fluence scatter from the edge in the Y-direction and is written as:

$$\phi_{mlcy} = 1 - erf(mlcy, \sigma_{ymlc}) \quad \text{(Eq. 23)}$$

and,

$$\phi_{mlcy} = [1 - erf(mlcy, \sigma_{ymlc})] + trans\_mlc \times e^{-\mu_{out\_ymlc}|y - mlcy|} \quad \text{(Eq. 24)}$$

The net effect of a single leaf on fluence perturbation is given by:

$$\phi_{mlcxy} = 1 - \left(\phi_{mlcx1} \cdot \phi_{mlcx2} \cdot \phi_{mlcy}\right) \cdot (1 - trans\_mlc) \quad \text{(Eq. 25)}$$

As an example, parameters in Table 2.3 were substituted into Eqs. 20 - 25. The photon fluence profiles of MLC leafs for 6 MV energy beam was calculated and are displayed in a 3D presentation in Fig. 2.19. The MLC aperture size is 20×22 cm^2 with the XY jaws set on 20×20 cm^2.

Table 2.3: Parameters used for illustrating MLC effects on exit fluence profiles

Parameter	Value	Equation used in
σ_{xmlc}	0.40	20, 21
σ_{ymlc}	0.40	23, 24
trans_mlc	0.02	21, 24, 25
μ_{out_xmlc}	0.40	21
μ_{out_ymlc}	0.38	24

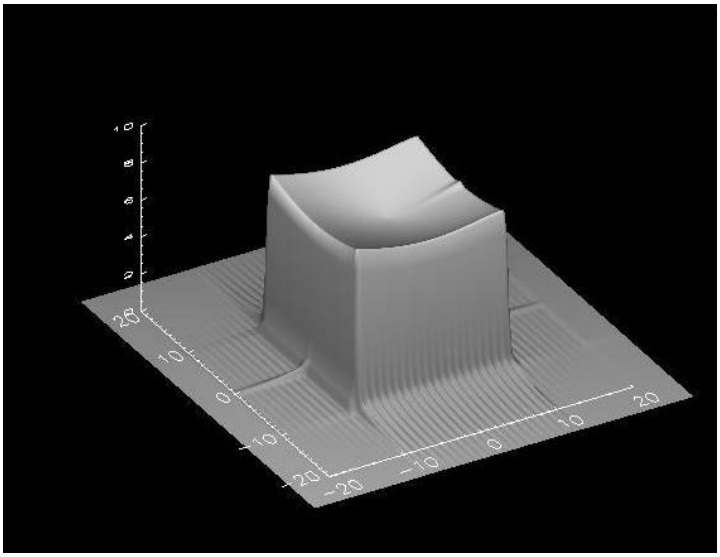

Fig. 2.19: 3D profiles of the combined primary collimator, flattening filter, XY jaws and MLC fluence for 6 MV energy beam generated in the GUI.

2.3: Monte Carlo (MC) Simulations

The MC method presents a numerical solution to a problem. It models objects interacting with each other or their environment based on simple object-object or object-environment relationship. In order to determine a solution, random sampling of interactions should occur until the result converges. The mechanics of executing a solution involves repetitive actions or calculations[48]. Due to the stochastic nature of particle transport, it is an ideal model to simulate with MC.

2.3.1: Particle transport

The incident particle's history is determined from: (i) medium geometry and composition; (ii) the particles' initial state, e.g. incident position, direction, charge and energy; and (iii) random selection of possible interactions of photons and electrons[49]. At any instance during a photons history, one or more particles (photons and electrons), their position, direction and energy is stored in memory on a stack. A particle's transport to its next position is called a *step*, after which the variables on the stack associated with that particle are updated. The key factors during a photon step are: (1) distance to the next interaction site; (2) type of interaction; (3) new particles, energies and directions; and (4) next transport step.

2.3.1.1: Photon transport

The photon transport step can be described using Fig. 2.20 as follows:

(1) Distance to the next interaction site

The particle is transported, in its current direction, for a randomly selected distance. The selection of a particular distance is performed by direct sampling from a probability density function (PDF) which is based on the mean free path of the medium for the photon energy under consideration (see Section 2.3.2.1).

(2) Type of interaction

After the photon was translated over this distance, a decision is made on the type of interaction to take place at that position. An interaction type is chosen randomly based on branching ratios, which depends on the photon energy and medium composition (see Section 2.3.2.2).

(3) New particles, energies and directions

When the interaction type is selected, the resulting scatter energy and angle of the original particle is chosen. These parameters are determined from cross section tables and from the kinematics of the interaction, again considering the current energy of the photon and the medium.

(4) Next transport step

The new particles created and/or set in motion after the interaction event, are transported to the next interaction site. The process continues until the particle escapes from the medium geometry or has lost all its energy. We say that one history has been completed.

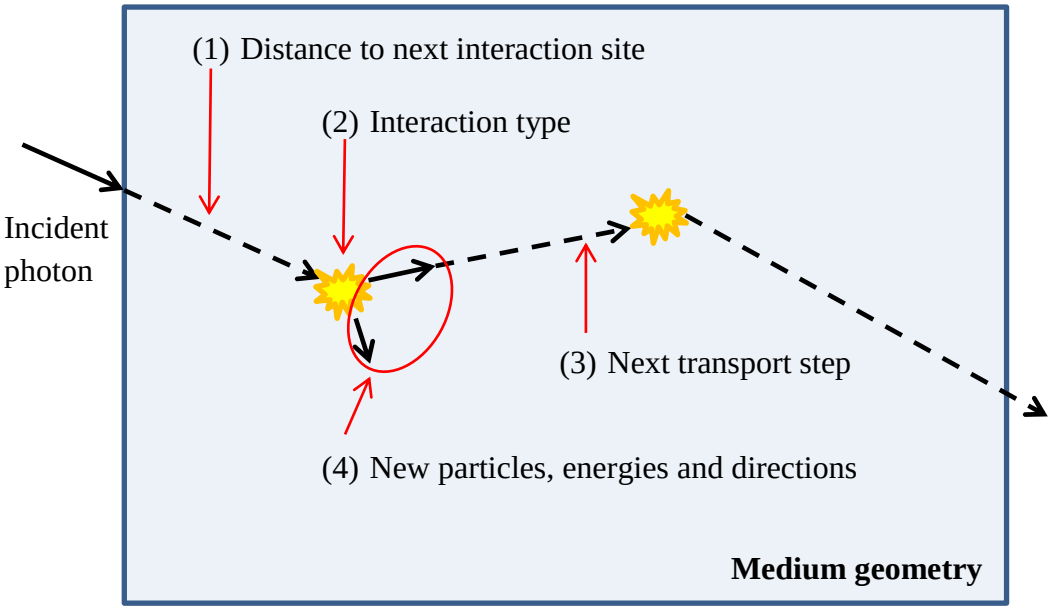

Fig. 2.20: Illustration of the key factors during a photon transport step. The process continues until the particle escapes the medium or has lost all its energy.

2.3.1.2: Electron transport

While the spatial distribution of energy imparted from photon interactions are primarily responsible for the dose distribution, electron transport takes up most of MC simulation computing time. In EGSnrc, electrons are transported until they fall below a set user-defined cutoff energy called *ECUT*. In the case for photons, this is called *PCUT*. Electron steps do not follow the particle transport from one discrete interaction to the next as in the case with photon transport. The electron's multiple Coulomb scattering interactions and energy losses are condensed. After each step the electron has lost a small amount of energy, through radiative and collision losses. It is also scattered by a small angle into a new direction, as illustrated in Fig. 2.21. This is referred to as a condensed history (CH) technique[19,25,27,28,49,]. The energy lost in the step is the product of the step length and stopping power of the medium, which is electron energy dependent. The deflection angle after the step is obtained by sampling step length and angular distribution data. The angular distribution is characterized by the scattering power, which is energy and medium dependent.

Energy losses are organized such that the energy is stored evenly, or continuously, along each step. This is called a *continuously slowing down approximation* (CSDA). Thus, all electrons with the same energy will travel the same distance before depositing their energy. In EGSnrc, energy losses below a set user-defined threshold will be modelled using CSDA, whereas those above the threshold will be treated individually in the same way as for photon interactions. The threshold for discrete radiative and collision energy losses are respectively called AP and AE. The lower these threshold values are set, the more random the electron transport process will occur. During electron transport, boundary-crossing and electron-step algorithms are involved[50]. These are explained in the next section.

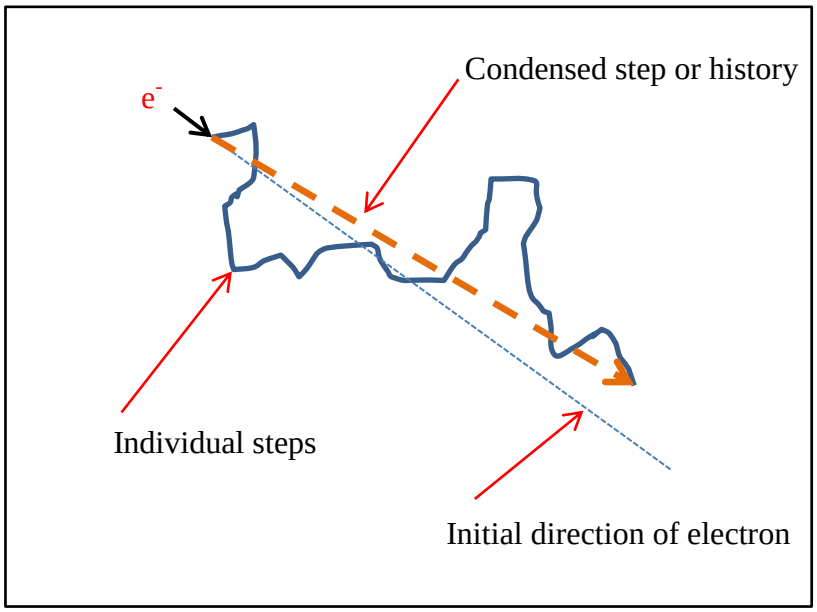

Fig. 2.21: Illustration of electron transport with an electron's individual steps, along with its condensed step. The energy loss in the condensed step is based on the CSDA, with the angular deflections based on multiple Coulomb scattering interactions.

In EGSnrc, when a particle's energy falls below ECUT and/or PCUT, its history is terminated and the residual energy is deposited at that site. For low ECUT and PCUT values the simulation is slowed down as the particles are transported through more steps before they are discarded. Larger values for

ECUT and PCUT can thus be used for high energy beams as well for larger scoring regions. Care should be taken that it should be not too high for the geometry size to avoid biased data.

2.3.2: Random sampling

Selecting parameters such as electron scattering, photon step or path length, etc., is a random process. The chance that a particular value for each parameter is chosen depends on the probability distribution controlling the event's outcome[49]. Random numbers used are determined by the type of distribution sampled. Two random selection schemes for photons are described below; first the distance to the next interaction site and second for selecting the type of interaction[51]. For charged particles (electrons), the random selection schemes that will be demonstrated are boundary crossing and electron-step events.

2.3.2.1: Path length selection

Path length selection makes use of direct sampling where the variable, thus the distance to the next interaction site, is obtained by using a PDF. It gives the probability that a variable will have a certain value. The PDF is given by:

$$p(x) = \mu e^{-\mu x} \qquad \text{(Eq. 26)}$$

with μ the linear attenuation coefficient and x the distance or depth in the medium. μ is the inverse of the mean free path (λ) of the photon, and determines the distance the photon travels before its next interaction. λ depends on the medium with which the photon is interacting as well as its energy. Using a value of 0.1 cm^{-1} for μ in Eq. 26, a plot for the PDF, *p(x)*, is displayed in Fig. 2.22. The PDF is integrated to give a cumulative density function (CDF) that has a maximum value of 1.0 after normalization. The CDF is expressed below:

$$c(x) = 1 - e^{-\mu x} \qquad \text{(Eq. 27)}$$

and is displayed in Fig. 2.22.

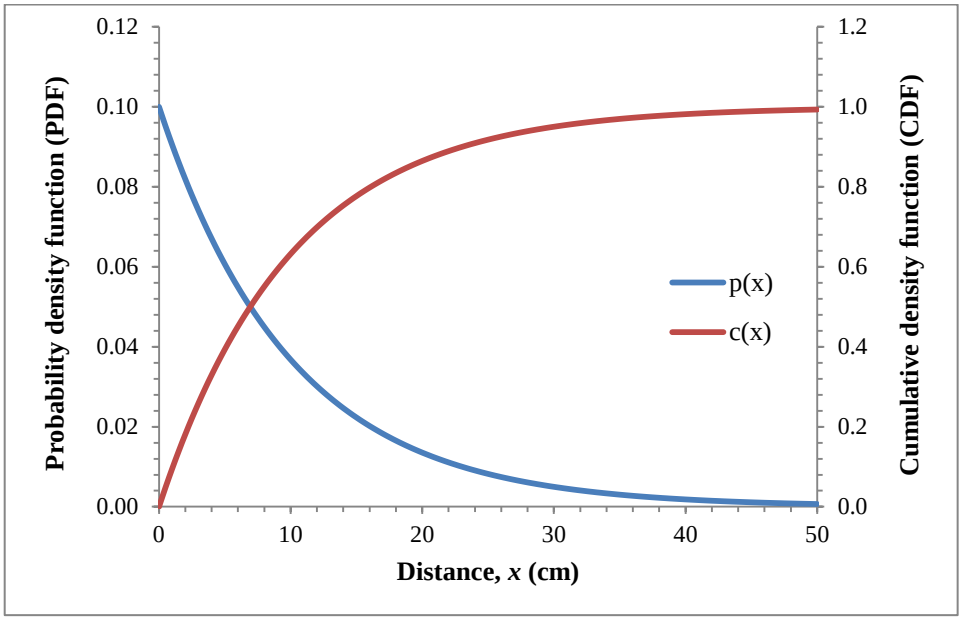

Fig. 2.22: Cumulative density function (CDF) makes use of an inversion sampling in order to obtain the distance to the next photon interaction. CDF is the integral of the probability density function (PDF)

From Fig. 2.22, the value of *c(x)* ranges between 0 and 1 as *x* goes from 0 to infinity. Thus, a value of *x* is chosen by randomly selecting a value of c(*x*) and projecting it onto the *x* axis. *c(x)* in Eq. 27 is invertible, meaning that this injective function will yield unique values for *x* for every *c(x)* chosen. Thus *x* can be directly calculated from:

$$c(x) = 1 - e^{-\mu x}$$

$$1 - c(x) = e^{-\mu x}$$

$$\ln[1 - c(x)] = -\mu x$$

$$x = \frac{\ln[1 - c(x)]}{-\mu}$$

$$x = \frac{\ln[c(x) - 1]}{\mu}$$

since $c(x) \leq 1 \ \forall \ \ x \in \Re$. There exists symmetry between $\ln[c(x) - 1]$ and $\ln[c(x)]$ since *c(x)* is randomly sampled we can say that:

$$x = \frac{\ln[c(x)]}{\mu} \qquad \text{(Eq. 28)}$$

The probability of choosing between x and $x + dx$ is proportional to the slope of c(x). With path length selection, this means that the probability of a path length x being chosen decreases exponentially with x. Once an interaction site is selected, an interaction type is chosen based on the probability of each process to occur.

2.3.2.2: Interaction type for photons

Relative probabilities or branching ratios are used for selecting an interaction type or process. The important interaction processes in MC for megavolt photons are: Compton scattering, photo-electric effect and pair production[52]. The branching ratio for interaction type i is the ratio of the cross section (σ_i) over the total cross section (σ_t). The interaction type is selected by sampling a random variable between 0 and 1, and finding the interval to which it corresponds. Fig. 2.23 illustrates an example for sampling an interaction type.

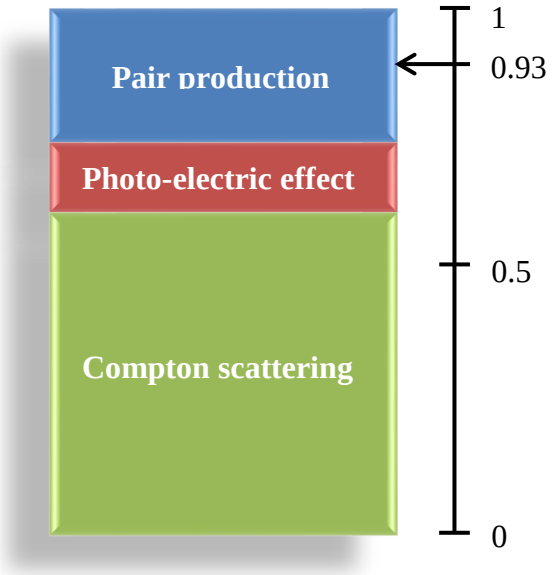

Fig. 2.23: Example of branching ratios for sampling interaction types for photons. The interaction is randomly selected based on the variable ranging between 0 and 1. The arrow indicates that a pair production event is to take place for random number R = 0.93.

2.3.2.3: Boundary crossing and electron-step algorithms for charged particles

Ideally, charged particle transport using the CH technique with multiple Coulomb scattering works in a homogeneous medium[27,49]. Fig. 2.24 shows an example where more than one material of medium is present. The two regions consist of different materials, with two electron tracks; a real electron track and a CH simulated electron path. As described before, the CH technique simulates the condensed effect of a number of real electron paths through multiple Coulomb scattering interactions. Some of the electron paths are simulated in material B, with the rest in material A.

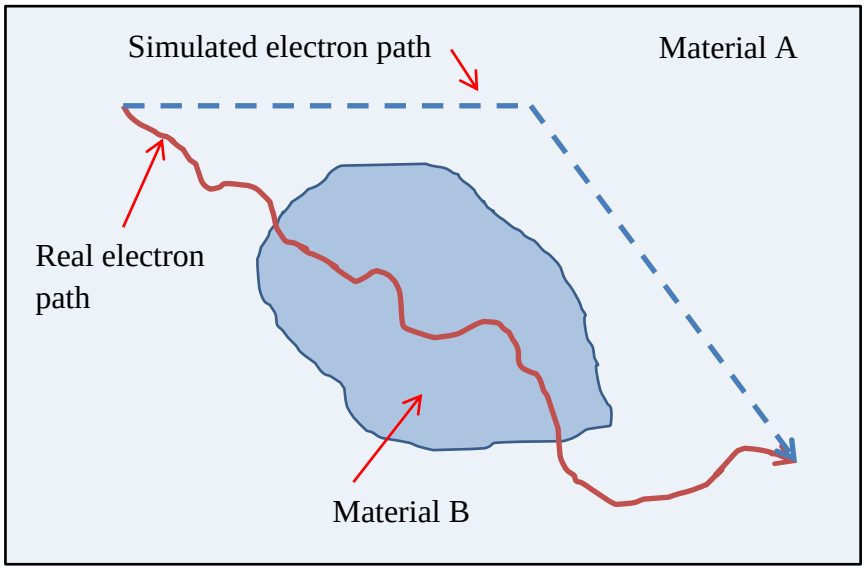

Fig. 2.24: Example of an electron path through various media using the random hinge method. Simulation artifacts can occur due to CH technique electron path not being influenced by material B, but the real electron path is influenced by material B.

The CH technique only exists where the distance to the material boundary is larger than the electron-step size. This means that the maximum step size must be smaller when an electron is in close vicinity to a material interface, and larger when the electron moves away from the boundary. PRESTA was the first to use this kind of step size variation[53]. Smaller step sizes will thus be present where a large number of small inhomogeneous regions are present. This will result in longer calculation times. As

the electron is about to cross a boundary, its CH step size will become infinitesimally small. This must be deactivated if the boundary crossing is to be allowed. In this case the step size becomes similar to the boundary distance, which can cause step size artifacts. In order to avoid these artifacts, a more accurate algorithm exists in EGSnrc.

In EGSnrc, the minimum distance (d_{min}) to the next material interface is selected by the user and CH transport will only occur when the electron is far away from the boundary than d_{min}[49]. If the electron is closer to the boundary than d_{min}, the electron will be transported in a single scattering mode. For MC simulations used in RT, boundary crossing artifacts can be ignored due to their negligible influence on the result. For example, the random hinge technique can be used to simulate electron boundary crossing without stopping at the interface. Material A's multiple scattering properties are used if the "hinge" is sampled in region of material A (Fig. 2.24); otherwise, the material B's properties are used. The total electron step length is dependent both materials' stopping powers and corresponding step segments. PENELOPE's user guide states that this approach provides a "fairly accurate description of interface crossing"[23]. Thus, it is an accurate and efficient method for MC-based dose calculations in RT treatment planning systems and Linac head modeling.

2.3.3: Random number generation

MC systems use random numbers to select initial starting events and dynamic variables for each particle history. Random number generators (RNGs) are classified into three types: true-, pseudo- and quasi-random numbers. True random numbers must be generated by a random physical process, such as radioactive decay. Pseudo-random numbers are generated by a single numerical algorithm, thus not truly random. To someone not familiar with the algorithm the sequence of the numbers appear random. Quasi-random numbers are also generated using a numerical algorithm, but the numbers are uniformly distributed and do not appear to be random[54].

Generating pseudo-random numbers during simulations takes a large amount of computing time, thus the efficiency of the code responsible for generating these numbers is important. The sequence of the random numbers is very long and it is also important that the numbers do not repeat themselves during the simulation. In the event this does occur, numerous particles histories will be identical to previous histories in the simulation. Seed numbers are initially used to start the sequence.

EGSnrc makes use of two pseudo-random number generators: RANLUX and RANMAR. RANLUX is used as the default generator. RANMAR has a quality situated between luxury levels 1 and 2 of RANFLUX and produces incorrect answers with luxury level 0 in some practical EGSnrc calculations[49,55,56,57]. For producing 3D dose distributions with very low uncertainties, a longer sequence is necessary. The lagged Fibonacci RNG has a sequence length or period of 2^{144} and is suitable for all practical purposes[58].

2.3.4: Statistical variance

It is important that the uncertainty or error in a MC result is known. The uncertainty is calculated by dividing a simulation into a number of batches. Each batch is a separate simulation of equal number of particle histories. When al batches are finished, the average or mean energy stored in each voxel is calculated along with the standard error in the mean (uncertainty). The uncertainty (σ) is expressed as follows:

$$\sigma \propto \frac{1}{\sqrt{N}} \qquad \text{(Eq. 29)}$$

with N the number of histories simulated per voxel. This means for an uncertainty of 0.01 (1%) the number of histories in each voxel should be approximately 10 000. Usually ten batches are used in EGSnrc for calculating the uncertainty.

2.3.5: Efficiency and variance reduction

The efficiency (ε) of a MC calculation can be estimated by:

$$\varepsilon = \frac{1}{\sigma^2 T} \qquad \text{(Eq. 30)}$$

where T is the computation time to obtain a variance estimate σ^2. Since the uncertainty is inversely proportional to the square root of the number of particle histories (Eq. 29), it is also inversely proportional to the square root of the computation time, T. Thus ε is invariant with T for a particular simulation type. In order to increase the efficiency, variance reduction techniques are used. These techniques reduce either (i) the uncertainty or variance for a particular simulation time or (ii) the time needed to obtain results with a determined uncertainty. Examples of techniques for variance reduction used in dose distributions are: geometry interrogation, zonal discard and range rejection[59].

2.3.5.1: Geometry interrogation

As a particle is being transported, geometry-checking is performed before each step to verify whether the particle will cross a voxel boundary during the step. In EGSnrc this is called HOWFAR. The process is useless if the particle is far from any boundary. In order to save time, the current closest distance (variable DNEAR in EGSnrc) from the boundary is stored so that geometry checking is only achieved when the particle is close to a boundary, as illustrated in Fig. 2.25.

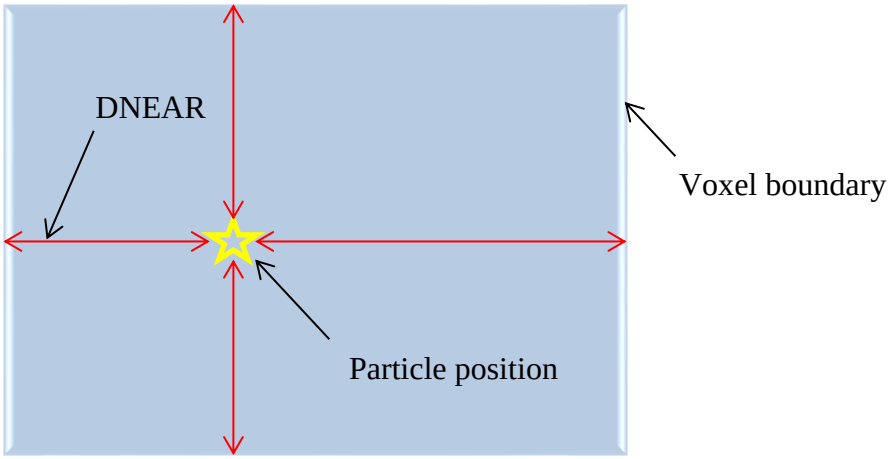

Fig. 2.25: Example of geometry-checking (HOWFAR) for variance reduction technique

2.3.5.2: Zonal discard

If an electron's energy is insufficient for it to escape a voxel, its kinetic energy is deposited in the voxel instead of transporting the electron any further, as illustrated in Fig. 2.26. R(E) is the radius or range of the electron for its current energy state.

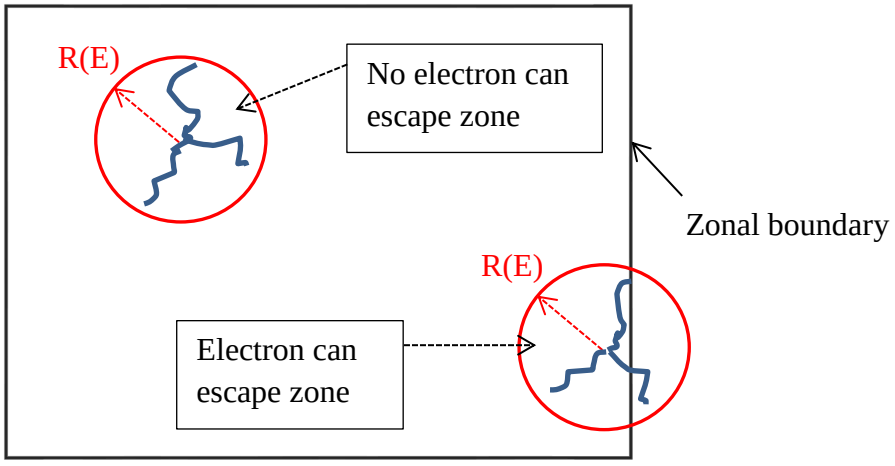

Fig. 2.26: Example of discard within a zone for variance reduction technique

2.3.5.3: Range rejection

This technique means that an electron's transport is terminated once its residual range, R(E), is smaller than the distance to the nearest boundary or region of interest (ROI)[60]. A large amount of CPU time can be saved using this technique in energy deposition problems where large regions exist. As illustrated in Fig. 2.27, the electron tracks are discarded where their range does not reach the scoring zone or ROI. Only the electron tracks reaching the ROI continue to be sampled.

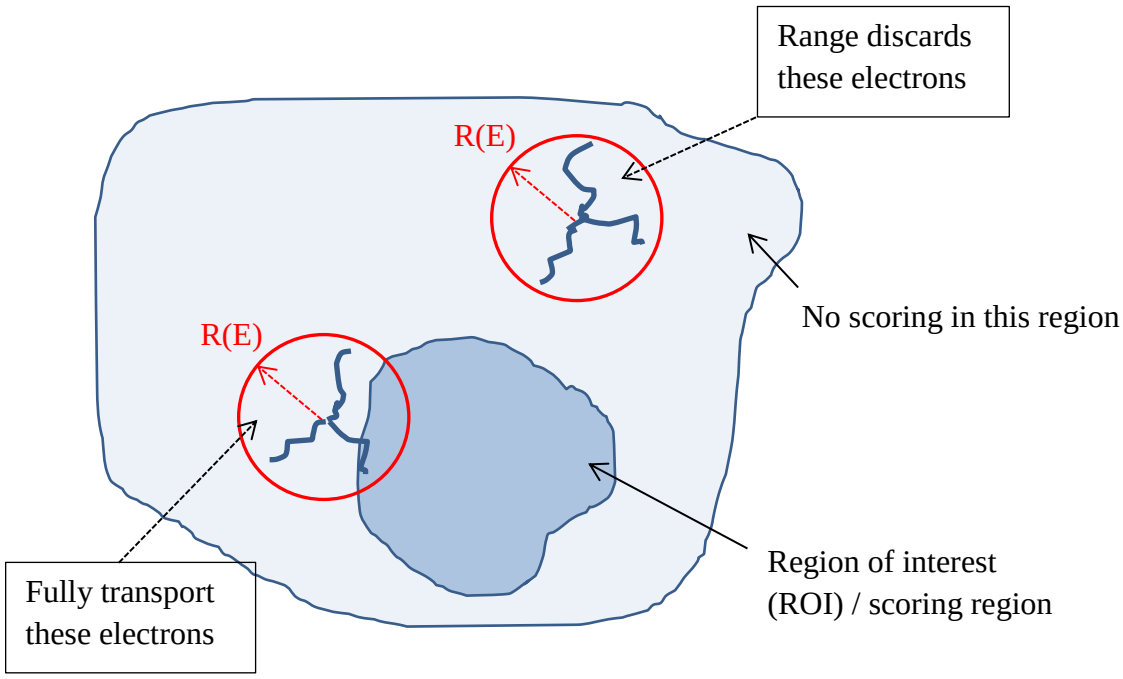

Fig. 2.27: Example of range rejection for variance reduction technique

2.4: GAFCHROMIC® EBT2 film

The source model is MC based but two dimensional (2D) dose distributions will also be measured with film to validate the source model. EBT2 film is composed out of a base of polyester substrate with a thickness of 175 micron (μm), followed by an active layer of 30 μm thickness. On top of this layer is a topcoat of 5 μm thickness, followed by an adhesive layer of 25 μm thickness. A polyester over-laminate, with a thickness of 50 μm, completes the film. The total thickness of the film is 285 μm or 0.285 mm. The configuration of the EBT2 film is shown in Fig. 2.28[36].

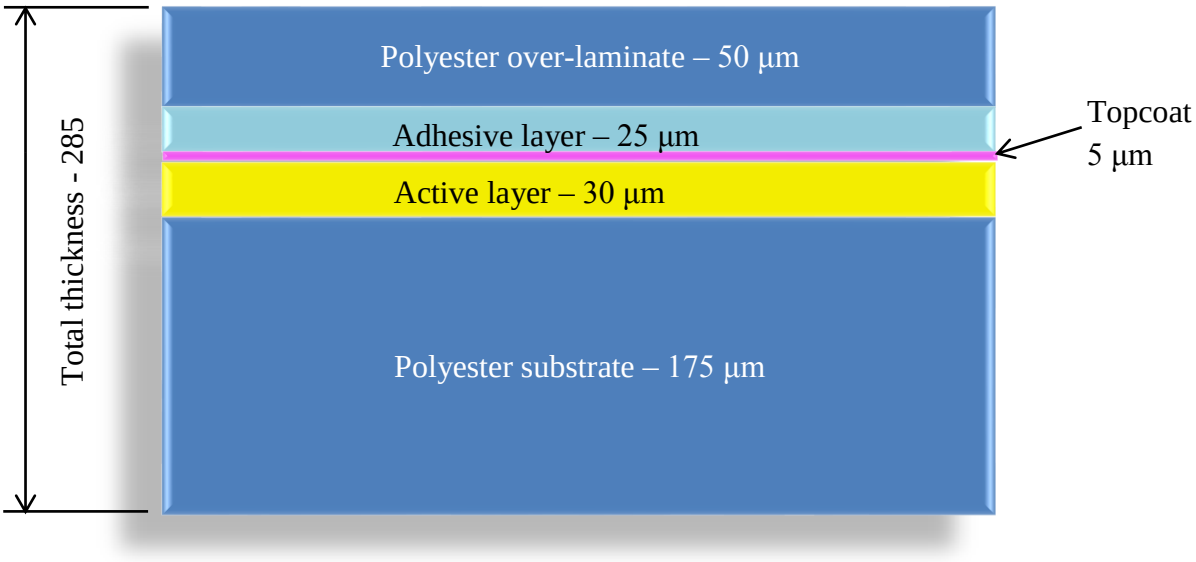

Fig. 2.28: Configuration of GAFCHROMIC® EBT2 dosimetry film

The over-laminate layer protects the topcoat and active layer from the effects of liquids, as well as from mechanical damage. The noticeable difference between the film and its predecessor (EBT) is the yellow color, due to a dye embodied into the active layer. The composition of the EBT2 film is near tissue equivalent, with an effective atomic number of 6.84.

2.5: Gamma index evaluation

The validation of the source model will be done using gamma (γ) index values calculated between MC and water tank data, as well in some cases MC and film data. Dose comparison can be done in various ways but the most useful of these is the γ index method. The γ index is a tool which is used to quantitatively compare multidimensional dose distributions[61]. The γ index compares two dose distributions; one is the reference profile and the other the comparison profile[62]. Fig. 2.29 shows a schematic presentation of the γ index tool for evaluating one-dimensional dose distributions with each other.

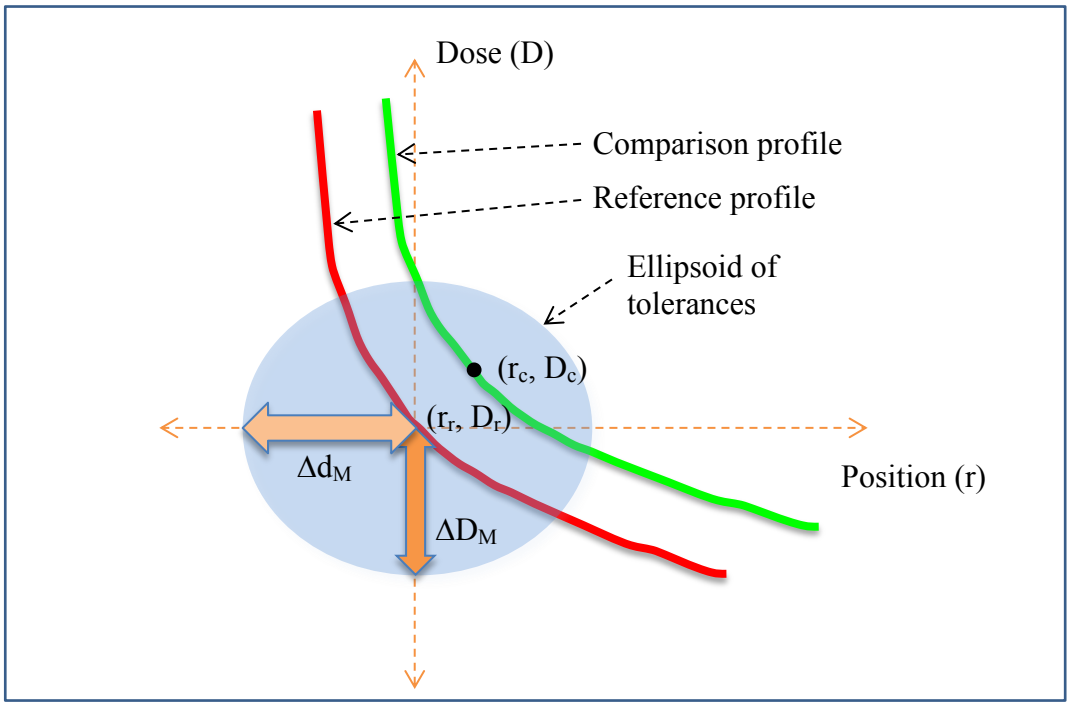

Fig. 2.29: Geometrical presentation of the gamma index and its dose difference and distance-to-agreement (DTA) criteria for a one-dimensional case

ΔD_M denotes the dose difference criterion and Δd_M for the distance-to-agreement criterion. The reference point on the reference profile is situated at the origin of the axial system and will have the coordinate of (r_r, D_r). The compared point (black dot) on the comparison profile will have the coordinate of (r_c, D_c).

The acceptance criteria create an ellipsoid surface which is defined by:

$$\sqrt{\frac{\Delta r^2}{\Delta d_M^2}+\frac{\Delta D^2}{\Delta D_M^2}}=1 \qquad \text{(Eq. 31)}$$

where

$$\Delta r=\left|r_r-r_c\right| \qquad \text{(Eq. 32)}$$

is the absolute distance between the reference and compared points, and

$$\Delta D=D_c(r_c)-D_r(r_r) \qquad \text{(Eq. 33)}$$

is the dose difference at position $\boldsymbol{r}_c$ relative to reference dose D_r in $\boldsymbol{r}_r$. The ellipsoid of acceptance needs to contain at least one point (r_c, D_c) for the compared distribution to match the reference dose in $\boldsymbol{r}_r$, for which:

$$\Gamma_r(r_c,D_c)\equiv\sqrt{\frac{\Delta r^2}{\Delta r_M^2}+\frac{\Delta D^2}{\Delta D_M^2}}\le 1 \qquad \text{(Eq. 34)}$$

The accuracy of the compared profile is determined by the smallest deviation point from the reference point, thus the point where $\Gamma_r(\boldsymbol{r}_c, D_c)$ is minimal. This minimal value is referred to as the quality index $\gamma(\boldsymbol{r}_r)$ of the reference point. When $\gamma(\boldsymbol{r}_r) \le 1$, the specified acceptance criteria has been met and comparison has passed.

In general, if the reference coordinate (r_r, D_r) falls within the boundaries of the ellipse in Eq. 31, then $\Gamma_r(r_c,D_c)<1$.

Chapter 3 - Methods & Materials

3.1: Water tank measurements

In order to validate the MC source model that will be developed in this study, benchmarking dose profile data were obtained in a Scanditronics Wellhöfer Blue Phantom using OmniPro^{TM} Accept 6.4a (IBA Dosimetry GmbH, Schwarzenbruck, Germany) scanning software. A CC01 ionization chamber was used for signal detection of the 1×1 to 5×5 cm^2 square field size (FS) apertures, with the CC13 chamber used for larger square, rectangular and off-set FS apertures. Linear interpolation to 2 mm step width, as well as least square smoothing, was performed on all water tank (WT) measured data. For irregular FS apertures GAFCHROMIC® EBT2 film was used to obtain 2D dose distributions in a RW3 solid phantom.

3.2: GAFCHROMIC® EBT2 film measurements

It was also necessary to characterize the document scanner that was used to obtain images of the scanned film. This is to verify that it will give consistent and reproducible results. Afterwards the conversion of pixel value to dose can be performed through film calibration. All films were scanned 24 hours after irradiation on the Linac, as suggested by ISP[36]. This is due to post-exposure density growth of the polymers occurring in the film. A HP^{TM} Photosmart C4683 and Canon^{TM} CanoScan N670U document scanners were used. Both scanners have a color depth of 48-bit. The resulting JPEG images were inverted and the red channel was analyzed using ImageJ software. ImageJ is a Java-based imaging processing program, freely available to the public, which was developed at the National Institute of Health[63]. The software can analyse both JPEG and TIFF files. Both scanners' file format

was set to JPEG by default. The Color Profiler tool in ImageJ was used to extract the red color channel from each ***rgb*** color channel, as it produces the maximum response to radiation[36].

3.2.1: Film preparation for scanner property testing

GAFCHROMIC® EBT2 films Lot # A09031001B were used in all measurements. A single film sheet of 25.4 cm × 20.3 cm (10" × 8") size was used and cut into smaller pieces of 2.5 cm × 2.0 cm. Ten rows and ten columns of film pieces can be obtained from a single sheet of film, thus producing a hundred film pieces. Each small film piece was placed at a depth of maximum dose (d_{max}) in a solid water phantom. They were irradiated with 100 cGy for each photon beam energy of 6, 8 and 15 MV on an Elekta^{TM} Precise Linac. The films were centered on the CAX. Radiation FS of 10×10 cm^2 was used with source-to-surface distance (SSD) of 100 cm. Each individual photon energy has a d_{max} value of 1.5, 2.0 and 2.5 cm in water for the respective photon energies. The film pieces were placed on top of 5 cm phantom thickness slabs, which served as a backscattering medium. These irradiated films were used to determine the scanner properties. The resolution was set to 300 dots per inch (dpi) for both scanners.

3.2.2: Scanner properties

3.2.2.1: Scanner dependency

The same set of film pieces were scanned on both the HP^{TM} Photosmart C4683 and Canon^{TM} CanoScan N670U document scanners on the same day to investigate any similarities and/or differences in the response from the film.

3.2.2.2: Scanner uniformity

Some scanners have a non-uniform response across their scanning surface. In such cases, non-uniform corrections are required[64]. In order to test the uniformity of the Canon™ CanoScan N670U document scanner and to evaluate if non-uniformity corrections are necessary, a single irradiated film piece was placed at 15 equally spaced locations on the scanning surface (Fig. 3.1). A region of interest (ROI) of 160×160 pixels was used for all film pieces during the analyses. The average red color component for each ROI was obtained and the uniformity calculated using the following equation:

$$U = 100\left(\frac{\max - \min}{\max + \min}\right)\% \qquad \text{(Eq. 35)}$$

where max and min indicates the maximum and minimum average red pixel values over the 15 ROI's as shown in Fig. 3.1.

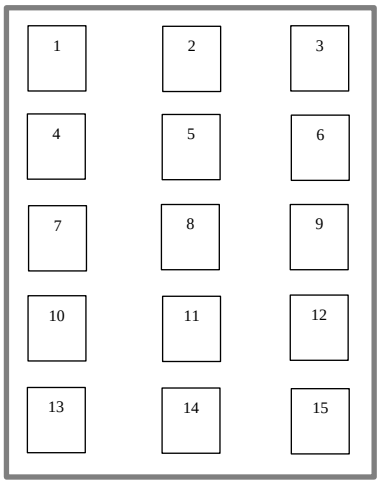

Fig. 3.1: Placements of single film piece over the scanner surface for uniformity measurements.

3.2.2.3: Film orientation

Park *et al*[65] reported an average dose decrease by 1.5 - 2.3% in reflection mode for EBT2 film rotating from portrait to landscape orientation. In order to compare the response of the film in different

scanning orientations, a single irradiated film piece was placed at position number 8 (Fig. 3.1) on the scanning surface of the scanner. It was scanned in both the portrait and landscape orientation respectively. A ROI of 160×160 pixels were drawn in on the JPEG image for analysis. The response difference was determined using the difference percentage equation as shown below:

$$error\% = 100 \times \left| \frac{Av_p - Av_l}{Av_p} \right| \quad \text{(Eq. 36)}$$

with Av_p and Av_l the average response values for the portrait and landscape orientations respectively.

3.2.2.4: Scanning side

In order to determine the influence of the scanning side of the film on its response, film pieces were scanned in the face-up and face-down orientation. A ROI of 160×160 pixels where used to evaluate the average pixel value for both film orientations.

3.2.2.5: Scanning repeatability

A single irradiated film piece was scanned 10 times at the same scanning position on the scanning surface of the scanner in order to determine its repeatability. The film piece was placed at position number 8 (Fig. 3.1) in the portrait orientation. The average pixel response in a ROI of 160×160 pixels was obtained, as well as a standard deviation, over the 10 scans.

3.2.3: Film calibration

RW3 solid water slabs were used: 5 × 1 cm slabs for backscatter and 1.5, 2.0 and 2.5 cm slabs as build-up for the 6, 8 and 15 MV energy beams respectively. Thus, the pieces were placed at each energy's d_{max} depth. 100 cm SSD and 10x10 cm^2 FS were used.

Ten pieces of film was used per energy to determine its pixel-to-dose curve. One film piece was set aside for background. The remaining ones were irradiated between 10 and 300 cGy at regular dose intervals. The film pieces were scanned approximately 24 hours after irradiation using the Canon™ CanoScan N670U document scanner, with a scanning resolution set at 75 dpi. After the films were scanned, a ROI of 72×72 pixels was drawn in for each film piece during analyses using ImageJ. The average red pixel value in the ROI was obtained for each film piece and, along with its corresponding absorbed dose, a calibration (pixel-to-dose) curve was obtained.

3.2.4: Dose measurement for irregular fields

A single EBT2 film piece was sandwiched between RW3 solid water slabs; 5 cm was used for backscatter and 5 cm on top of the film for build-up. The Linac head's cross-wire projection was traced onto the sides of the film (Fig. 3.2) in order to position the scanned image correctly with the simulated dose data. The markings were made using a 30×30 cm^2 FS aperture. The film's position was at isocentre, thus having a SSD of 95 cm.

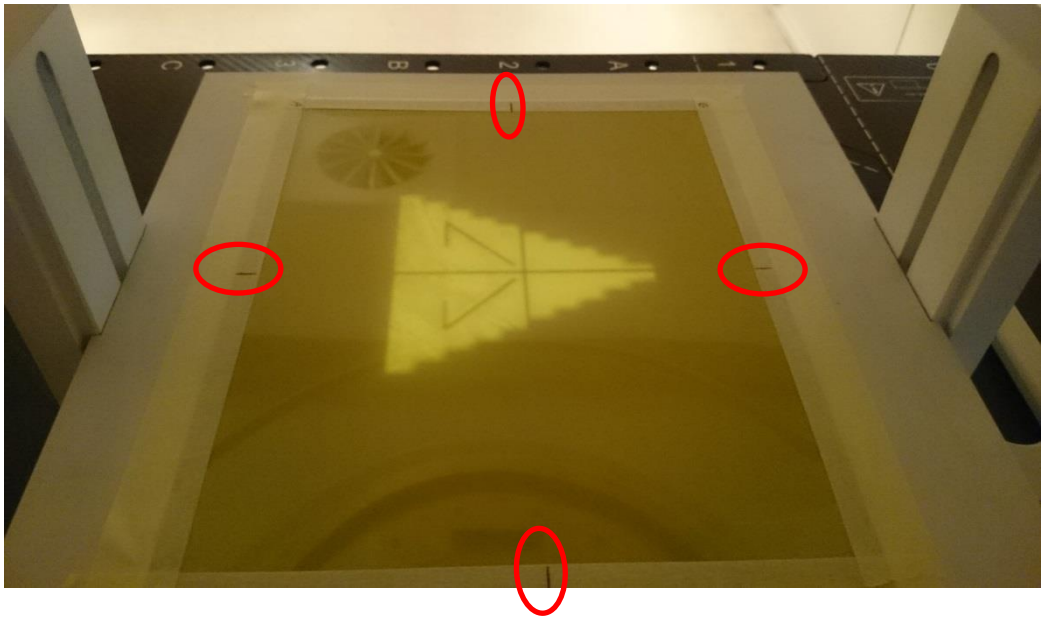

Fig. 3.2: Picture of *Triangle* aperture with the cross-wire markings (encircled in red) on the sides of the film.

3.2.4.1: Scanning and analyses of films

All the film pieces were scanned into JPEG format using the document scanner, approximately 24 hours after irradiation. Scanning resolution of the Canon™ CanoScan N670U document scanner was set at 75 dpi and analyzed in ImageJ.

3.2.5: Output factors

Output factors (OF's) for the Precise Linac were measured with a CC13 ionization chamber at a depth of 10 cm in water and a SSD of 90 cm for FS's ranging from 4×4 to 40×40 cm^2. For the smaller FS's, GAFCHROMIC® EBT2 film was used to obtain the OF's for the FS's ranging from 1×1 to 5×5 cm^2, along with a 10×10 cm^2 FS as reference. RW3 solid water slabs were used as phantom medium: 5 cm thickness for backscatter and 10 cm thickness for build-up were used for the all energies. The film pieces were placed at the isocentre. 100 monitor units (MU's) were delivered to the film. The

irradiated film pieces were scanned after 24 hours using the Canon™ CanoScan N670U document scanner with a scanning resolution of 75 dpi and analyzed in ImageJ.

3.3: The Graphical User Interface (GUI) as a tool to aid in the estimation of the initial exit fluence for the Monte Carlo source model.

An IDL[66] GUI was developed where the MC source files can be generated in order to perform dosimetry simulations in the DOSXYZnrc MC code. The GUI makes use of the photon energy spectrum, as well as photon and electron fluence data for a specific energy beam in order to generate a source file. These fluence data are generated using mathematical models.

Fig. 3.3 displays the platform in the GUI in order to create a source model. In the *FIELD SIZES* window, the X1, X2, Y1 and Y2 jaws have drop down menus to select the position where each jaw should be. *BEAM NUMBER, PHASE SPACE PLANE SSD* and *LINAC BEAM's* drop down menus are to select the number of beams if multiple beams will be generated for a plan; the distance from the source to the phase space file position and the Linac with its corresponding energy respectively. The *Wedge* and *MLC* tick boxes are to activate the selected component in the fluence code. The *RTPLAN* tick box is to load a RTPLAN DICOM file from a planning system and the plan's parameters will be used to generate a source file. The tick boxes of *PhotSpec, ElecSpec, PrimFl, JawFl* and *MLCFl* are to activate the photon energy spectrum, electron energy spectrum, primary collimator fluence, jaw fluence and MLC fluence respectively to be displayed.

The *MLC, PSPEC, ESPEC, PRIMFLU, JAWFLU* and *MLCFLU* buttons are used to access the MLC (Fig. 3.4), photon energy spectrum (Fig. 3.5), electron energy spectrum (Fig. 3.6), primary collimator fluence (Fig. 3.7), jaw fluence (Fig. 3.8 and 3.9) and MLC fluence (Fig. 3.10) platforms respectively.

The *Run* button runs the IDL program to generate a source file that can be named when selecting the *Save source file as:* - button.

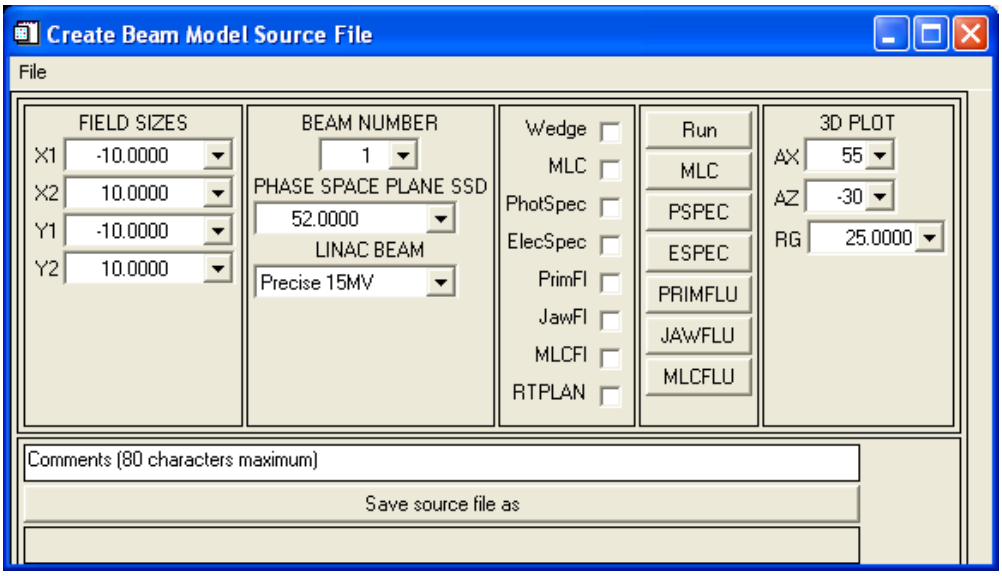

Fig. 3.3: Graphical user interface (GUI) to create source input files.

In Fig. 3.4, the left and right MLC bank leafs' ranging from leaf number 1 to 40 are displayed, as well as their drop down menus in order to select their position in centimeters individually. These are the openings at isocentre.

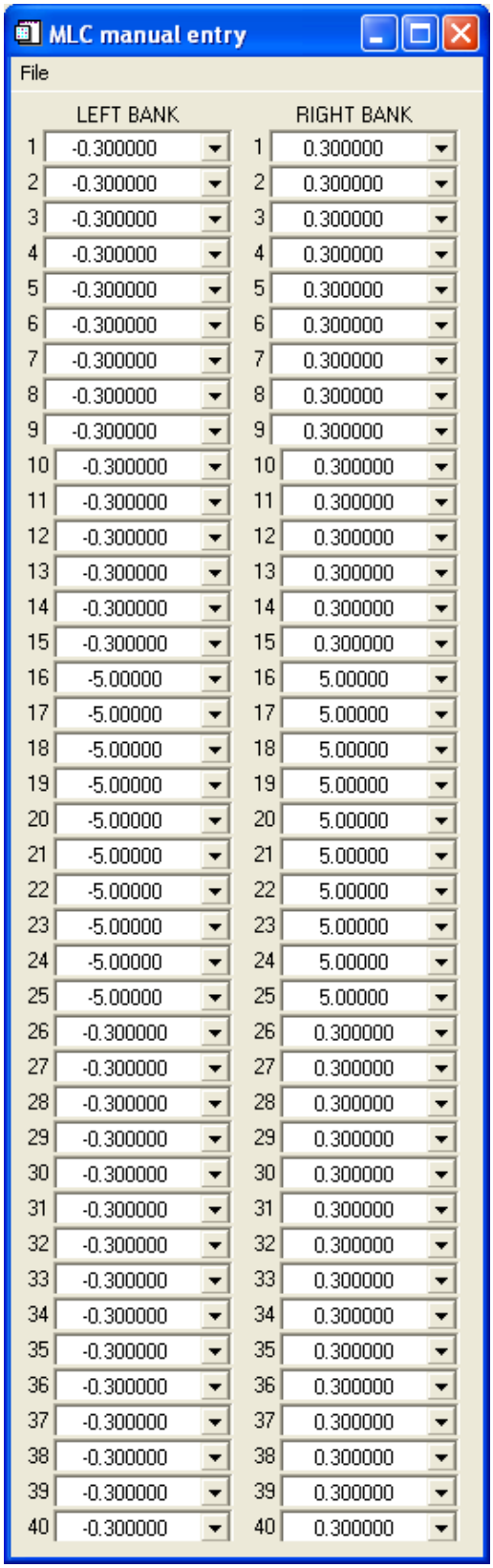

Fig. 3.4: GUI to select MLC positions at isocentre.

Fig. 3.5 shows the GUI to modify the photon energy spectrum's parameters. The *DEFAULT VALUES* window is the set of initial values. The *TRIAL VALUES* widget sliders are used to modify the parameters. The *Reset* buttons reset the trial value back to its default value. The parameters, as described in Section 2.1.1, are as follows: *E0* is the maximum electron energy falling onto the tungsten target (Eqs. 1 and 2); *alfa0* and *alfa1* are the values in Eq. 3; *t0*, *t1*, *t2*, *t3* and *t4* are the values for the polynomial function (Eq. 5) for the 15 MV energy beam's flattening filter. For the 6 and 8 MV energy beams, the default values will be that which is found in Eq. 4.

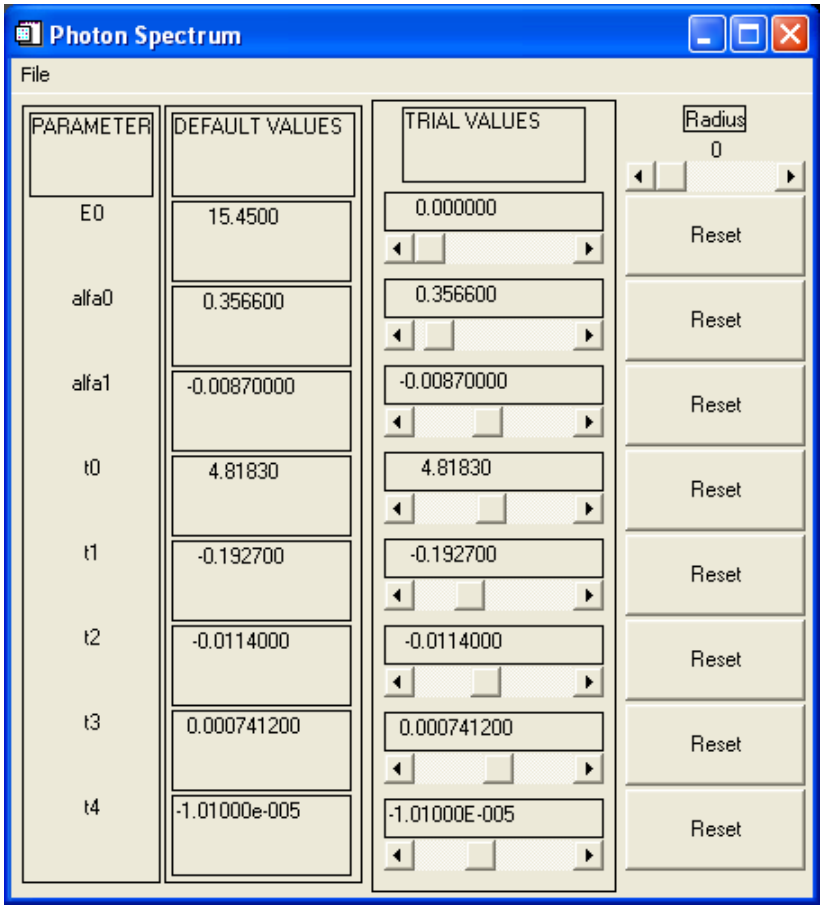

Fig. 3.5: GUI to modify photon energy spectrum parameters.

Fig. 3.6 shows the GUI to modify the contamination electron energy spectrum. The parameters, as described in Section 2.1.2, are as follows: *Emax* is the maximum contamination electron energy; *ee0*, *ee1*, *ee2*, *ee3*, *ee4* and *ee5* are the coefficients for the polynomial function in Eq. 6.

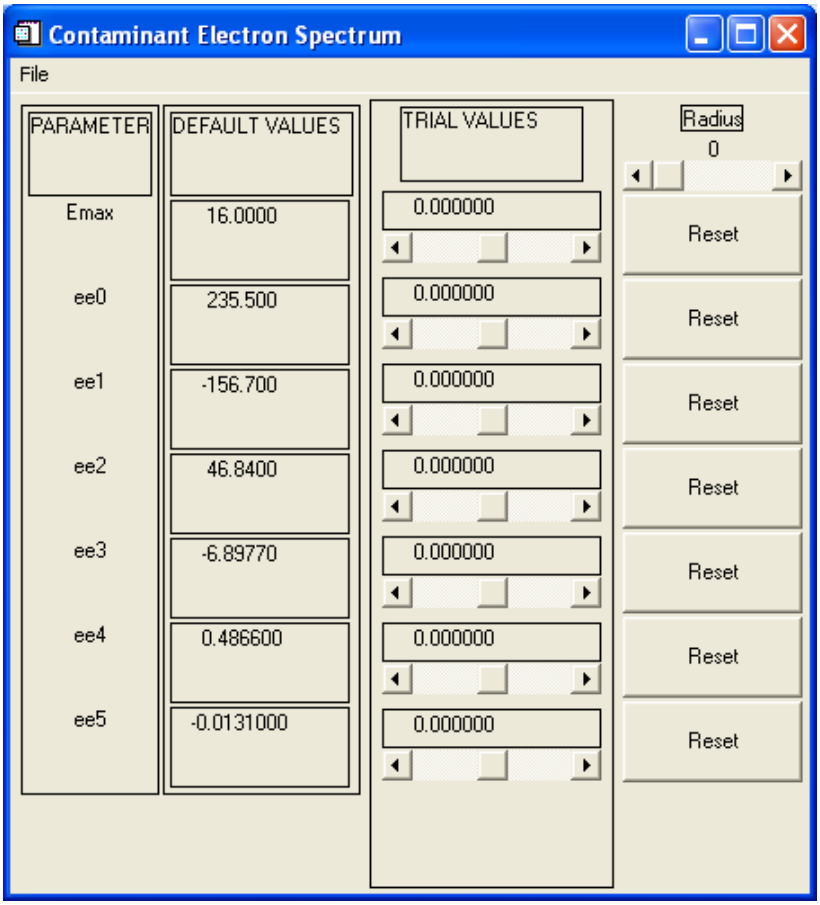

Fig. 3.6: GUI to modify electron energy spectrum parameters.

Fig. 3.7 shows the GUI to modify the photon fluence. The parameters, as described in Section 2.1.3, are as follows: *pj* is the amplitude of the Gaussian function (Eq. 7); *psig4* is the FWHM of the Gaussian function in the target's fluence (Eq. 7); *px3* is the radial position of the primary collimator's fluence (Eqs. 8 - 10); *psig1* is the FWHM of the error function (Eqs. 8 - 10); *ph* is the amplitude of the decreasing function (Eq. 8); *pmu1* is the 'decay' coefficient (Eq. 8); *pconst* is a constant (Eq. 8); *pmu2* is the attenuation coefficient of the flattening filter's fluence (Eq. 11); *pt0*, *pt1*, *pt2*, *pt3* and *pt4* are the coefficients for the polynomial function (Eq. 13) for the 15 MV energy beam flattening filter. For the 6 and 8 MV energy beams, the default values will be that which is found in Eq. 12.

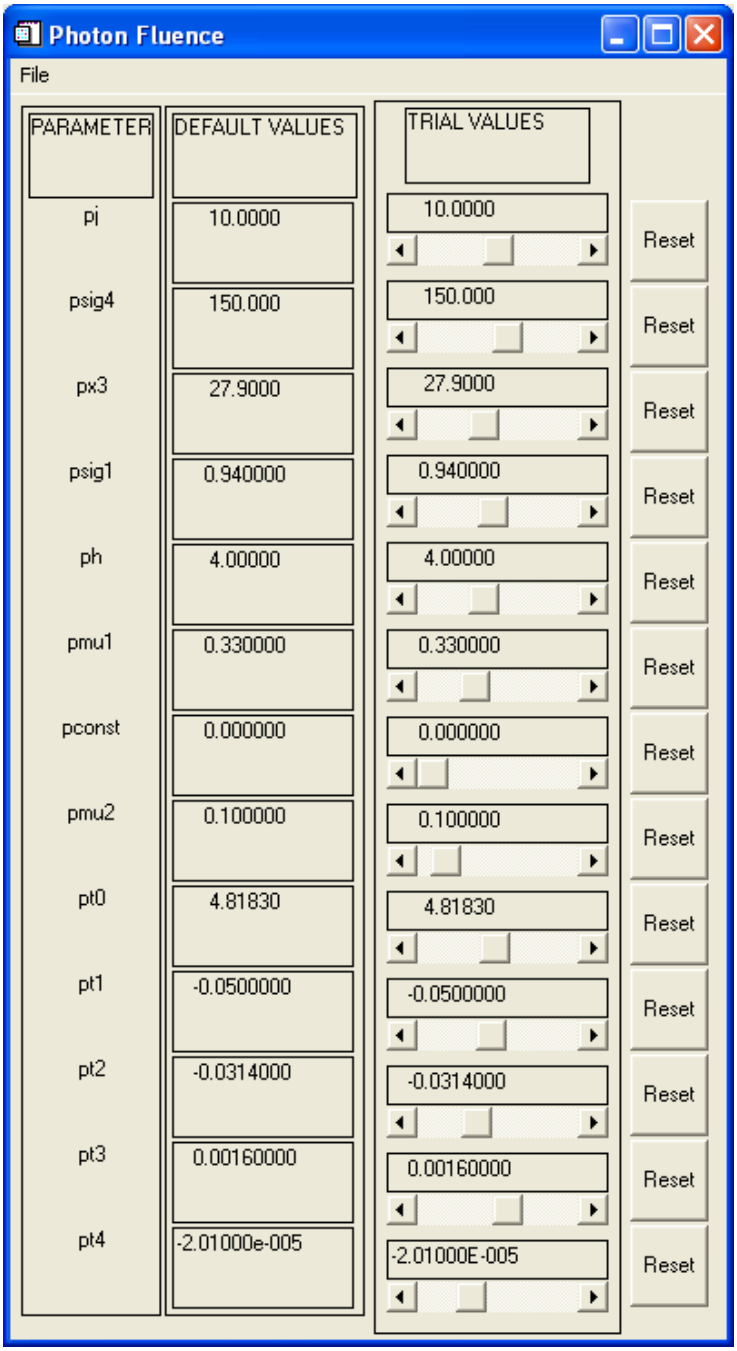

Figure 3.7: GUI to modify photon fluence parameters before and after the flattening filter.

Fig. 3.8 shows the GUI to modify the jaw fluence parameters. The parameters, as described in Section 2.1.3.4, are as follows: *sigma_jaws* is the FWHM of the Gaussian function in the jaw's fluence (Eqs. 15 and 16); *trans_jaws* is the maximum transmitted fluence through the jaws (Eq. 16); *aa_jaws* is a value for the exponential decreasing function (Eq. 17); *mu_out0* and *mu_out1* are values in the exponential decreasing function (Eq. 17) to model fluence under the jaws.

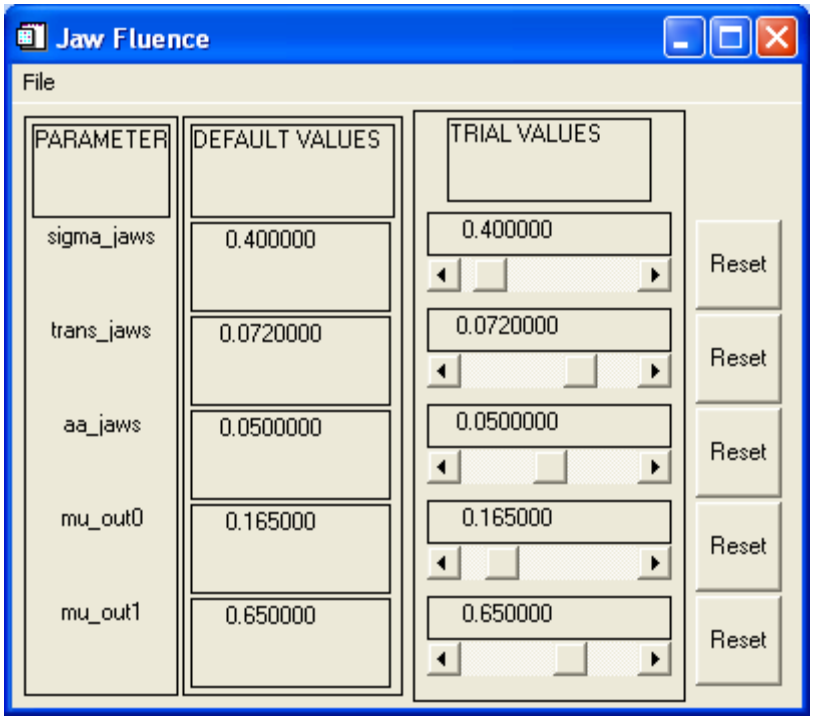

Fig. 3.8: GUI to modify jaw fluence parameters.

Adjustments were made in the IDL based GUI to expand the single *sigma_jaws* parameter to be different for the individual X1, X2, Y1 and Y2 jaws. The same was done for the transmission parameter (*trans_jaws*) in the decaying function for the X- and Y-jaws, as shown in Fig. 3.9.

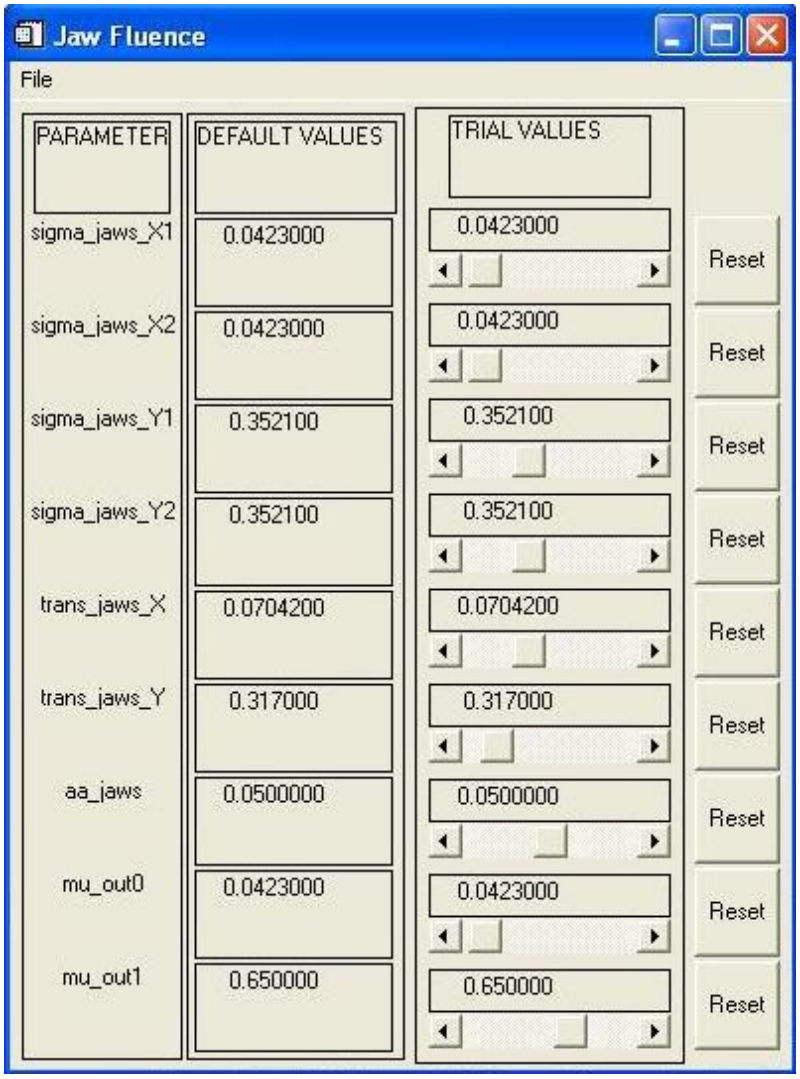

Fig. 3.9: GUI to modify jaw fluence parameters, after modifications were done in the code for the *sigma_jaws* and *trans_jaws* parameters.

Fig. 3.10 shows the GUI to modify the MLC fluence parameters. These parameters, as described in Section 2.1.3.5, are as follows: *sigmax_mlc* and *sigmay_mlc* is the FWHM of the error functions for the MLC's fluence in the X- and Y-directions respectively (Eqs. 20 and 21); *trans_mlc* is the maximum transmission through the MLC (Eq. 21); *aa_mlc* is a coefficient for the decay function (Eq. 22); *mu_out0* and *mu_out1* are values in the decaying function (Eq. 22).

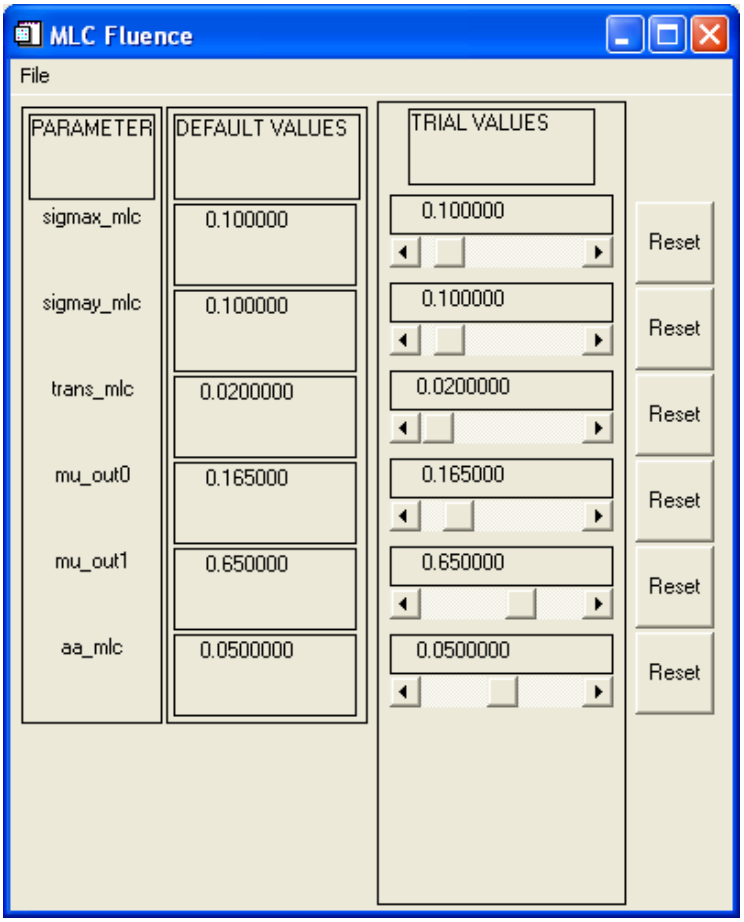

Fig. 3.10: GUI to modify MLC fluence parameters.

3.3.1 Square field aperture source files

The default values for the various parameters in the GUI's (Fig. 3.6 – 3.10) were used to produce the fluence and energy spectra for the MC source model. Dose distributions were calculated. Percentage depth dose (PDD) and dose profiles were compared with measured benchmarked data. The gamma (γ) index was used as the metric to determine the correspondence between the MC and WT data. If the γ-index evaluation for the comparison did not pass, new source parameters were selected, until the comparison passed.

The range of square field sizes is as follow: 1×1, 2×2, 3×3, 4×4, 5×5, 7×7, 10×10, 12×12, 15×15, 20×20, 30×30 and 40×40 cm^2. Fig. 3.11 is an example of a 10×10 cm^2 source fluence input generated in the GUI in order to obtain simulated MC dose distributions and to compare it to the measured WT dose distributions.

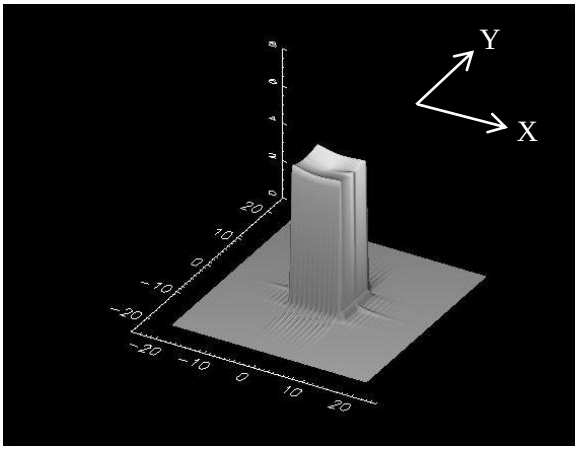

Fig. 3.11: 3D fluence map of 10×10 cm^2 square field aperture generated in the GUI for 6 MV beam. The white arrows indicate the X- and Y-directions.

3.3.2 Rectangular field aperture source files

The rectangular aperture configurations used to test the source model were 5×20, 20×5, 10×30 and 30×10 cm^2 in the X and Y directions, with Table 3.1 listing the X and Y jaws configurations for all the apertures.

Table 3.1: X and Y jaws configurations used for rectangular field shapes

Jaws	**5×20 cm^2**	**20×5 cm^2**	**10×30 cm^2**	**30×10 cm^2**
X1	-2.5	-10.0	-5.0	-15.0
X2	+2.5	+10.0	+5.0	+15.0
Y1	-10.0	-2.5	-15.0	-5.0
Y2	+10.0	+2.5	+15.0	+5.0

The MLC configurations for each above mentioned aperture are listed in Table 3.2 below.

Table 3.2: X and Y jaws with their corresponding MLC field used for rectangular field shapes

Jaws (cm^2)	**MLC (cm^2)**
5×20	6×20
20×5	22×5
10×30	12×30
30×10	32×10

The rectangular aperture source files were generated using the GUI. Parameters obtained for square aperture profiles from the initial trial runs (see section 4.2.1.3) were used, as listed in Tables 3.4 and 3.5 for the 6, 8 and 15 MV beams respectively. The equivalent FS formed by the X and Y jaws and MLC combinations for the 5×20 and 20×5 cm^2 apertures was determined to be 8.00 cm, using the following equation:

$$FS_{eq} = \frac{2xy}{x+y} \qquad \text{(Eq. 37)}$$

where *x* and y are the FS dimensions in the X-and Y-directions respectively.

This meant that the *sigma_jaws_X, sigma_jaws_Y, trans_jaws*_X and *trans_jaws*_Y parameter values for the 7×7 and 10×10 cm^2 FS were used to acquire their values at 8.00 cm equivalent FS using interpolation. For the 10×30 and 30×10 cm^2 apertures, the equivalent FS formed was determined using Eq. 37 to be 15.00 cm, thus the 15×15 cm^2 square FS *sigma_jaws_X, sigma_jaws_Y, trans_jaws*_X and *trans_jaws*_Y parameter values were used.

Table 3.4: Parameters for creating rectangular aperture shape source files

FS (cm^2)	***E0***			**Electron weight (%)**		
	6 MV	**8 MV**	**15 MV**	**6 MV**	**8 MV**	**15 MV**
5×20	7.00	8.73	12.96	0.0	0.0	0.1
20×5	7.00	8.73	12.96	0.0	0.0	0.1
10×30	7.00	9.01	12.96	0.1	0.2	0.4
30×10	7.00	9.01	12.96	0.1	0.2	0.4

Table 3.5: Jaw parameters for creating rectangular aperture shape source files for all energies

FS (cm^2)	***sigma_jaws_X***	***sigma_jaws_Y***	***trans_jaws_X***	***trans_jaws_Y***
5×20	0.155	0.352	0.048	0.247
20×5	0.155	0.352	0.048	0.247
10×30	0.155	0.352	0.087	0.423
30×10	0.155	0.352	0.087	0.423

Using the parameters from Tables 3.4 and 3.5, the 3D fluence maps of the source input files generated are displayed in Fig. 3.12.

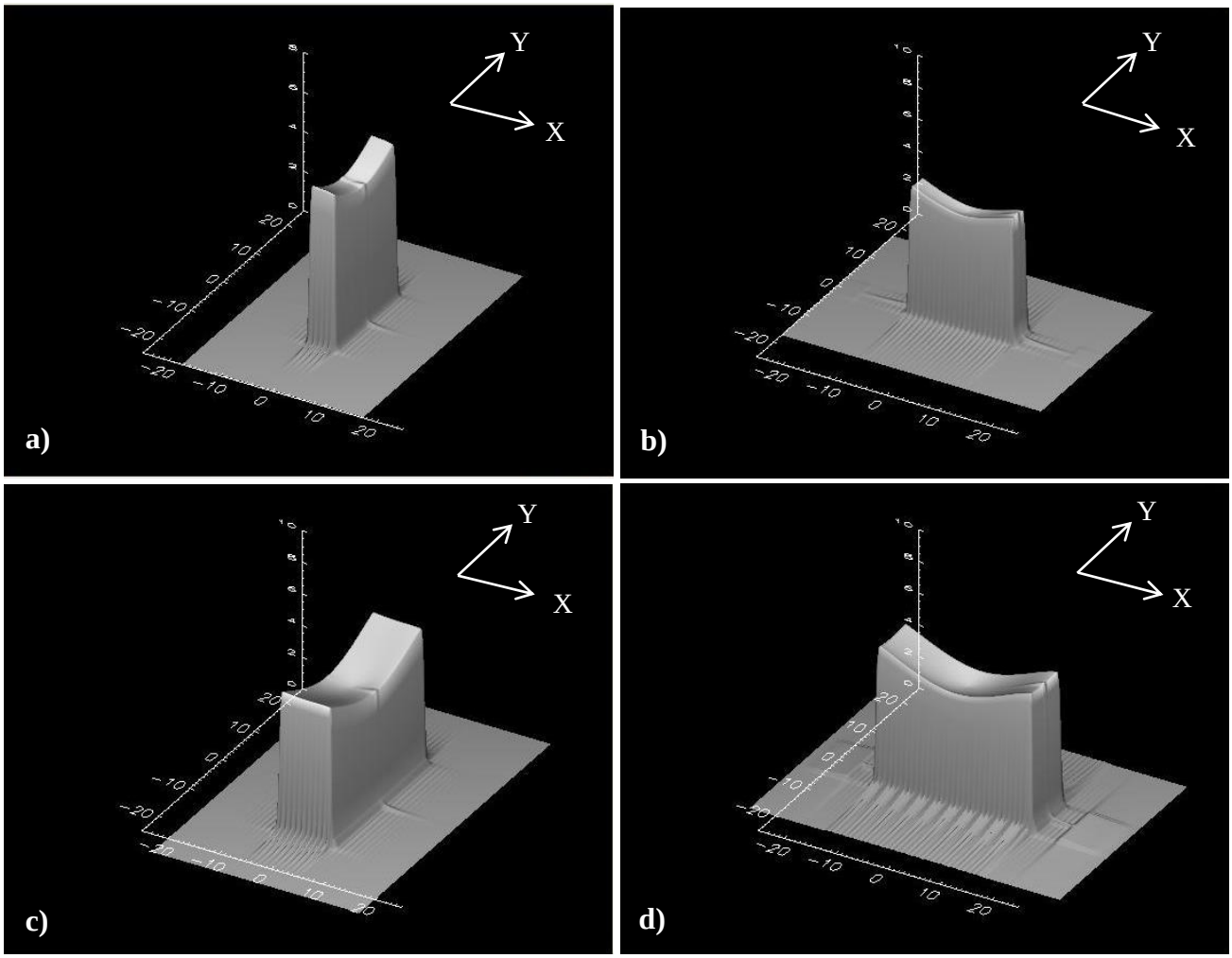

Fig. 3.12: 3D fluence maps of rectangular field apertures generated in the GUI having (a) 5×20, (b) 20×5, (c) 10×30, and (d) 30×10 cm^2 shapes for example the 6 MV beam. The white arrows indicate the X- and Y-directions.

3.3.3 Off-set field aperture source files

In order to test the source model in the off-axis directions, the following aperture configurations for off-set fields were used for all beam energies, as shown in Table 3.6. Table 3.6 also lists the X and Y jaws configurations for the off-set fields.

Table 3.6: X and Y jaws configurations used for off-set field apertures

Jaws	**10×10 cm^2, 2.5 cm X**	**10×10 cm^2, -5.0 cm Y**	**15×15 cm^2, -3.0 cm Y**	**15×15 cm^2, 7.5 cm X**	**20×20 cm^2, -5.0 cm X**	**20×20 cm^2, 10.0 cm Y**
X1	-2.5	-5.0	-7.5	0.0	-15.0	-10.0
X2	7.5	5.0	7.5	15.0	5.0	10.0
Y1	-5.0	-10.0	-10.5	-7.5	-10.0	0.0
Y2	5.0	0.0	4.5	7.5	10.0	20.0

Parameter values obtained for 10×10, 15×15 and 20×20 cm^2 square apertures for all energies (section 4.2.1.3) were used for the off-set source files using the GUI. 3D fluence maps of the source input files generated are displayed along with beams-eye-view (BEV) illustrations of the directions of the off-sets in Fig. 3.13 – 3.18.

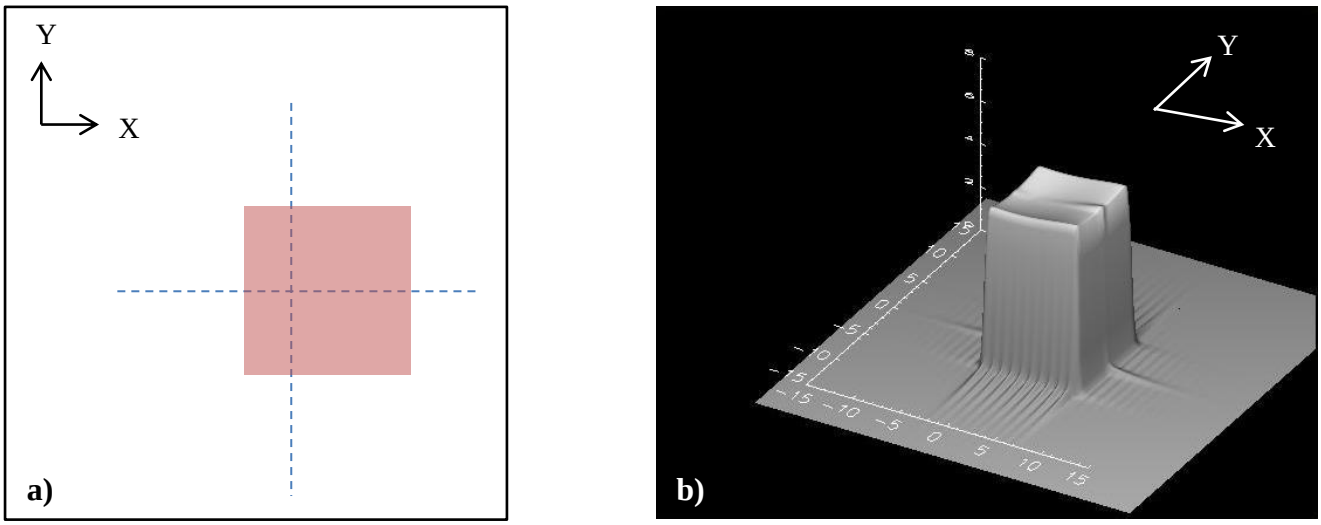

Fig. 3.13: (a) BEV illustration of the 2.5 cm off-axis shift in the X-direction, (b) 3D fluence map generated in IDL of the 10×10 cm^2 aperture off-set 2.5 cm off-axis for 6 MV beam. The blue dash lines in (a) indicates the CAX.

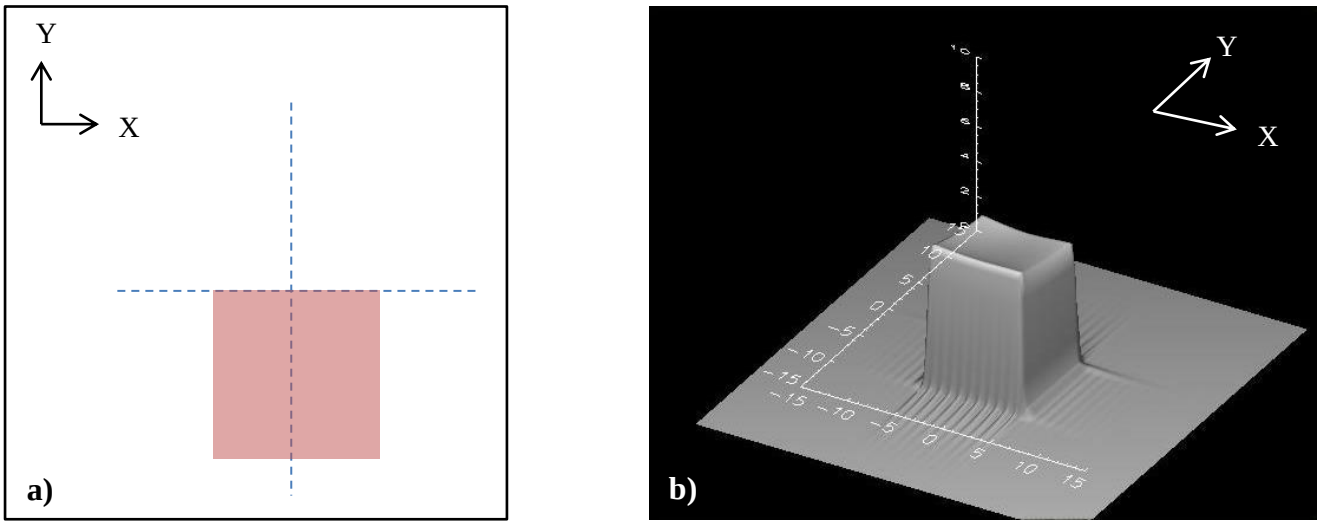

Fig. 3.14: (a) BEV illustration of the -5.0 cm off-axis shift in the Y-direction, (b) 3D fluence map generated in IDL of the 10×10 cm^2 aperture off-set -5.0 cm off-axis for 6 MV beam. The blue dash lines in (a) indicates the CAX.

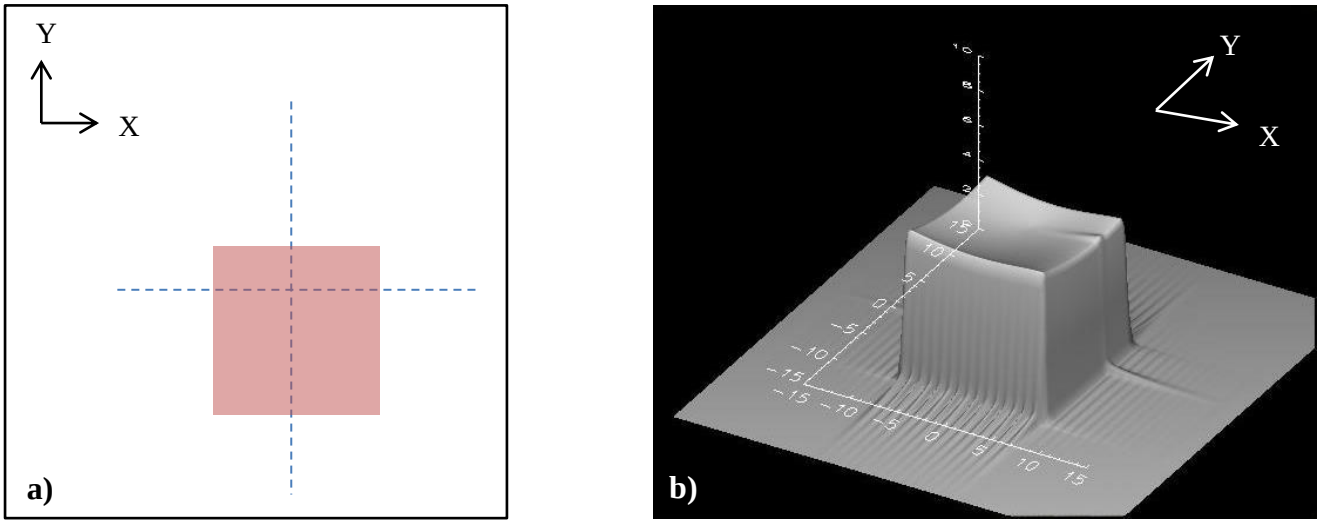

Fig. 3.15: (a) BEV illustration of the -3.0 cm off-axis shift in the Y-direction, (b) 3D fluence map generated in IDL of the 15×15 cm^2 aperture off-set -3.0 cm off-axis for 8 MV beam. The blue dash lines in (a) indicates the CAX.

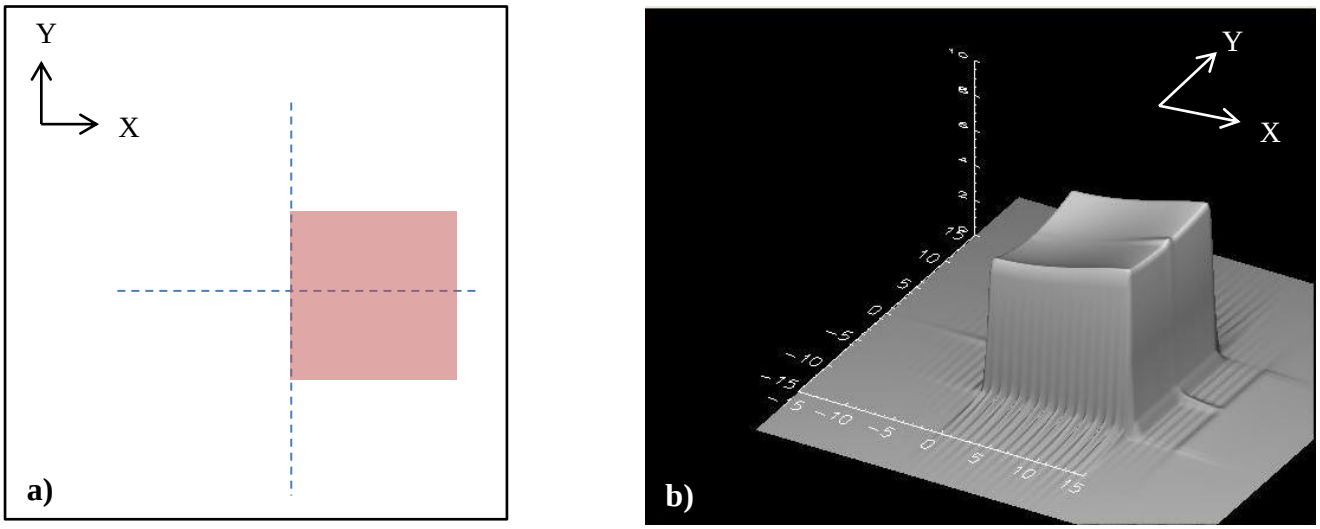

Fig. 3.16: (a) BEV illustration of the 7.5 cm off-axis shift in the X-direction, (b) 3D fluence map generated in IDL of the 15×15 cm^2 aperture off-set 7.5 cm off-axis for 8 MV beam. The blue dash lines in (a) indicates the CAX.

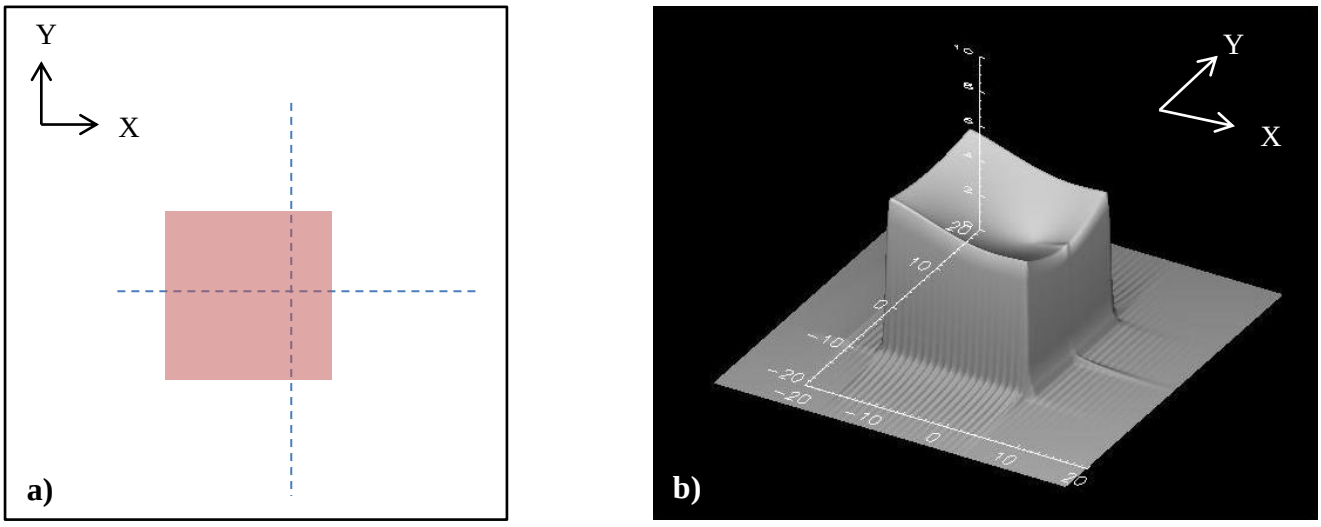

Fig. 3.17: (a) BEV illustration of the -5.0 cm off-axis shift in the X-direction, (b) 3D fluence map generated in IDL of the 20×20 cm^2 aperture off-set -5.0 cm off-axis for 15 MV beam. The blue dash lines in (a) indicates the CAX.

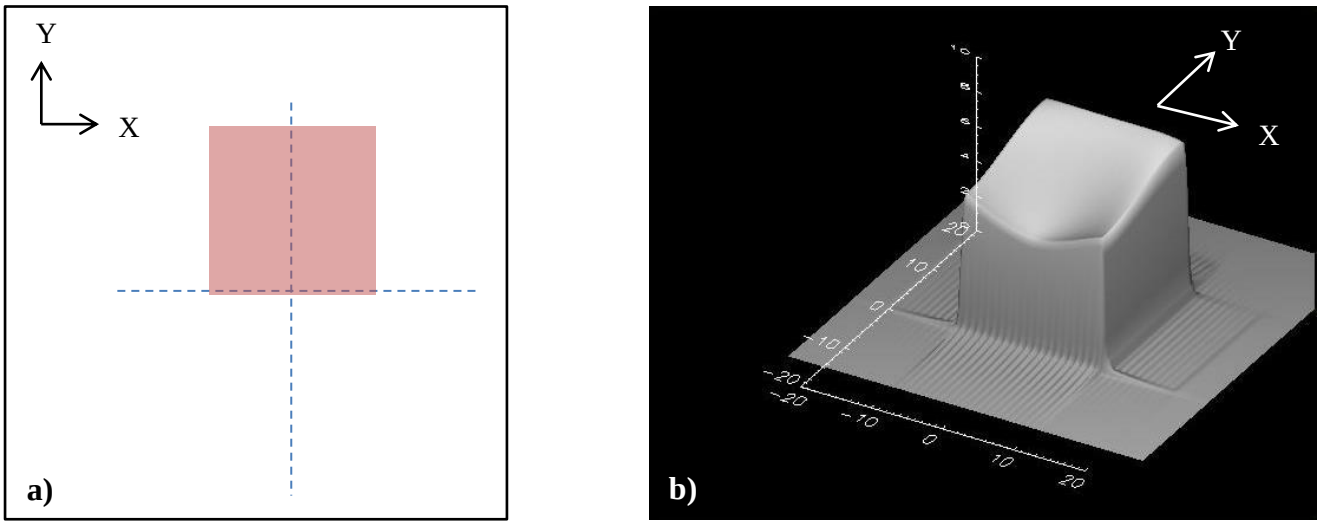

Fig. 3.18: (a) BEV illustration of the 10.0 cm off-axis shift in the Y-direction, (b) 3D fluence map generated in IDL of the 20×20 cm^2 aperture off-set 10.0 cm off-axis for 15 MV beam. The blue dash lines in (a) indicates the CAX.

3.3.4 Irregular field aperture source files

Irregular field apertures are created solely by MLC's with the X and Y jaws backing up at the outermost MLC positions of the aperture. For testing the source model parameters, three aperture geometries were generated on XiO® TPS, one for each of the 6, 8 and 15 MV energy beams. The geometries used are based on the ones used by Georg *et al*[67], with a few adjustments. A *Triangle*, *Arrow* and *Mirror E* field shape was set up for the 6, 8 and 15 MV beams. Tables 3.7 and 3.8 lists the X and Y jaws, along with the MLC configurations used for all three shapes respectively.

Table 3.7: X and Y jaws positions (cm) used for shown field shapes

Jaws	Triangle	Arrow	Mirror E
X1	-5.0	-7.5	-6.0
X2	5.0	7.5	6.0
Y1	-5.0	-2.5	-4.0
Y2	5.0	7.5	4.0

The generated MLC and jaw configurations are displayed in Fig. 3.19 (a) – (c), with the X and Y jaws displayed as red lines for all geometries.

Table 3.8: MLC leaf positions (cm) used for irregular field shapes

Leaf pair #	Triangle		Arrow		Mirror E	
	Y1	Y2	Y1	Y2	Y1	Y2
1	-0.3	0.3	2.2	2.8	-0.3	0.3
2	-0.3	0.3	2.2	2.8	-0.3	0.3
3	-0.3	0.3	2.2	2.8	-0.3	0.3
4	-0.3	0.3	2.2	2.8	-0.3	0.3
5	-0.3	0.3	2.2	2.8	-0.3	0.3
6	-0.3	0.3	2.2	2.8	-0.3	0.3
7	-0.3	0.3	2.2	2.8	-0.3	0.3
8	-0.3	0.3	2.2	2.8	-0.3	0.3
9	-0.3	0.3	2.2	2.8	-0.3	0.3
10	-0.3	0.3	2.2	2.8	-0.3	0.3
11	-0.3	0.3	2.2	2.8	-0.3	0.3
12	-0.3	0.3	2.2	2.8	-0.3	0.3
13	-0.3	0.3	2.2	7.5	-0.3	0.3
14	-0.3	0.3	1.5	7.2	-4.0	4.0
15	-5.0	5.0	0.8	6.5	-4.0	4.0
16	-5.0	5.0	0.2	5.8	-4.0	4.0
17	-4.5	4.5	-0.5	5.2	1.0	4.0
18	-4.0	4.0	-1.2	4.5	1.0	4.0
19	-3.5	3.5	-1.9	3.8	-4.0	4.0
20	-3.0	3.0	-2.5	3.2	-4.0	4.0
21	-2.5	2.5	-2.5	3.2	-4.0	4.0
22	-2.0	2.0	-1.9	3.8	-4.0	4.0
23	-1.5	1.5	-1.2	4.5	1.0	4.0
24	-1.0	1.0	-0.5	5.2	1.0	4.0
25	-0.5	0.5	0.2	5.8	-4.0	4.0
26	-0.5	0.5	0.8	6.5	-4.0	4.0
27	-0.3	0.3	1.5	7.2	-4.0	4.0
28	-0.3	0.3	2.2	7.5	-0.3	0.3
29	-0.3	0.3	2.2	2.8	-0.3	0.3
30	-0.3	0.3	2.2	2.8	-0.3	0.3
31	-0.3	0.3	2.2	2.8	-0.3	0.3
32	-0.3	0.3	2.2	2.8	-0.3	0.3
33	-0.3	0.3	2.2	2.8	-0.3	0.3
34	-0.3	0.3	2.2	2.8	-0.3	0.3
35	-0.3	0.3	2.2	2.8	-0.3	0.3
36	-0.3	0.3	2.2	2.8	-0.3	0.3
37	-0.3	0.3	2.2	2.8	-0.3	0.3
38	-0.3	0.3	2.2	2.8	-0.3	0.3
39	-0.3	0.3	2.2	2.8	-0.3	0.3
40	-0.3	0.3	2.2	2.8	-0.3	0.3

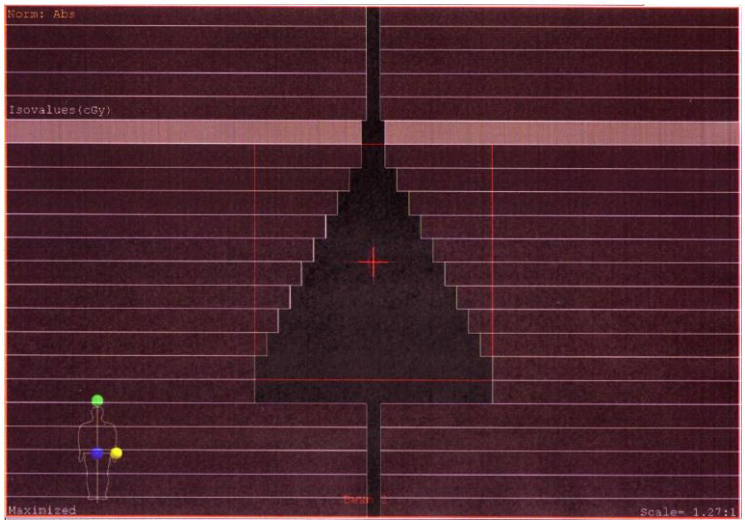

a)

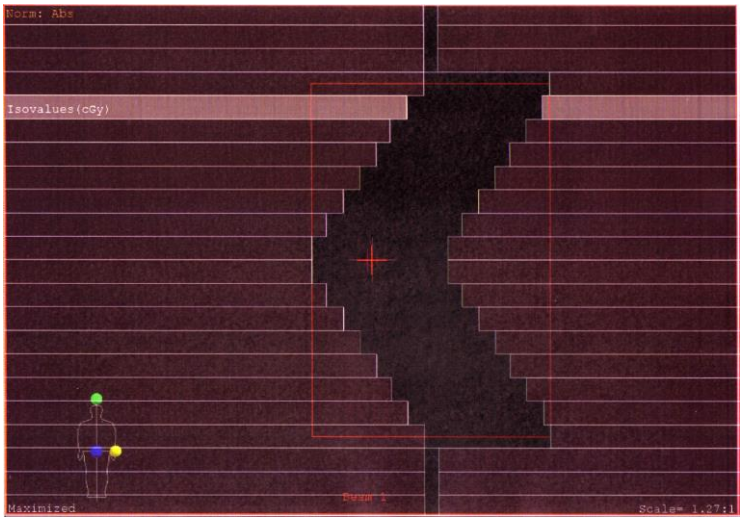

b)

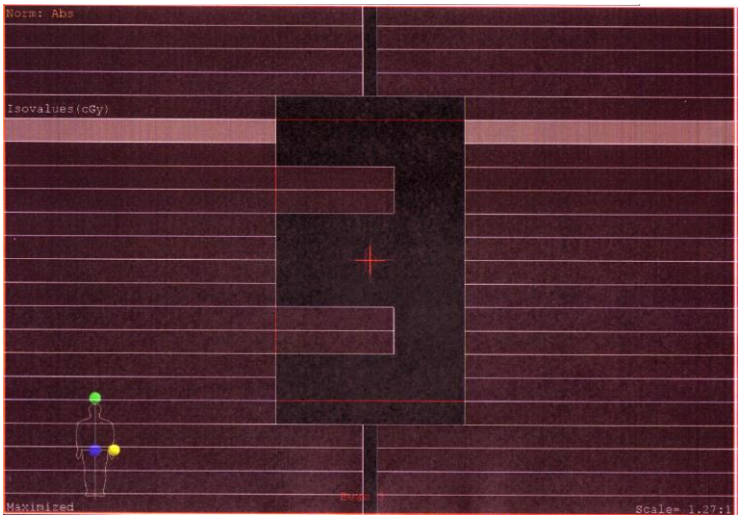

c)

Fig. 3.19: Irregular field apertures generated in XiO® having (a) triangle, (b) arrow and (c) mirror E shapes.

Note the XY jaws shown as red lines.

The irregular aperture source files were generated using the source model GUI. The equivalent FS formed by the MLC's for the *Triangle*, *Arrow* and *Mirror E* field shapes was determined to be 6.55, 7.25 and 7.36 cm respectively. This meant that the parameter values for the 7×7 cm^2 for all energies were used (section 4.2.1.3), as listed in Table 3.9.

Table 3.9: Parameter values for creating irregular aperture shape source files

Parameter	6 MV	8 MV	15 MV
psig4	62	118	240
E0	7.00	8.73	13.24
Electron weight (%)	0.0	0.0	0.1
sigma_jaws_X	0.155	0.155	0.155
sigma_jaws_Y	0.352	0.352	0.352
trans_jaws_X	0.039	0.039	0.039
trans_jaws_Y	0.211	0.211	0.211

Using the parameters from Table 3.9, the 3D fluence maps of the source input files generated are displayed in Fig. 3.20.

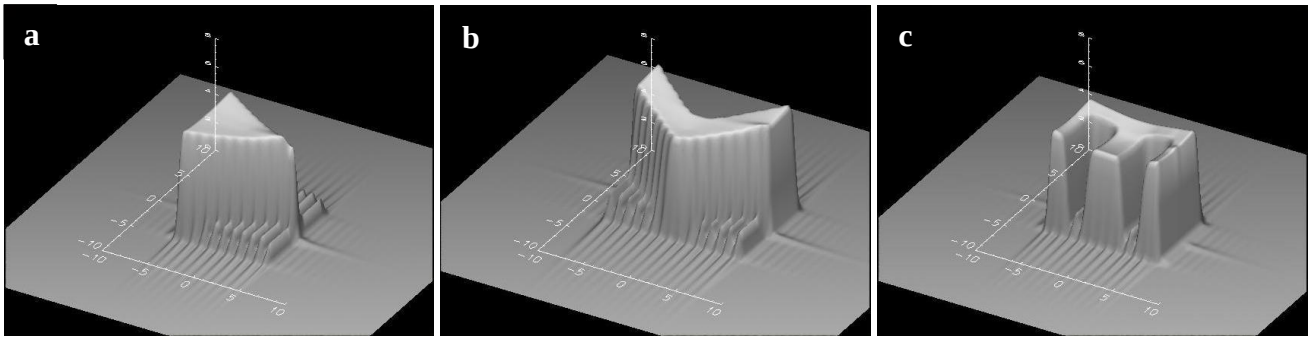

Fig. 3.20: 3D fluence maps of irregular field apertures generated in the GUI having (a) *Triangle*, (b) *Arrow* and (c) *Mirror E* shapes

3.4: Monte Carlo simulations

The EGSnrc MC code, DOSXYZnrc, was used for simulations. This was installed on a Linux openSUSE 10.3 platform on an Intel® Xeon® CPU with 8 processors, each with a speed of 2.33 GHz. In DOSXYZnrc, an input file was created using the PEGS4 cross-section data file, *700icru.pegs4dat*.

3.4.1 Phantom definitions

A non-CT data phantom was created by defining the properties of individual volume elements or voxels. Global electron (ECUT) and photon (PCUT) cut-off energy values were set at 0.7 and 0.01 MeV respectively for the phantom media that were generated for the dose simulations. These values are used as default at our facility. As soon as an electron or photon's total energy falls below the cut-off energy, its history is terminated and its energy deposited in the current region. The time required for a given calculation is strongly dependent on the value of ECUT and thus it is important to use as high a value as possible[25].

A water phantom material (*H2O700icru*) was constructed for dose simulations for square, rectangular and off-set FS apertures. GAFCHROMIC® EBT2 film was used for dose measurement for the irregular FS apertures. It was placed in the RW3 solid water slabs. The physical density of water and RW3 solid phantom is 0.998 and 1.045 g/cm^3 respectively. The elemental composition of water and RW3 is listed in Table 3.10, as used by Fujita *et al*[68]. Using these physical density and elemental composition information, a RW3 solid water phantom material (*RW3700icru*) was constructed in DOSXYZnrc for dose simulations.

Table 3.10: Elemental composition for a water and RW3 solid phantom material

Element	**Fractional by weight composition**	
	Water	**RW3**
H	0.1119	0.0759
C		0.9041
O	0.8881	0.0080
Ti		0.0120

3.4.1.1 Phantom voxel divisions for water tank dose simulations

The number of voxels in the X- and Y-directions and their sizes for the square FS apertures in the water phantom are listed in Tables 3.12 – 3.14. These dimensions and voxel groups were unchanged for all energies used.

The number of voxels in the Z-dimension and their sizes in the water phantom for the square, rectangular and off-set FS apertures are listed in Table 3.11. The widths of the voxels for the 6 MV beam were chosen in order to extract profiles at the following depths: 1.5, 5, 10 and 20 cm. Steeper dose gradients (build-up region for the PDD profiles) require smaller voxels. For this reason, the first group of 20 voxels have widths of 0.2 cm. For the 8 and 15 MV beams, the widths of the voxels were chosen to extract profiles at the following depths: 2, 2.5, 5, 10 and 20 cm. The minimum and maximum boundaries for the Z-dimension for all water phantom simulations are 0 and 31 cm respectively. The (*0,0,0*) coordinate is the isocentre location for all aperture simulations. This was the same for all energies.

Table 3.11: Z-dimension of water phantom for various energies. These were kept the same for all fields simulated.

6 MV		**8 & 15 MV**	
Width (cm)	# voxels	Width (cm)	# voxels
0.20	20	0.25	1
0.25	1	0.50	60
0.50	52	0.25	1
0.75	1		

Table 3.12: X- and Y-dimensions of water phantom for 1×1 – 5×5 cm^2 square FS apertures. The minimum and maximum X and Y boundaries are -20 and +20 cm respectively.

Width (cm)	**Number of voxels**	
	1×1 - 3×3 cm^2	**4×4 & 5×5 cm^2**
0.9	1	1
2.0	8	7
0.2	31	51
2.0	8	7
0.9	1	1

Table 3.13: X- and Y-dimensions of water phantom for 7×7 – 20×20 cm^2 square FS apertures. The minimum and maximum X and Y boundaries are -20 and +20 cm respectively.

Width (cm)	Number of voxels				
	7×7 cm^2	**10×10 cm^2**	**12×12 cm^2**	**15×15 cm^2**	**20×20 cm^2**
0.25	1	1	1	1	1
2.0	7	6	5	4	5
0.2	20	20	20	25	25
0.5	7	15	23	27	39
0.2	20	20	20	25	25
2.0	7	6	5	4	5
0.25	1	1	1	1	1

Table 3.14: X- and Y-dimensions of water phantom for 30×30 and 40×40 cm^2 square FS apertures. The minimum and maximum X and Y boundaries are -25 and +25 cm respectively.

30×30 cm^2		**40×40 cm^2**	
Width (cm)	**# voxels**	**Width (cm)**	**# voxels**
0.25	1	0.5	1
2.0	1	0.2	35
0.2	35	1.0	35
1.0	25	0.2	35
0.2	35	0.5	1
2.0	1		
0.25	1		

The minimum and maximum boundaries for the X- and Y-directions for rectangular FS apertures are listed in Table 3.15. The number of voxels for the X- and Y-directions and their sizes in the water phantom for rectangular FS apertures are listed in Table 3.16.

Table 3.15: Minimum and maximum boundaries for X- and Y-dimensions for rectangular FS apertures

Boundaries (cm)		**5×20 cm^2**	**20×5 cm^2**	**10×30 cm^2**	**30×10 cm^2**
X	Min	-20	-25	-20	-25
	Max	+20	+25	+20	+25
Y	Min	-25	-20	-25	-20
	Max	+25	+20	+25	+20

Table 3.16: X- and Y-dimensions of water phantom for rectangular FS apertures

Direction	5×20 cm²		20×5 cm²		10×30 cm²		30×10 cm²	
	Width (cm)	# voxels	Width (cm)	# voxels	Width (cm)	# voxels	Width (cm)	# voxels
X	0.9	1	0.25	1	0.25	1	0.5	1
	2.0	7	2.0	5	2.0	6	5.0	1
	0.2	51	0.2	25	0.2	20	0.2	35
	2.0	7	0.5	39	0.5	15	1.0	25
	0.9	1	0.2	25	0.2	20	0.2	35
			2.0	5	2.0	6	5.0	1
			0.25	1	0.25	1	0.5	1
Y	0.25	1	0.9	1	0.5	1	0.25	1
	2.0	5	2.0	7	5.0	1	2.0	6
	0.2	25	0.2	51	0.2	35	0.2	20
	0.5	39	2.0	7	1.0	25	0.5	15
	0.2	25	0.9	1	0.2	35	0.2	20
	2.0	5			5.0	1	2.0	6
	0.25	1			0.5	1	0.25	1

The number of voxels in the X- and Y-directions and their sizes in the water phantom for the off-set FS apertures are listed in Tables 3.18 – 3.20. The minimum and maximum boundaries for the X- and Y-directions for off-set FS apertures are listed in Table 3.17.

Table 3.17: Minimum and maximum boundaries for X- and Y-directions for off-set FS apertures in the water phantom.

Boundaries (cm)		10×10 cm², 2.5 cm X	10×10 cm², -5.0 cm Y	15×15 cm², -3.0 cm Y	15×15 cm², 7.5 cm X	20×20 cm², -5.0 cm X	20×20 cm², 10.0 cm Y
X	Min	-20	-20	-5	-20	-24	-25
	Max	+20	+20	+24	+20	+13	+25
Y	Min	-20	-20	-20	-20	-25	-6
	Max	+20	+20	+20	+20	+25	+25

Table 3.18: X- and Y-dimensions of water phantom for 10×10 cm^2 off-set FS apertures

Direction	**10×10 cm^2, 2.5 cm X**		**10×10 cm^2, -5.0 cm Y**	
	Width (cm)	# voxels	Width (cm)	# voxels
X	0.25	1	0.25	1
	2.0	7	2.0	6
	1.0	1	0.2	20
	0.2	20	0.5	15
	0.5	13	0.2	20
	0.2	20	2.0	6
	2.0	5	0.25	1
	0.25	1		
Y	0.25	1	0.25	1
	2.0	6	2.0	3
	0.2	20	0.2	25
	0.5	15	0.5	13
	0.2	20	0.2	25
	2.0	6	1.0	1
	0.25	1	2.0	8
			0.25	1

Table 3.19: X- and Y-dimensions of water phantom for 15×15 cm^2 off-set FS apertures

Direction	**15×15 cm^2, -3.0 cm Y**		**15×15 cm^2, 7.5 cm X**	
	Width (cm)	# voxels	Width (cm)	# voxels
X	0.25	1	0.25	1
	2.0	1	2.0	4
	0.2	20	0.2	25
	0.5	25	0.5	27
	0.2	30	0.5	25
	2.0	2	2.0	4
	0.25	1	0.25	1
Y	0.25	1	0.25	1
	2.0	4	2.0	2
	0.2	25	1.0	1
	0.5	27	0.2	30
	0.2	25	0.5	23
	2.0	4	0.2	25
	0.25	1	2.0	6
			0.25	1

Table 3.20: X- and Y-dimensions of water phantom for 20×20 cm^2 off-set FS apertures

Direction	**20×20 cm^2, -5.0 cm X**		**20×20 cm^2, 10.0 cm Y**	
	Width (cm)	# voxels	Width (cm)	# voxels
X	0.25	1	0.25	1
	2.0	2	2.0	5
	0.2	33	0.2	25
	0.5	33	0.5	39
	0.2	30	0.2	25
	2.0	2	2.0	5
	0.25	1	0.25	1
Y	0.25	1	0.25	1
	2.0	5	1.0	1
	0.2	25	0.2	30
	0.5	39	0.5	35
	0.2	25	0.2	25
	2.0	5	1.0	1
	0.25	1	0.25	1

3.4.1.2 RW3 phantom voxel divisions

The number of voxels for the X-, Y- and Z-dimensions in the RW3 phantom and their sizes are listed in Table 3.21. The minimum and maximum boundaries for the X- and Y-dimensions are -15 and 15 cm, for the Z-dimension the minimum and maximum boundaries are -5 and 5 cm.

Table 3.21: RW3 solid phantom dimensions for irregular FS apertures

Direction	**Triangle**		**Arrow & Mirror E**	
	Width (cm)	# voxels	Width (cm)	# voxels
X	7.0	1	5.0	1
	0.5	1	0.5	1
	0.2	75	0.2	95
	0.5	1	0.5	1
	7.0	1	5.0	1
Y	7.0	1	5.0	1
	0.5	1	0.5	1
	0.2	75	0.2	95
	0.5	1	0.5	1
	7.0	1	5.0	1
Z	0.1	1	0.1	1
	0.2	49	0.2	49
	0.1	1	0.1	1

3.4.2 Source parameters

The incident particle (IQIN) was set on photon. This is the charge of the incident beam in performing the dose calculations. The source type (ISOURCE) was set on *isource = 4: Beam characterization model*. The parameters for source type 4, using the DOSXYZnrc GUI, were as follows:

- The X, Y and Z-coordinates at isocenter was set at (*0,0,0*);
- Theta, phi and collimator angles were set at 180, 180 and 0 degrees respectively;
- Distance from source to isocenter was set at 48 cm, as the source input file was created in the IDL GUI at a phase-space plane at 52 cm below the target;
- File containing source parameters from BEAMDP was the source input file that was created using the GUI;
- Phase space redistribution (ISMOOTH) was disabled. When phase space data is used, DOSXYZnrc will re-use the phase space particles if the number of histories required by the user is greater than the number of particles stored in the phase space file. With this option, DOSXYZnrc can redistribute the phase space particles when they are used more than once;
- Phase space file format (MODE) was set to *no ZLAST*, which is the default file format. BEAM can create phase space files with 7 or 8 variables, depending on whether ZLAST is stored or not. DOSXYZnrc has to know that.

3.4.3 Simulation parameters

In order to obtain an uncertainty of less than 1%, the amount of histories (NCASE) to be simulated per square FS were determined using Eq. 29 (section 2.3.4). For example a 1×1 cm^2 FS, the number of voxels is 177 674 ($49\times49\times74$) for 6 MV. 10 000 histories per voxel are required, thus approximately 180 million histories is required. Table 3.22 lists the amount of histories for the square FS apertures.

Table 3.22: Histories performed for square FS apertures.

Square FS (cm^2)	**Number of histories ($\times 10^9$)**
1×1	0.2
2×2	0.4
3×3	0.5
4×4	0.8
5×5	0.9
7×7	1.0
10×10	2.0
12×12	4.0
15×15	6.0
20×20	8.0
30×30	10.0
40×40	20.0

For this same reason, the following number of histories was used for various FS apertures:

- 4×10^9 histories for 5×20 and 20×5 cm^2 rectangular, 10×10 cm^2 off-set and irregular FS apertures
- 6×10^9 histories for 10×30 and 30×10 cm^2 rectangular and 15×15 cm^2 off-set FS apertures
- 8×10^9 histories for 20×20 cm^2 off-set FS apertures.

The number of histories per batch was NCASE/10, as the simulations are divided into 10 batches.

Two random seed numbers (INSEED1 and INSEED2) were set for each simulation. The random number generator (RNG) used requires two seeds between 1 - 31328 and 1 - 30081 respectively. For each different pair of seeds, an independent random number sequence was generated which differed from the default values.

The incident beam size (BEAM_SIZE) was set at 100 cm. This allows the user to control the size of the incident beam for source type 4 phase space input. It is the side of a square field in cm, with a default value of 100 cm. When phase space particles are read from a data file or reconstructed by a multiple-source model, DOSXYZnrc will check their positions and discard those that fall outside of the specified field[27].

For using a homogeneous phantom, HOWFARLESS was turned on. This enabled subroutines HOWFAR and HOWNEAR to ignore voxel boundaries and only considered the extreme outer boundaries of the phantom when calculating distance along particle trajectory or perpendicular distance to the nearest boundary. This allowed charged particles to take longer steps, limiting only SMAX (maximum allowed step length) and ESTEPE (maximum allowed energy loss per step), and thus, speeds up simulation time.

The thickness and medium of the region outside the phantom was set as a uniform vacuum. The output restart data (IDAT) was set to *after every batch*. For large phantoms, writing this file will take a long time.

Range rejection (IREJECT) was set to on. This is a switch for turning on particle range rejection. This can save simulation time by terminating particle histories immediately if they cannot reach the boundary of the current voxel with energy greater than ECUT. The energy associated with that particle is deposited in the current voxel and only the higher electrons can generate bremsstrahlung.

The following parameters for the EGSnrc transport were used[27]:

- Maximum step length (SMAX) was set to 5 cm;
- Maximum fractional energy loss per step (ESTEPE) was set to 0.25 (25%);
- Maximum first elastic scattering moment per step (Xlmax) was set to 0.5;
- Boundary crossing algorithm (bca_algorithm) was set to *PRESTA-I*;
- Skin depth for BCA was set to 0 cm. This is the distance from the boundary at which lateral correlations will be switched off;
- Electron-step algorithm (transport_algorithm) was set to *PRESTA-II*;
- Spin effects for electron elastic scattering was turned on. This is necessary for good backscattering calculations;
- Electron impact ionization (eii_flag) was turned off. This parameter is only of interest in keV X-ray calculations;

- Brems angular sampling (IBRDST) was set to *simple* (default). Only the leading term of the Koch-Motz distribution is used to determine the emission angle of bremsstrahlung photons;
- Brems cross sections was set to BH (default). The Bethe-Heitler bremsstrahlung cross section (Coulomb corrected above 50 MeV) was used;
- Bound Compton scattering (IBCMP) was turned off. Compton scattering was treated with Klein-Nishina;
- Pair angular sampling (IPRDST) was set to *simple*. This turns on the leading term of angular distribution and is sufficient for most applications;
- Photoelectron angular sampling (IPHTER) was turned off (default), meaning that photo-electrons received their directions from the incident photon;
- Rayleigh scattering (IRAYLR) was turned off (default). If switched on, the coherent (Rayleigh) scattering is turned on and requires special PEGS4 data set;
- Atomic relaxations (IEDGFL) was turned off (default). This is only switched on for low energy applications with photo-electric absorption events and the shell vacancies created are relaxed via emission of fluorescent X-rays, Auger and Koster-Cronig electrons; and
- Photon cross-sections (photon_xsections) was set to *Storm-Israel* (default). This determines which photon cross-section data are used and is standard in the PEGS4 data set.

3.4.4 Implementing the beam characterization model

The **dosxyznrc_gui** was used to compile and run the simulations. To compile DOSXYZnrc, the *Compile* button is selected from the *Run* menu. The opened window will provide different **make** options for e.g. optimization, no optimization, debug, etc. In order to run the code from the GUI, an existing input file must be loaded or a new one created. Any changes to an existing file should be saved before running. Selecting the *Run* from the *Run* menu, a window opens giving an option to run

DOSXYZnrc interactively or via queue batch system. Interactive run option was used for all simulations. Now the simulation can begin by selecting the *Execute* button.

3.4.5 DOSXYZnrc output analysis

The resulting output phantom (*.egs4phant*) and dose distribution (*.3ddose*) files for each aperture size and energy were imported into *mcshow*. The *.egs4phant* output file is an ASCII file containing the following information necessary for DOSXYZnrc to simulate the phantom[27]: (1) number of media in the phantom; (2) names of the media; (3) ESTEPE value for each medium; (4) number of voxels in the X, Y and Z directions; (5) list of voxel boundaries in the X, Y and Z directions; (6) an X-Y array containing the medium number in each voxel for each Z slice; and (7) an X-Y array containing the densities in each voxel for each slice in the Z direction. .3*ddose* file contains the 3D dose data generated by DOSXYZnrc[27]. *Mcshow* is a Unix-based dose analysis code that was developed at Fox Chase Cancer Centre by C-M Ma and co-workers[69]. It can read the *.egs4phant* and *.3ddose* files so that the user can extract depth and profile dose data using a plotting tool called Xmgr. Xmgr is an early name for Grace, which is short for **GR**aphing, **A**dvanced **C**omputation and **E**xploration of data[70]. Crossline and inline dose profiles were obtained at d_{max}, 5, 10 and 20 cm depth. PDD curves were obtained for square, rectangular and off-set FS apertures for each energy for which the photon beam source were evaluated.

For irregular FS apertures, crossline and inline dose profiles were also obtained in *mcshow* and compared to the corresponding profiles obtained from the irradiated films. γ-analyses were used on the 2 % / 2 mm comparison level.

Chapter 4 – Results & Discussion

4.1: Film scanner properties

The average red, green and blue pixel values obtained from the film images obtained from scans in scanner #1 (Canon™ CanoScan N670U) are shown in Table 4.1. A ROI of 160×160 pixels was used in ImageJ to acquire the average pixel values against given dose for all the scanned film pieces.

Table 4.1: Average red, green and blue pixel values against given dose from EBT2 film pieces, irradiated in a 6 MV energy photon beam.

Dose	**Average pixel value for 6 MV**		
(cGy)	**Red**	**Green**	**Blue**
0	87.02	68.94	253.88
10	101.73	73.95	253.30
20	114.04	81.90	253.28
40	128.76	89.24	245.79
80	153.32	109.30	244.54
120	169.18	124.99	242.84
160	183.44	136.89	241.13
200	193.37	147.36	239.32
250	204.31	161.04	241.04
300	213.12	172.30	240.49

From Table 4.1 the blue color component's average pixel values stays fairly constant, while the red and green color components' average pixel values increase with increasing absorbed dose. The red component is more sensitive to variation in absorbed dose, thus it will be extracted and used for all film analyses.

4.1.1: Scanner dependency

The same film pieces were scanned on scanner #2 (HP^{TM} Photosmart C4683) on the same day in order to investigate any similarities and/or differences. The compared red channel response curves from both scanners are shown in Fig. 4.1.

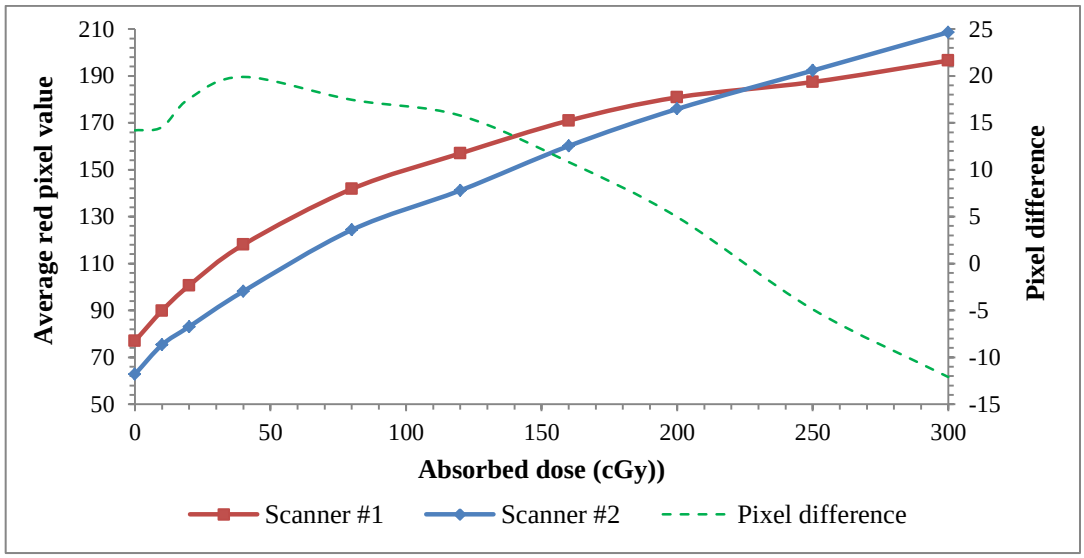

Fig. 4.1: Average pixel response curves from both scanners illustrating scanner dependency. Scanners #1 and #2 are the Canon and HP scanners respectively.

The green dash curve from Fig. 4.1 is the difference in average red pixel values between the two scanners per dose. A maximum average pixel difference of 19.9 can be observed at an absorbed dose value of 40 cGy. It is recommended that only one document scanner be used when calibration and measurement film pieces are scanned for analyses, so that the pixel-to-dose curve for that specific scanner can be used to obtain the measurement film's corresponding absorbed dose value.

4.1.2: Scanner uniformity

The average red pixel values from the 15 equally spaced locations over the scan area were obtained and displayed in Table 4.2. This data were used to determine the uniformity of pixel response from the scanner.

Table 4.2: Average red pixel values from 15 equally spaced locations on scanner surface for uniformity measurements

Positions on A4 scan area	**Average red pixel value**
#1	143.71
#2	142.12
#3	143.49
#4	143.90
#5	141.19
#6	143.93
#7	143.72
#8	140.97
#9	143.70
#10	143.46
#11	141.32
#12	143.70
#13	143.45
#14	141.14
#15	144.07

The maximum and minimum mean red pixel values from Table 4.2 are 144.07 and 140.97 respectively. Using Eq. 35, the pixel uniformity was calculated to be 1.09 %. Thus we can conclude that the scanner has an uniformity of approximately 1 % and it is suitable for film analyses.

4.1.3: Film orientation

The average red pixel values for both portrait and landscape orientations are 140.97 and 146.02 respectively. The percentage difference was calculated to be 3.52 % using Eq. 36, thus illustrating that a large discrepancy can occur when calibration and/or measurement film pieces are scanned in different orientations to one another. It is thus important that the orientation of the film pieces should be the same when scanned for analysis.

4.1.4: Scanning side

The average red pixel values for the film pieces scanned in both face-up and face-down orientation are displayed in Table 4.3.

Table 4.3: Average red pixel values of film pieces scanned in face-up and face-down orientation

Absorbed Dose (cGy)	**Average red component pixel values**		**% error**
	Face-up	**Face-down**	
0	82.45	82.82	**0.45**
10	93.12	93.84	**0.77**
20	105.70	105.58	**0.11**
40	121.32	121.60	**0.23**
80	142.33	142.23	**0.07**
120	158.80	158.80	**0.00**
160	167.34	167.64	**0.18**
200	177.60	179.15	**0.87**
250	188.63	189.27	**0.34**
300	197.67	198.28	**0.31**

The average red pixel values from the film pieces scanned in the face-up and face-down orientations correspond very well with each other, as shown in Table 4.3. The difference percentage was calculated using Eq. 36, with the highest difference of 0.87 % at an absorbed dose of 200 cGy. Thus it can be concluded that irradiated film pieces can be scanned in the face-up or face-down orientation, as there will be a negligible difference between the two orientations.

4.1.5: Scanning repeatability

The average red pixel values for the repeated scans were obtained and shown in Table 4.4.

Table 4.4: Average red pixel values of single film piece scanned multiple times for repeatability

Number of repeated scan	Average red pixel value
#1	142.83
#2	142.81
#3	142.80
#4	142.79
#5	142.87
#6	142.76
#7	142.74
#8	142.81
#9	142.83
#10	142.85

The mean of the ten scanned images' average red pixel values was determined to be 142.81, with a standard deviation of 0.039. The coefficient of variance thus was determined to be 0.04 %. From the results it can be seen that the response of the scanner is constant for repetitive scans and that the scanner is suitable for film analyses. The repeatability is well within 1 %.

4.2: The GUI based MC source model

4.2.1: Square field apertures

4.2.1.1 Initial trial runs

Below are a few examples of parameter trial runs performed in order to compare the simulated MC with the measured WT dose distributions. This was done in order to obtain benchmark parameters for the input files for the MC source generated with the GUI.

A: Maximum incident electron energy (*E0*)

Fig. 4.2 (a) and (b) shows the measured WT and simulated MC PDD's for a 6 MV 1×1 cm^2 square FS aperture with a default value of 6.45 MeV for *E0*, normalized at 10 cm depth and d_{max} respectively. The comparison between the two dose distributions failed, requiring the *E0* value to increase. An *E0* value of 8.17 MeV was then simulated and is displayed in Fig. 4.3 (a) and (b), normalized at 10 cm depth and d_{max} respectively. The comparison also failed.

An *E0* value of 7.00 MeV resulted in the best comparison normalized at 10 cm depth, as shown in Fig. 4.4.

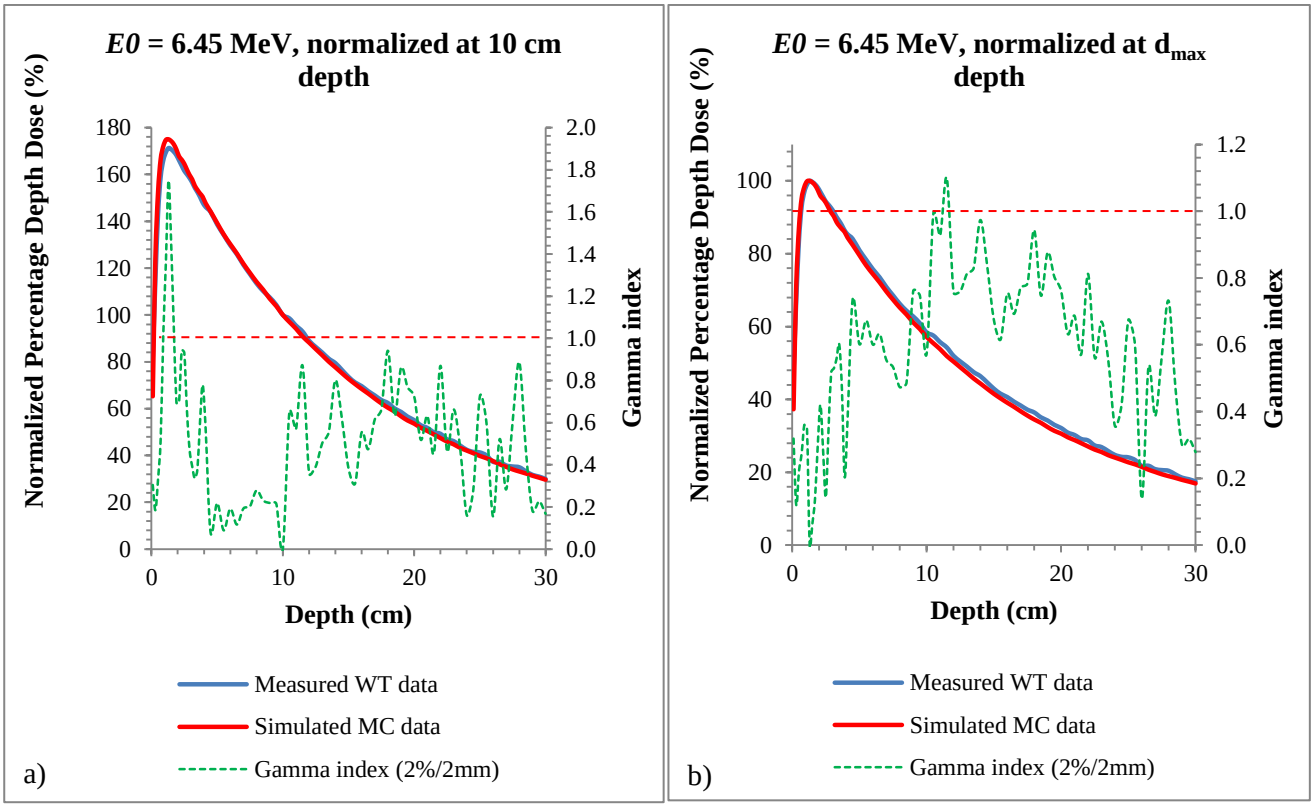

Fig. 4.2: Percentage depth dose (PDD) curve for 6 MV 1×1 cm^2 square field aperture, with a default *E0* value of 6.45 MeV. The green dash curve represents the γ-index evaluation between the measured WT and simulated MC dose distributions, with the comparison failing the evaluation for both which were normalized at (a) 10 cm and (b) d_{max} depth.

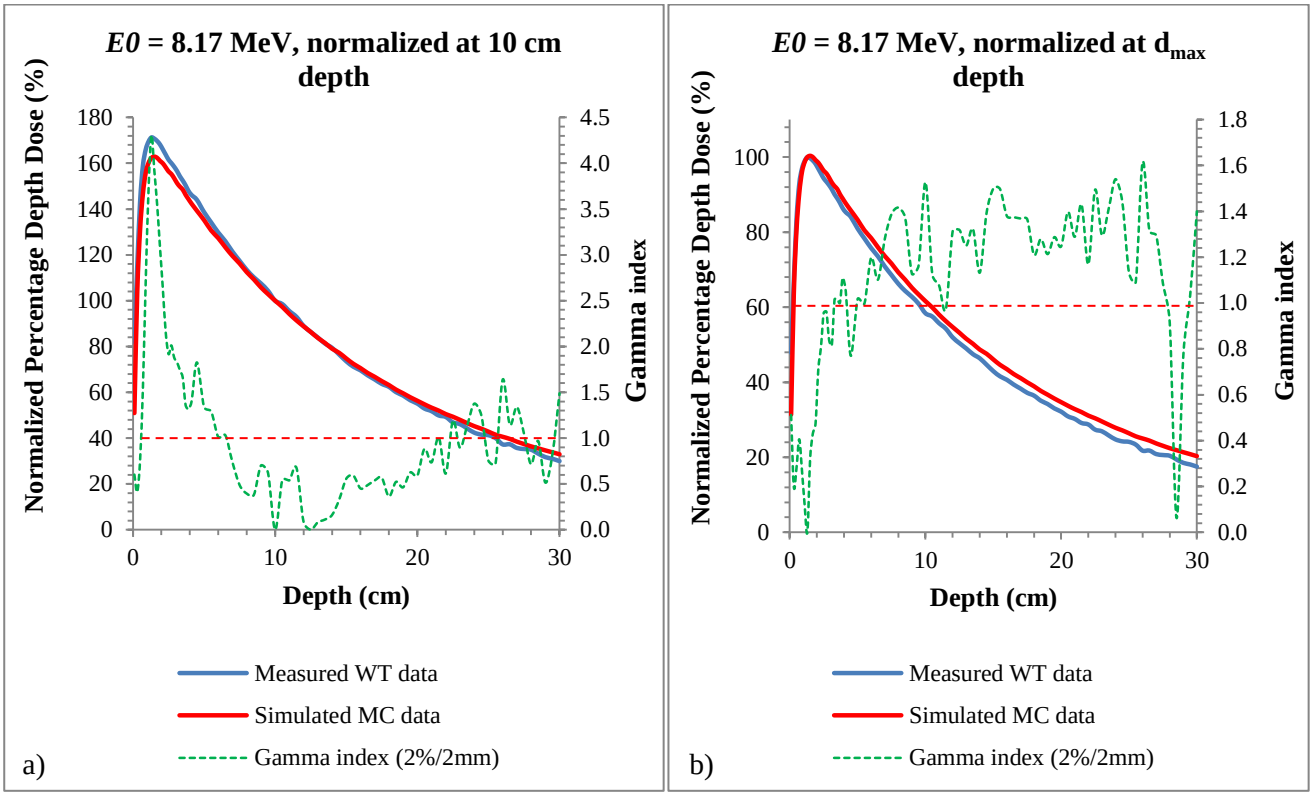

Fig. 4.3: Percentage depth dose (PDD) curve for 6 MV 1×1 cm^2 square field aperture, with an *E0* value of 8.17 MeV. The green dash curve represents the γ-index evaluation between the measured WT and simulated MC dose distributions, with the comparison failing the evaluation for both which were normalized at (a) 10 cm and (b) d_{max} depth.

The penetrative abilities of the 6 MV photons are illustrated by the higher *E0* value. This is necessary for higher energy photons, e.g. 8 and 15 MV beams, to have a higher *E0* value in order to penetrate deeper in the water phantom. For larger square field apertures for a 6 MV beam, higher *E0* values were obtained. This indicates the dose contribution of secondary scatter photons in the measured WT dose distributions. It is thus critical that the best suited value for each square field aperture's *E0* parameter be determined for the best possible fit of the source model. In Fig. 4.2 to 4.4 the γ-index (green dash line) indicated the goodness of fit which is set at 2 % / 2 mm. The maximum incident electron energy onto the target of 7.00 MeV yielded the PDD which resembles the WT data in Fig. 4.4.

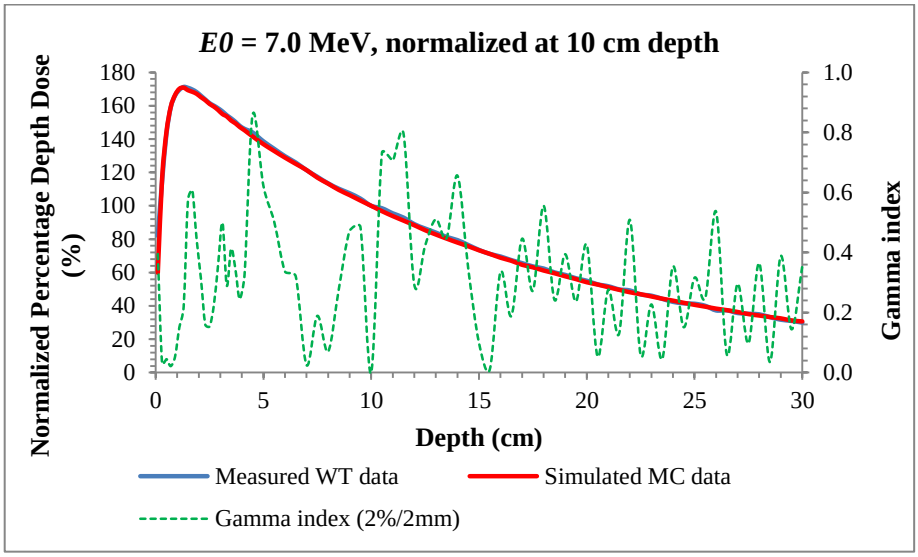

Fig. 4.4: Percentage depth dose (PDD) curve for 6 MV 1×1 cm^2 square field aperture, with an *E0* value of 7.0 MeV. The green dash curve represents the γ-index evaluation between the measured WT and simulated MC dose distributions, with the comparison passed.

B: FWHM of Gaussian function in modeling jaw fluence (*sigma_jaws*)

Fig. 4.5 (a) shows the inline profiles for a 1×1 cm^2 square field aperture for 6 MV beam, at d_{max} depth with *sigma_jaws* default value of 0.4. The comparison between MC and WT dose distributions failed, requiring adjustments in the GUI to adjust the parameter for each jaw separately. Thus, new input source files were created for the X- and Y-jaws to have different values for *sigma_jaws.*

Fig. 4.5 (b) shows the d_{max} depth comparison inline profiles for a 6 MV 1×1 cm^2 aperture with *sigma_jaws_X1* and *sigma_jaws_X2* having a value of 0.042. This value is smaller than the default value of 0.4, thus producing a steeper penumbra for the X-jaws. The evaluation passed using the new parameter value. The transmission of the jaws parameter (*trans_jaws*) was also adjusted in the GUI to be individualized for the X- and Y-jaws, with a smaller value (*trans_jaws_X* = 0.005) in comparison to the default value of 0.072, which was set for both jaws initially.

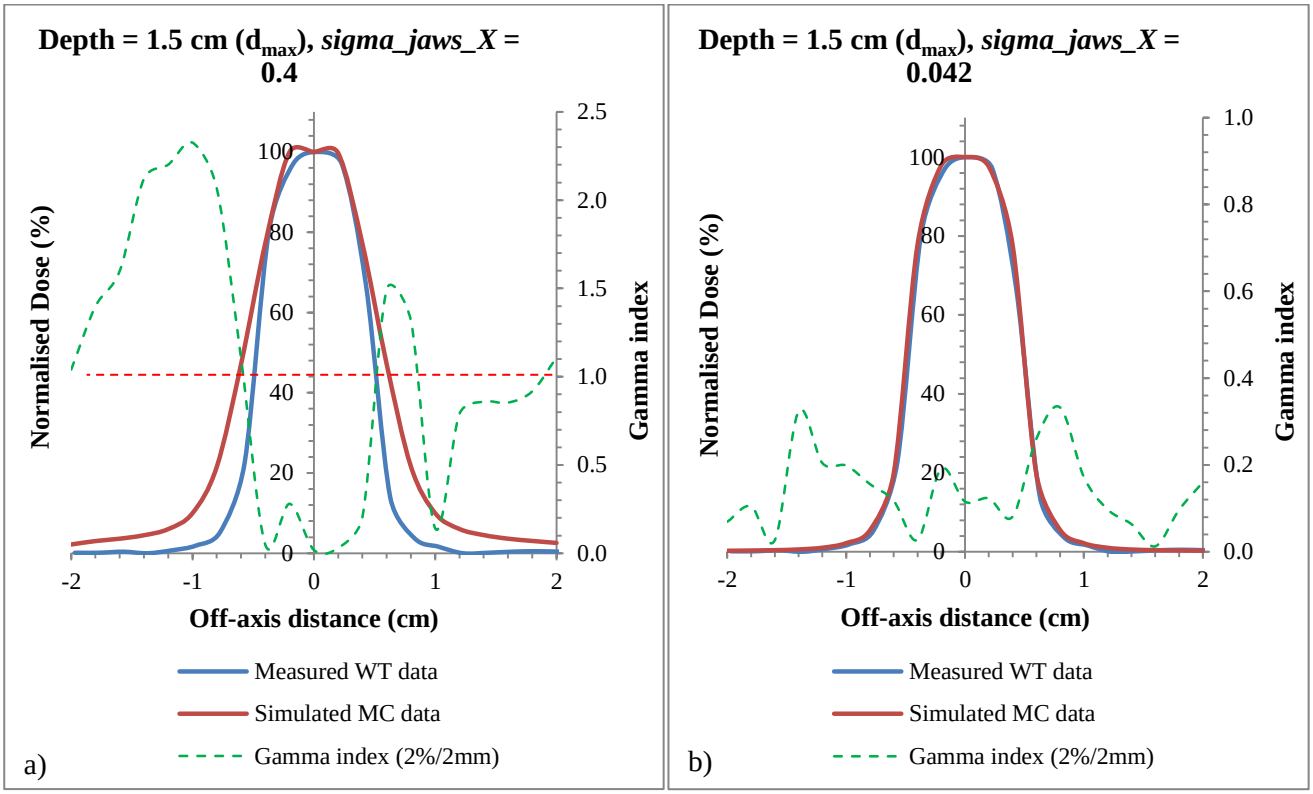

Fig. 4.5: d_{max} depth comparison inline profiles for 6 MV 1×1 cm^2 square field aperture, with a (a) default *sigma_jaws_X* value of 0.4. The green dash curve represents the γ-index evaluation between the measured WT and simulated MC dose distributions, with the comparison failed. (b) displays the d_{max} depth inline profile for 6 MV 1×1 cm^2 square field aperture, with a *sigma_jaws_X* value of 0.042. The γ-index evaluation between the measured WT and simulated MC dose distributions passed.

C: Modelling of transmission of jaw fluence (*trans_jaws*)

The transmission of the jaw parameter (*trans_jaws*) was adjusted in the GUI to be separate for the X- and Y-jaws, as the Y-jaws are thinner than the X-jaws and they are back-up to the MLC's. The Y-jaws transmission values are larger compared to the X-jaws, as the transmission of the MLC's above the Y-jaws also contribute to the net transmission of the fluence. Fig. 4.6 (a) shows the d_{max} depth comparison crossline profiles for a 6 MV 10×10 cm^2 square field aperture with a default *trans_jaws* value of 0.072.

The comparison between the measured WT and simulated MC dose distributions failed just outside the field, as indicated by the red dash ellipses. Thus it was necessary to adjust the transmission to a higher value to align MC and WT data, as shown in Fig. 4.6 (b). Fig 4.6 (b) shows the d_{max} depth comparison crossline profiles for a 6 MV 10×10 cm^2 square field aperture with a default *trans_jaws* value of 0.282, with the comparison passed.

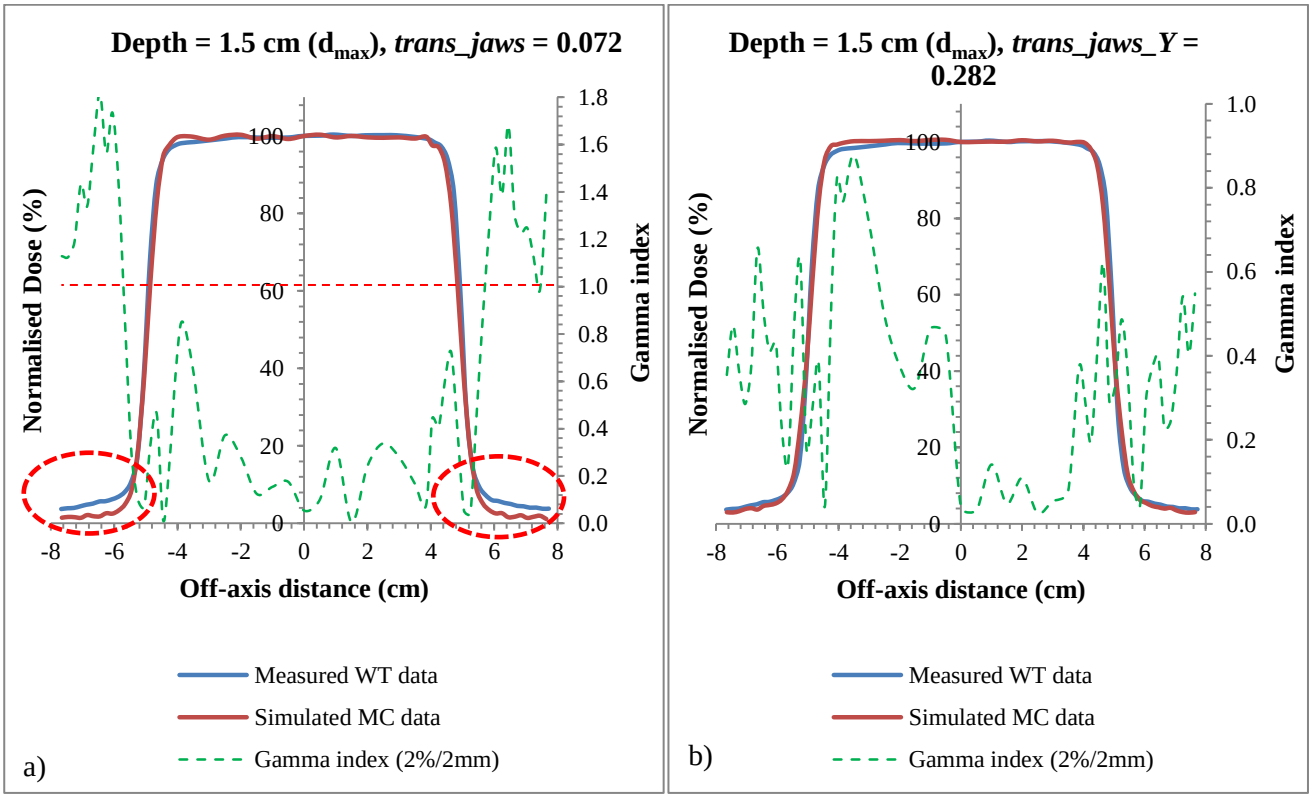

Fig. 4.6: d_{max} depth comparison crossline profiles for 6 MV 10×10 cm^2 square field aperture, with a (a) default *trans_jaws* value of 0.072. The green dash curve represents the γ-index evaluation between the measured WT and simulated MC dose distributions, with the comparison failed as indicated by the red dash ellipses. (b) displays the d_{max} depth crossline profile for 6 MV 10×10 cm^2 square field aperture, with a *trans_jaws_Y* parameter value of 0.282. The γ-index evaluation between the measured WT and simulated MC dose distributions passed.

D: FWHM of Gaussian function in target fluence (*psig4*)

Fig. 4.7 shows the crossline profiles for a 30×30 cm^2 square field aperture for 6 MV beam, at d_{max} depth. The comparison between MC and WT dose distributions failed, requiring adjustments in the target fluence due to the "horns" on the profile (indicated by the blue arrows). The *psig4* parameter is related to a specific energy, thus it is ideal for its value to be constant for that specific energy.

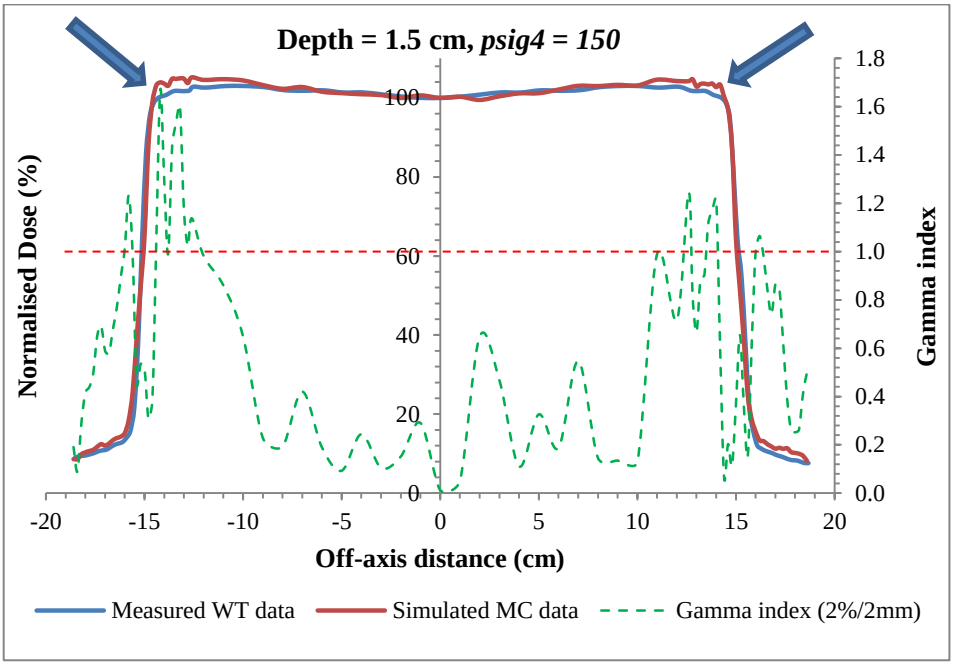

Fig. 4.7: Crossline profiles taken at d_{max} for 6 MV for a 30×30 cm^2 square field aperture, with a default *psig4* value of 150. The green dash curve represents the γ-index evaluation between the measured WT and simulated MC dose distributions, with the comparison failed at the 'horns' of the profiles.

In order to find the optimum *psig4* parameter value, a least square (LS) optimization method[71] was used. The method used the profile data in 80% open FS area of the crossline and inline profiles from the 40×40 cm^2 square aperture for the 6 MV beam taken at a depth beyond the range of contamination electrons, as displayed in Fig. 4.8. From Fig. 4.8, the minimum LS value represents the smallest difference between the measure WT and simulated MC dose distributions, thus the optimum *psig4* parameter value. The minimum LS for both the crossline and inline profiles for the 6 MV beam gave

an optimum *psig4* parameter value of 62. The same process was performed for the 8 and 15 MV beams, and their respective *psig4* parameter values were found to be 118 and 240 respectively.

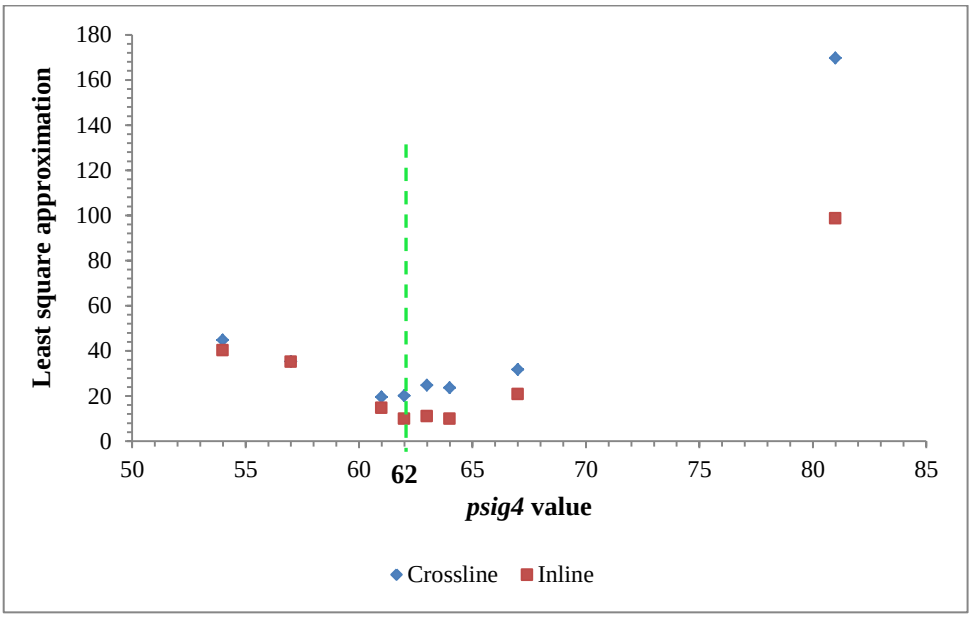

Fig. 4.8: Least square values of the 80% open field size area of the crossline and inline profiles for the 6 MV 40×40 cm^2 square aperture, in order to find the optimum *psig4* parameter value. The green dash line illustrates the corresponding *psig4* parameter value of 62 for the minimum LS optimization between the measured WT and simulated MC dose distributions.

4.2.1.2 Electron contamination model

Fig. 4.9 (a) shows a PDD comparison between measured WT and simulated MC dose distributions for a 6 MV 15×15 cm^2 square aperture. The comparison failed the γ-index evaluation in the build-up and d_{max} regions. This meant that electron contamination was needed in order to increase the absorbed dose near the surface of the water. Initially, the GUI could provide an input source file that contained two sub-sources, one each for photons and electrons, to give a total fluence weight of 100%. We then incorporated the electron contamination model from the 15 MV to the source codes of the 6 and 8 MV beams as well. Fig. 4.9 (b) displays the PDD comparison between measured WT and simulated MC dose distributions for a 6 MV 15×15 cm^2 square aperture after 0.1% electron weight was added to the

6 MV source code. 99.9% of the fluence exists out of photons. The comparison passed the γ-index evaluation.

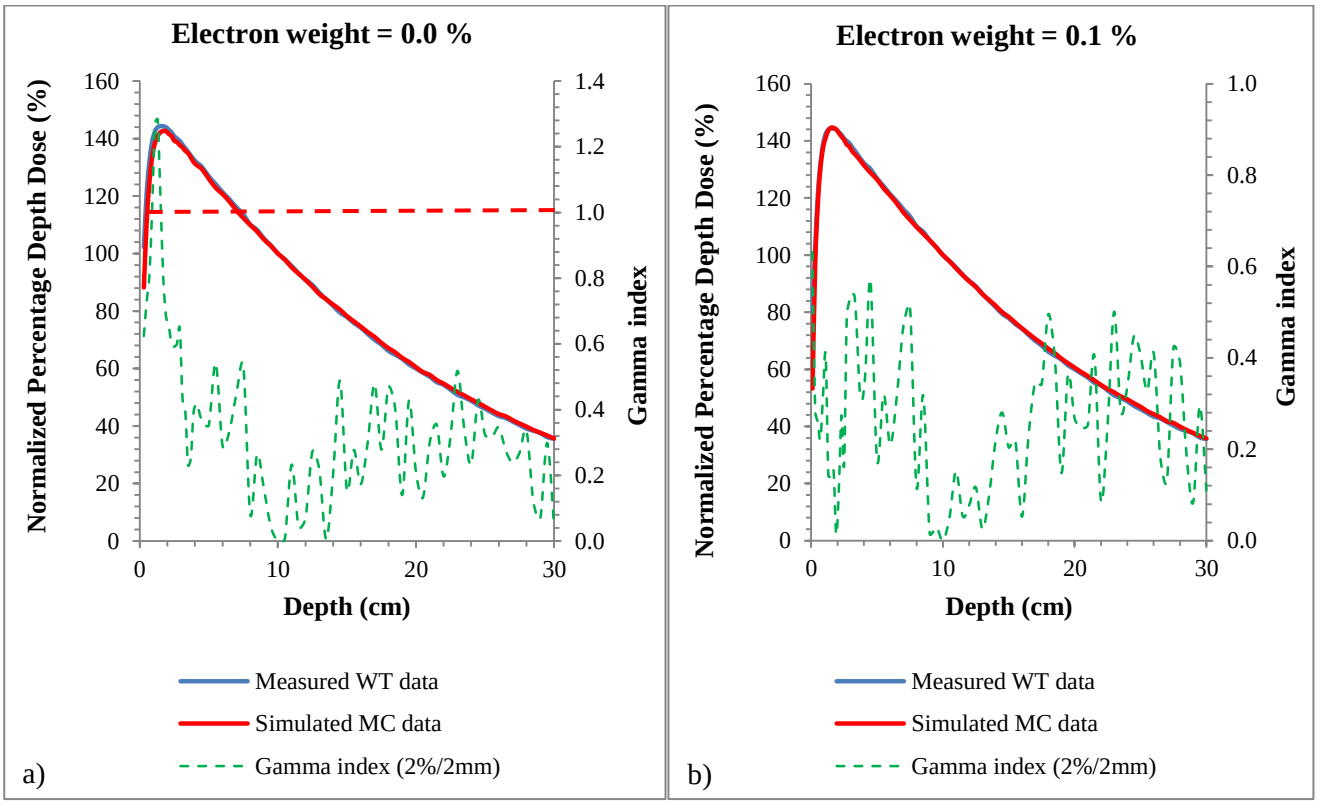

Fig. 4.9: Percentage depth dose (PDD) curve for 6 MV 15×15 cm^2 square field aperture (a) without any contamination electrons. The green dash curve represents the γ-index evaluation between the measured WT and simulated MC dose distributions. The comparison failed in the dose build-up region. The red dash line indicates the pass/fail border of the γ-index = 1. (b) shows the PDD curve for 6 MV 15×15 cm^2 square field aperture with 0.1 % electron weight added to the source code. The γ-index evaluation between the measured WT and simulated MC dose distributions passed.

The larger square field apertures required higher electron weights. This is due to the fact that the source model struggles to model the electrons which are present in the measured WT dose distributions, as more electrons fall onto the water surface in larger field apertures and contribute to the surface dose. The electron weights for the various FS and energies are listed in Table 4.6 in the next section.

4.2.1.3 Summary of parameters

The parameter values for the various square field apertures and energies obtained are displayed in the tables and figures below. These parameter values were subsequently used as benchmark values for the rectangular, off-set and irregular field apertures simulations and comparisons.

The maximum electron energy (*E0*) parameter values for all energies are listed in Table 4.5.

Table 4.5: Parameter *E0* values for all energies

Photon energy beam (MV)	**Maximum incident electron energy, *E0* (MeV)**
6	7.00
8	8.73
15	13.24

The relative intensity for the electron contamination model for all energies and various square field apertures are listed in Table 4.6 below. As previously discussed in the section before, the larger square field apertures requires larger electron source intensities due to the fact that the source model struggles to add dose in the build-up region.

Table 4.6: Electron source intensity weights for various square field apertures for all energies

Square FS (cm^2)	**Electron source intensity weight (%)**		
	6 MV	**8 MV**	**15 MV**
1×1	0.00	0.00	0.00
2×2	0.00	0.00	0.00
3×3	0.00	0.00	0.00
4×4	0.00	0.00	0.05
5×5	0.00	0.00	0.05
7×7	0.00	0.00	0.10
10×10	0.00	0.10	0.20
12×12	0.00	0.10	0.30
15×15	0.10	0.20	0.40
20×20	0.20	0.30	0.80
30×30	0.50	0.50	1.00
40×40	0.60	0.70	1.00

The FWHM of the Gaussian, which is the derivative of the error function, that describes the penumbra of the X- and Y-jaw fluence (*sigma_jaws_X* and *sigma_jaws_Y*) parameters, along with the X- and Y-jaw fluence maximum transmission (*trans_jaws_X* and *trans_jaws_Y*) parameter values for the various square field size apertures, are listed in Table 4.7. The *sigma_jaws* and *trans_jaws* parameters are the same for all the energies.

The FWHM of the Gaussian error function (*sigmax_mlc* and *sigmay_mlc*) parameter values for the MLC's penumbra model of the fluence in the X- and Y-directions are 0.4 for all energies.

Table 4.7: Jaw fluence parameters for various square field size apertures. These values were used for all three beam energies studied.

Square FS (cm^2)	***sigma_jaws***		***trans_jaws***	
	X	***Y***	***X***	***Y***
1×1	0.042	0.197	0.005	0.035
2×2			0.005	0.071
3×3			0.005	0.071
4×4			0.008	0.141
5×5	0.155	0.352	0.023	0.176
7×7			0.039	0.211
10×10			0.062	0.282
12×12			0.070	0.352
15×15			0.087	0.423
20×20			0.107	0.528
30×30			0.127	0.599
40×40			0.085	0.528

4.2.1.4 Square FS apertures: WT vs MC data

A few square FS apertures are displayed, for example, in this section in order to illustrate the comparison between the measured WT and simulated MC dose distributions. This was done in order to benchmark the source model. For the comparison PDD profiles in Fig. 4.11 – 4.17, the measured WT dose data are displayed by solid lines, with the square, diamond and triangle symbols representing the simulated MC dose data for 6, 8 and 15 MV respectively. Crossline and inline profiles for the WT dose measurements and MC simulations for are shown in Fig. 4.11 – 4.17. Various depth profiles are displayed and are normalized to the PDD value at that depth respectively. The solid lines represent the measured WT dose data, with the square symbols the simulated MC dose data for the crossline profiles. The dash lines represent the measured WT dose data, and the triangles the simulated MC dose data for the inline profiles. The γ-index for all the comparisons passed the 2 % / 2 mm criteria, with the MC variance below 1.0 % for all the simulations.

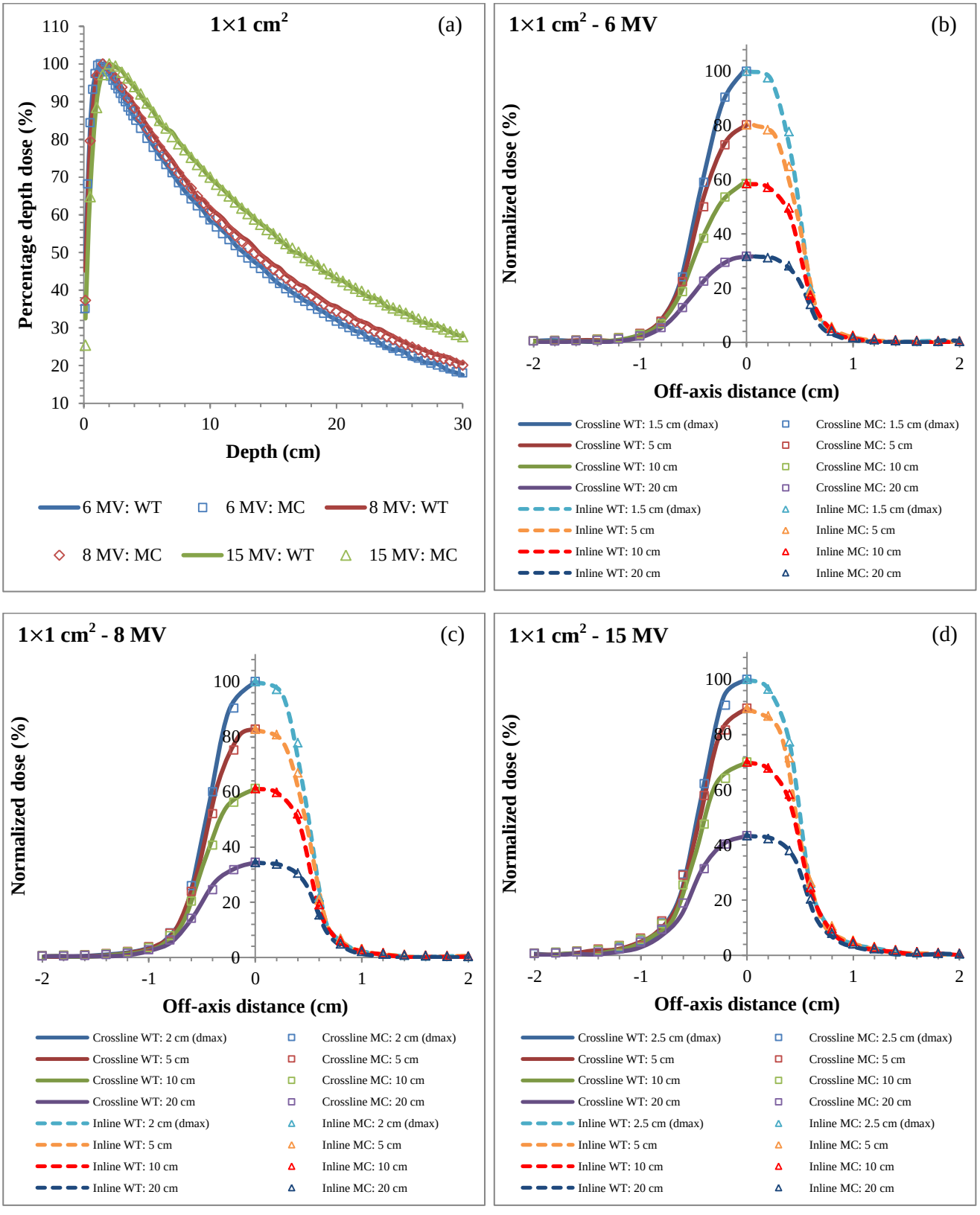

Fig. 4.11: Comparison dose data for a 1×1 cm^2 square FS aperture (a) PDD curves for various energies and (b – d) crossline and inline profiles for the 6, 8 and 15 MV beams respectively.

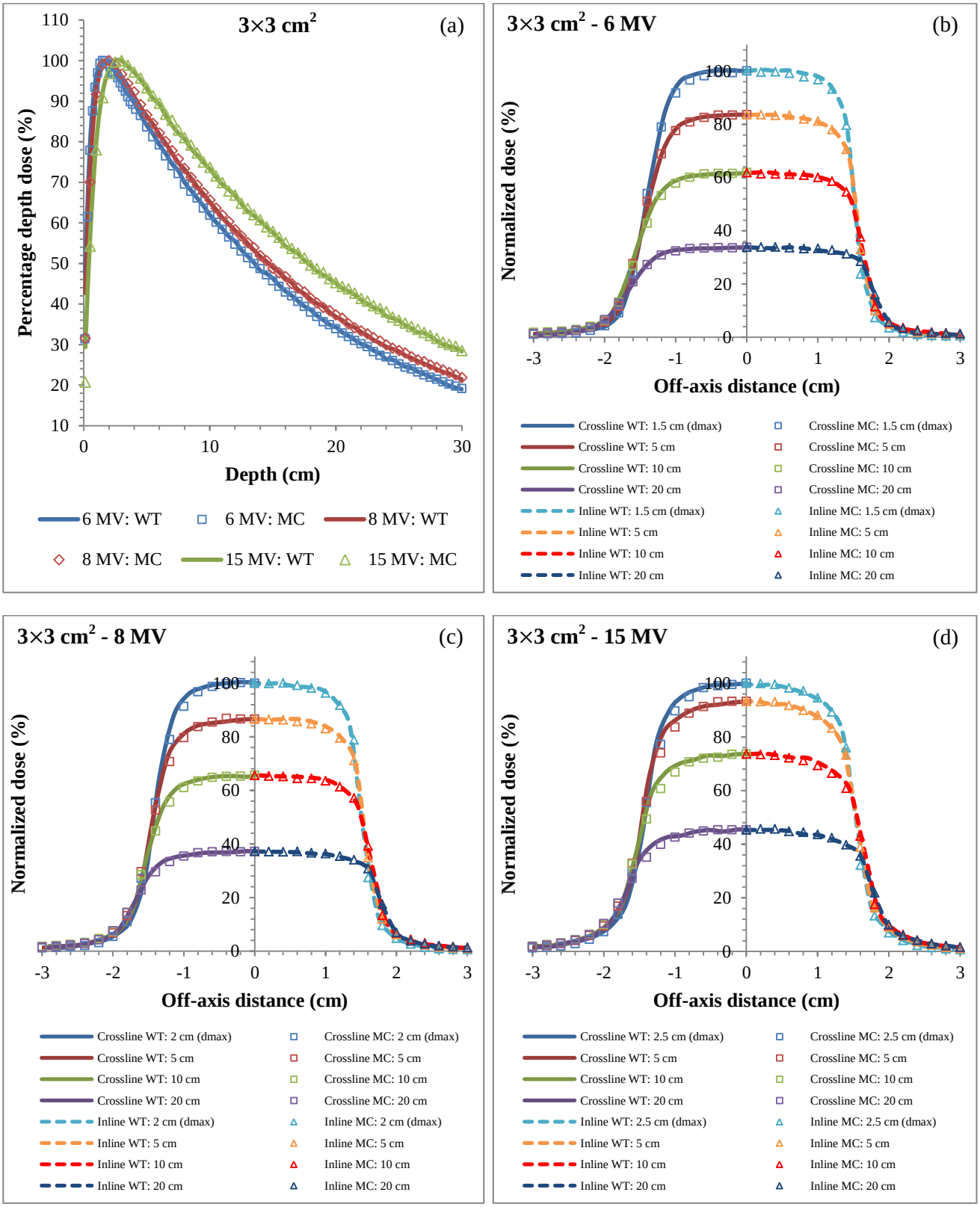

Fig. 4.12: Comparison dose data for a 3×3 cm^2 square FS aperture (a) PDD curves for various energies and (b – d) crossline and inline profiles for the 6, 8 and 15 MV beams respectively.

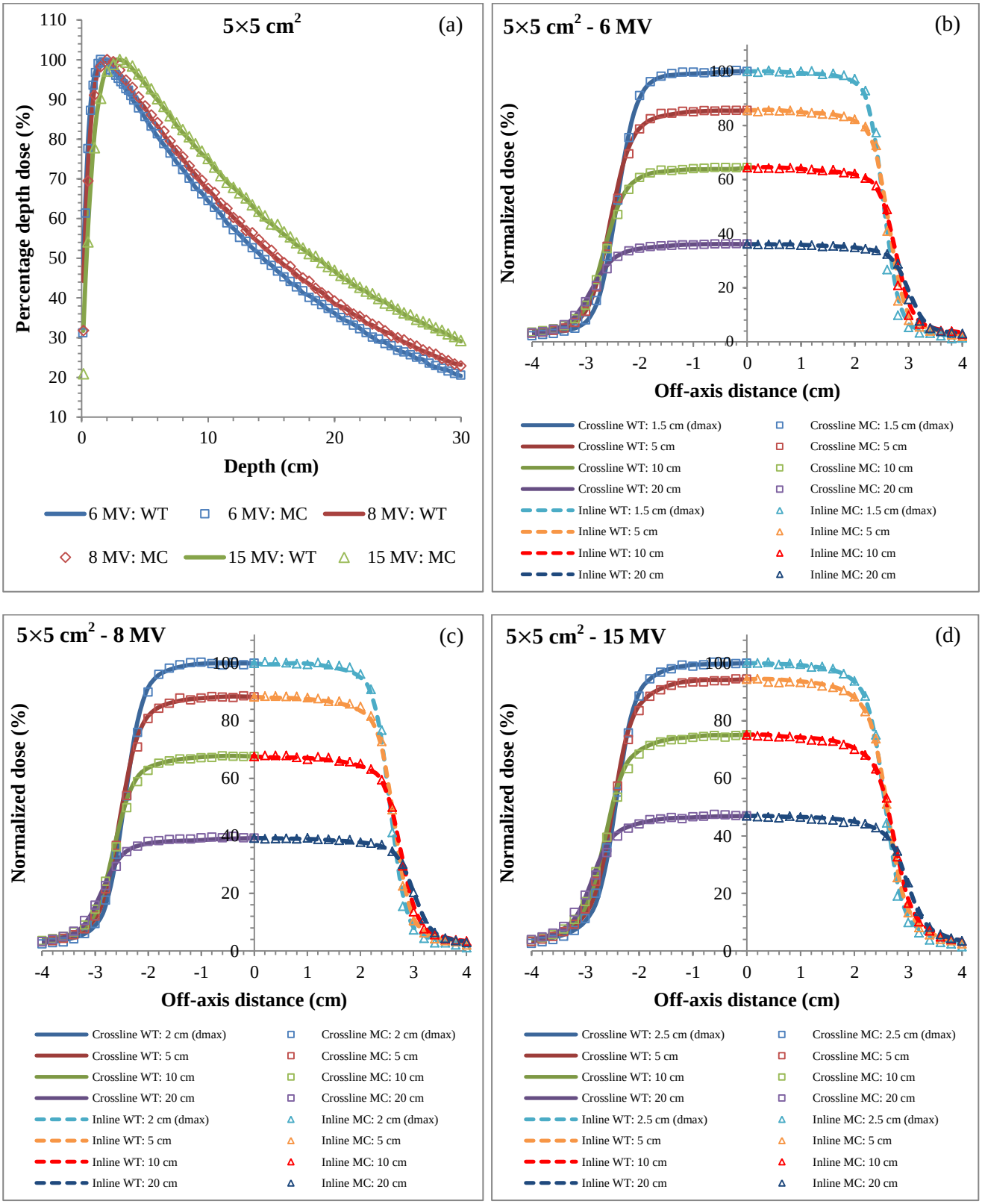

Fig. 4.13: Comparison dose data for a 5×5 cm^2 square FS aperture (a) PDD curves for various energies and (b – d) crossline and inline profiles for the 6, 8 and 15 MV beams respectively.

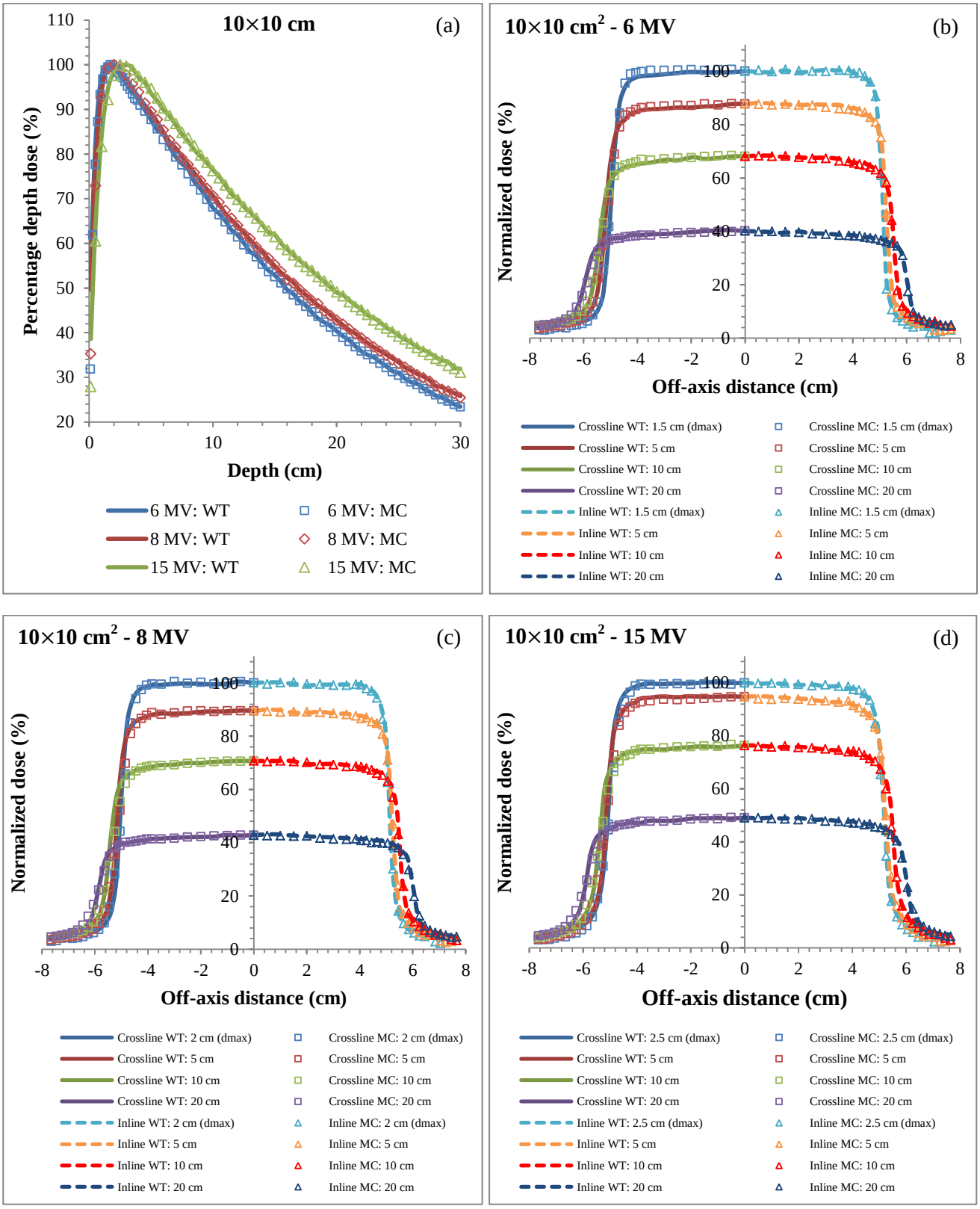

Fig. 4.14: Comparison dose data for a 10×10 cm^2 square FS aperture (a) PDD curves for various energies and (b – d) crossline and inline profiles for the 6, 8 and 15 MV beams respectively.

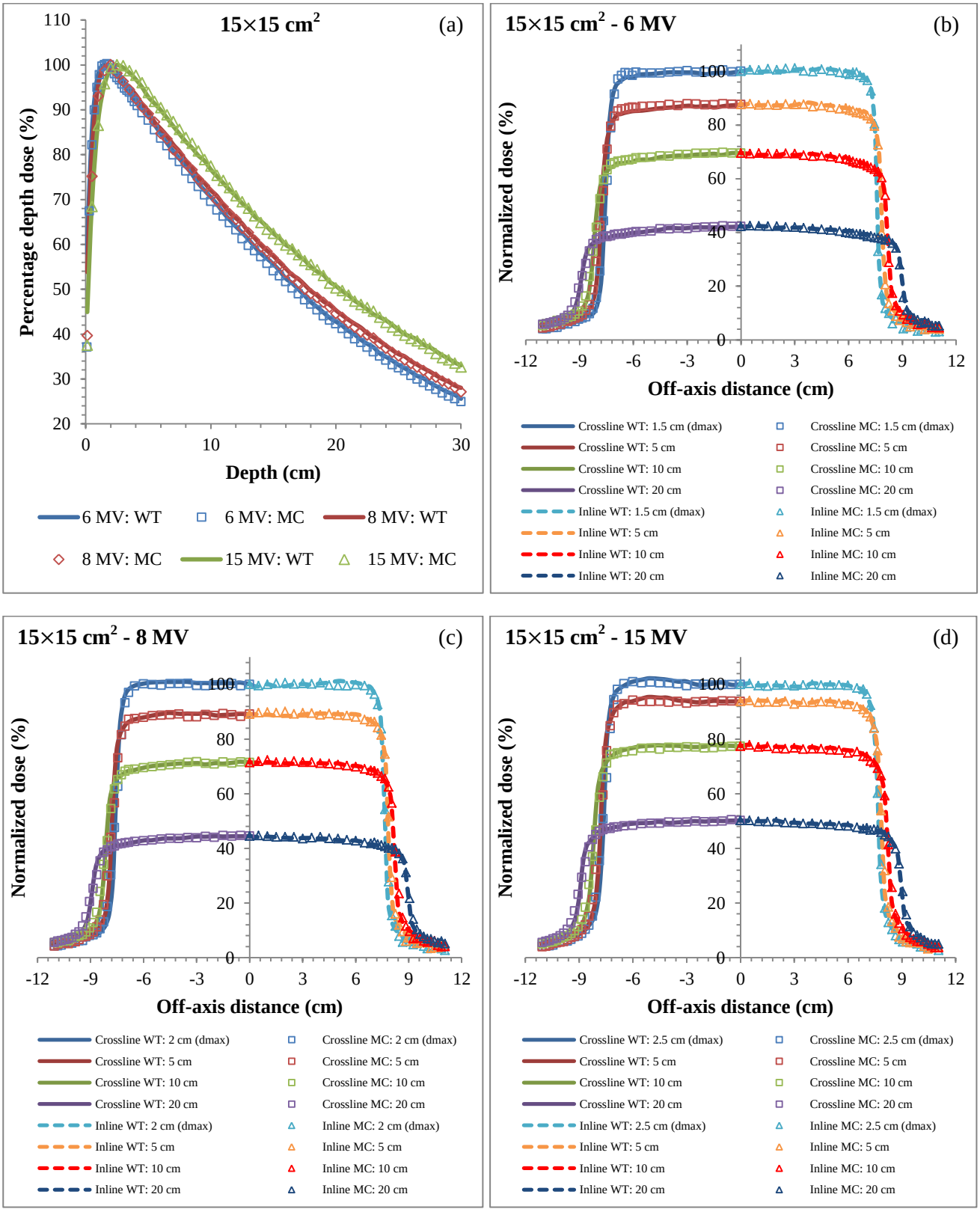

Fig. 4.15: Comparison dose data for a 15×15 cm^2 square FS aperture (a) PDD curves for various energies and (b – d) crossline and inline profiles for the 6, 8 and 15 MV beams respectively.

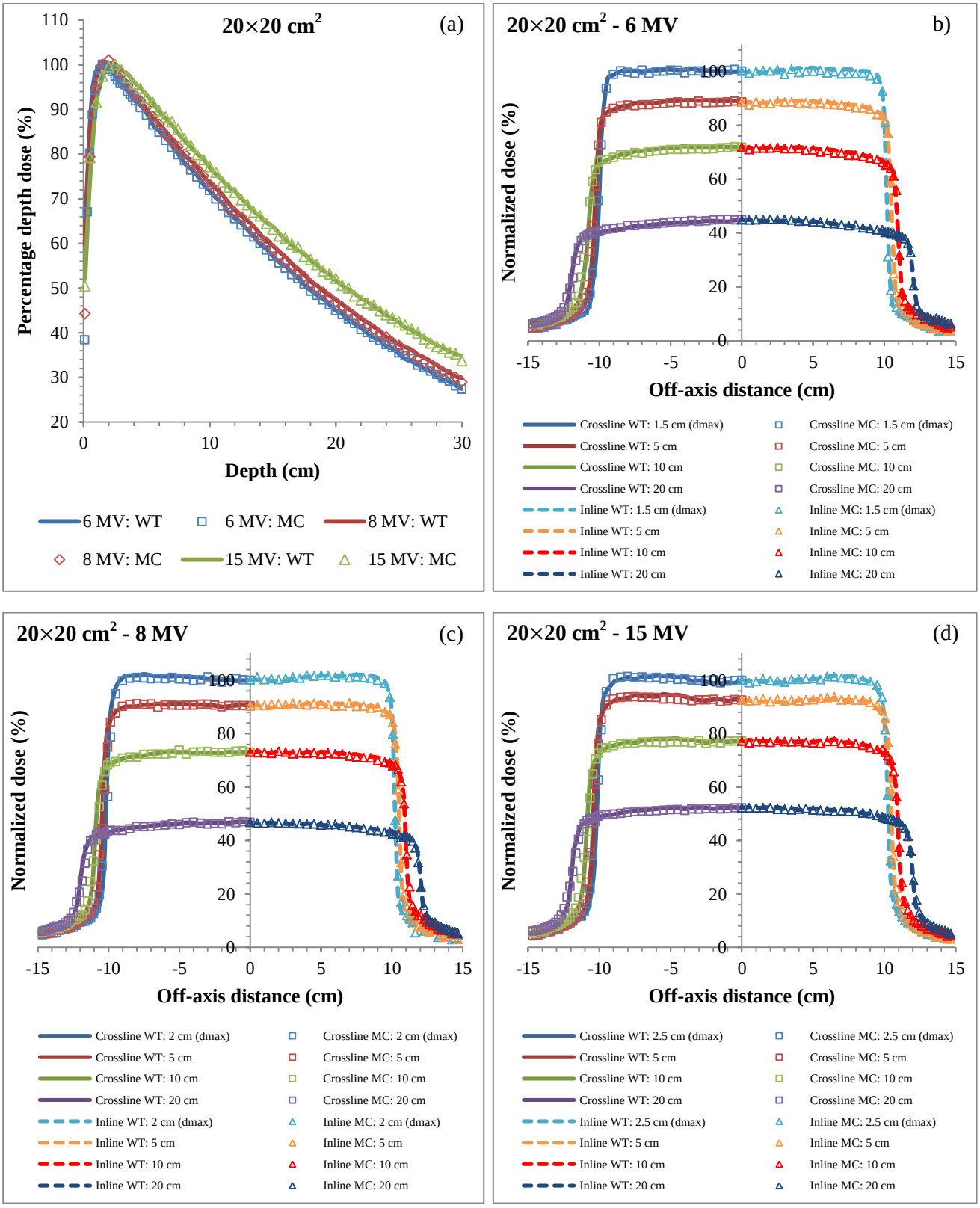

Fig. 4.16: Comparison dose data for a 20×20 cm^2 square FS aperture (a) PDD curves for various energies and (b – d) crossline and inline profiles for the 6, 8 and 15 MV beams respectively.

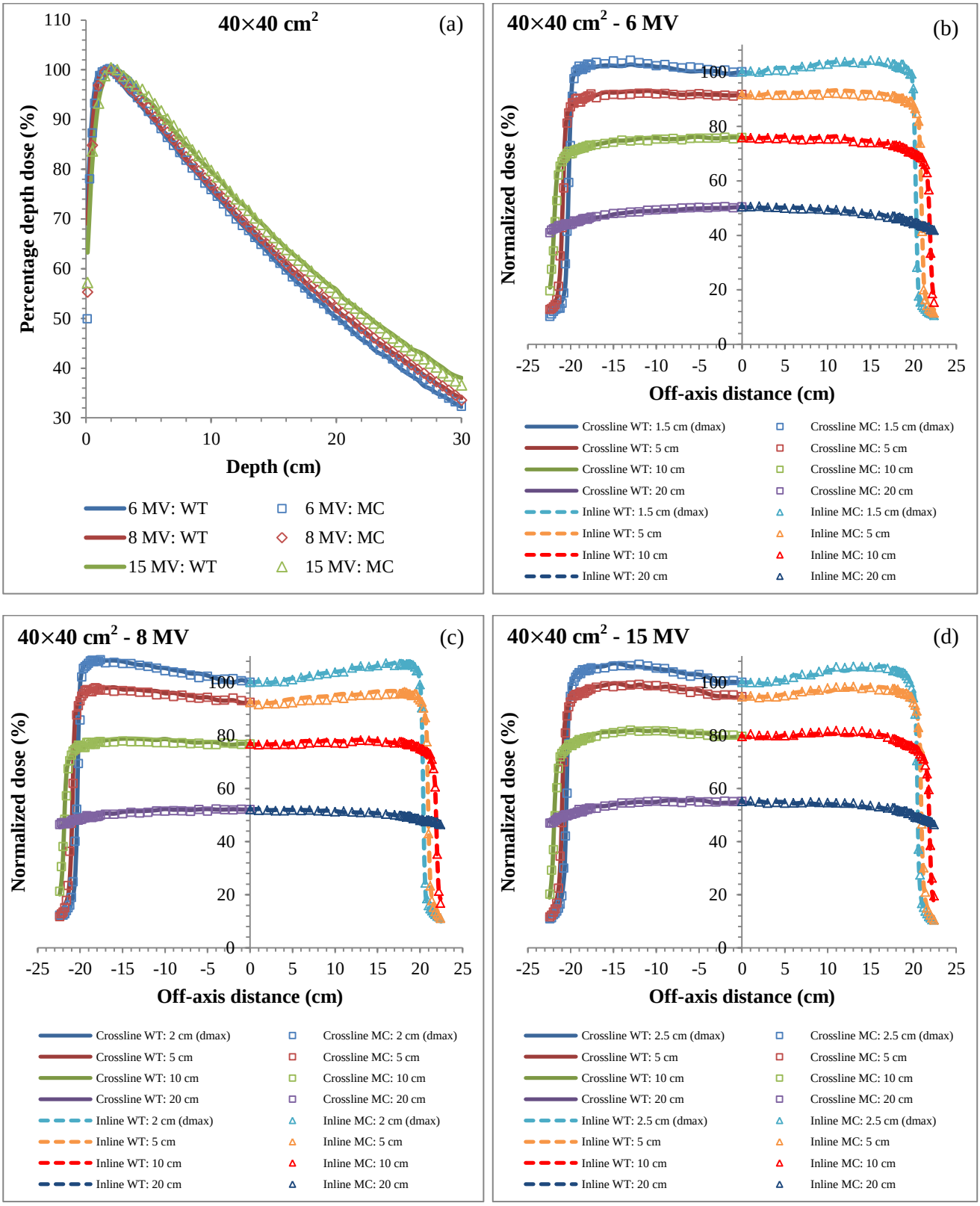

Fig. 4.17: Comparison dose data for a 40×40 cm^2 square FS aperture (a) PDD curves for various energies and (b – d) crossline and inline profiles for the 6, 8 and 15 MV beams respectively.

4.2.2: Rectangular field apertures

Using the benchmarked source model parameters from the square FS apertures, e.g. data in Tables 4.5 – 4.7, the following rectangular FS apertures were simulated and evaluated against measured data: 5×20, 20×5, 10×30 and 30×10 cm^2. Percentage depth dose data, as well as, crossline and inline profiles for all energies are displayed in Figs. 4.19, 4.21, 4.23 and 4.25 respectively.

In these figures the measured WT dose data are displayed by solid lines, with the square, diamond and triangle symbols the simulated MC dose data for 6, 8 and 15 MV respectively. For the comparison crossline and inline profiles between the WT dose measurements and MC simulations for 6, 8 and 15 MV, the various depth profiles displayed are normalized to the local PDD for each energy under consideration. The solid lines represent the measured WT dose data, with the square symbols the simulated MC dose data for the crossline profiles. The dash lines represent the measured WT dose data, and the triangle symbols the simulated MC dose data for the inline profiles. The γ-index criterion of 2 % / 2 mm was met for all comparisons, with the MC variance below 1.0 %. This illustrates that the source model parameters is suitable for symmetrical geometries.

4.2.2.1 Aperture size: 5×20 cm^2

Fig. 4.18 (a) displays the coronal slice at isocenter of the dose distribution in the water phantom for 6 MV beam in *mcshow*. Fig. 4.18 (b) displays the transverse slice at d_{max} = 1.5 cm depth for 6 MV. The red dash lines indicate the locations where the depth and profiles curve data were extracted along the CAX.

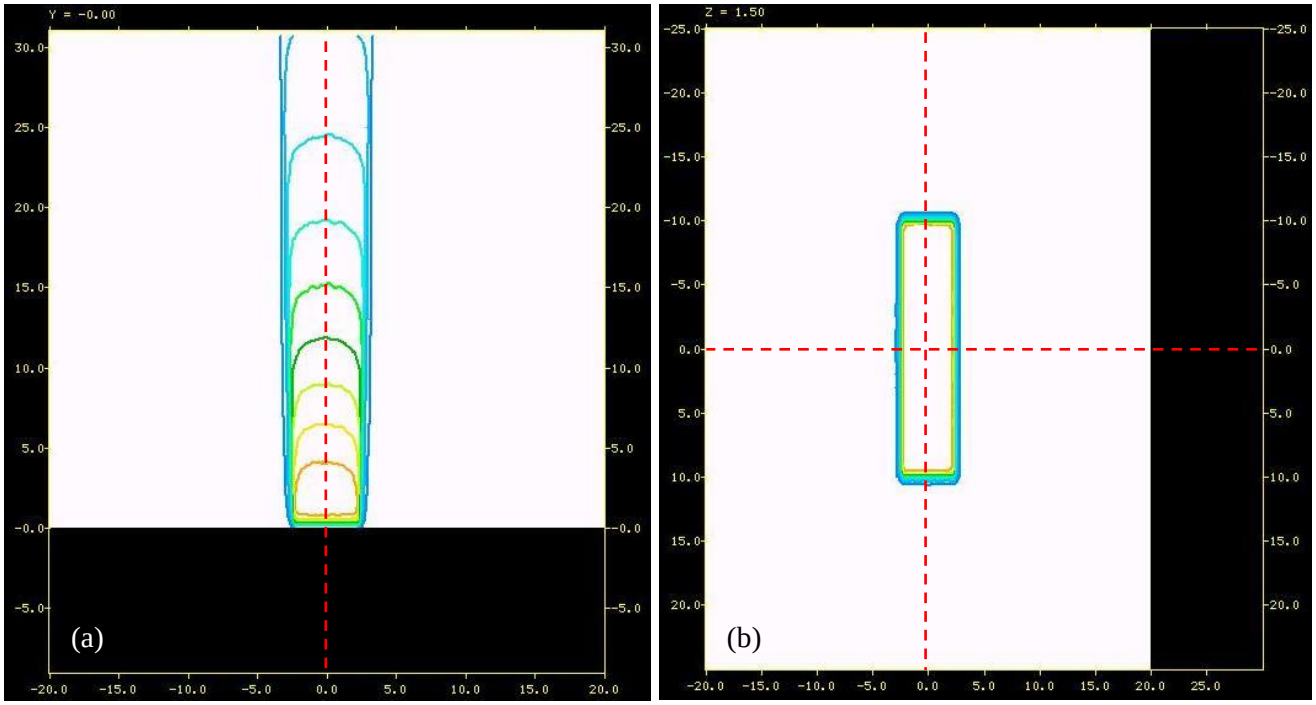

Fig. 4.18: (a) Coronal and (b) transverse slices displaying dose distributions for the 5×20 cm^2 FS for a 6 MV beam in *mcshow*. Dose data were extracted along the red dash lines for PDD and dose profile comparison as shown in the next figure.

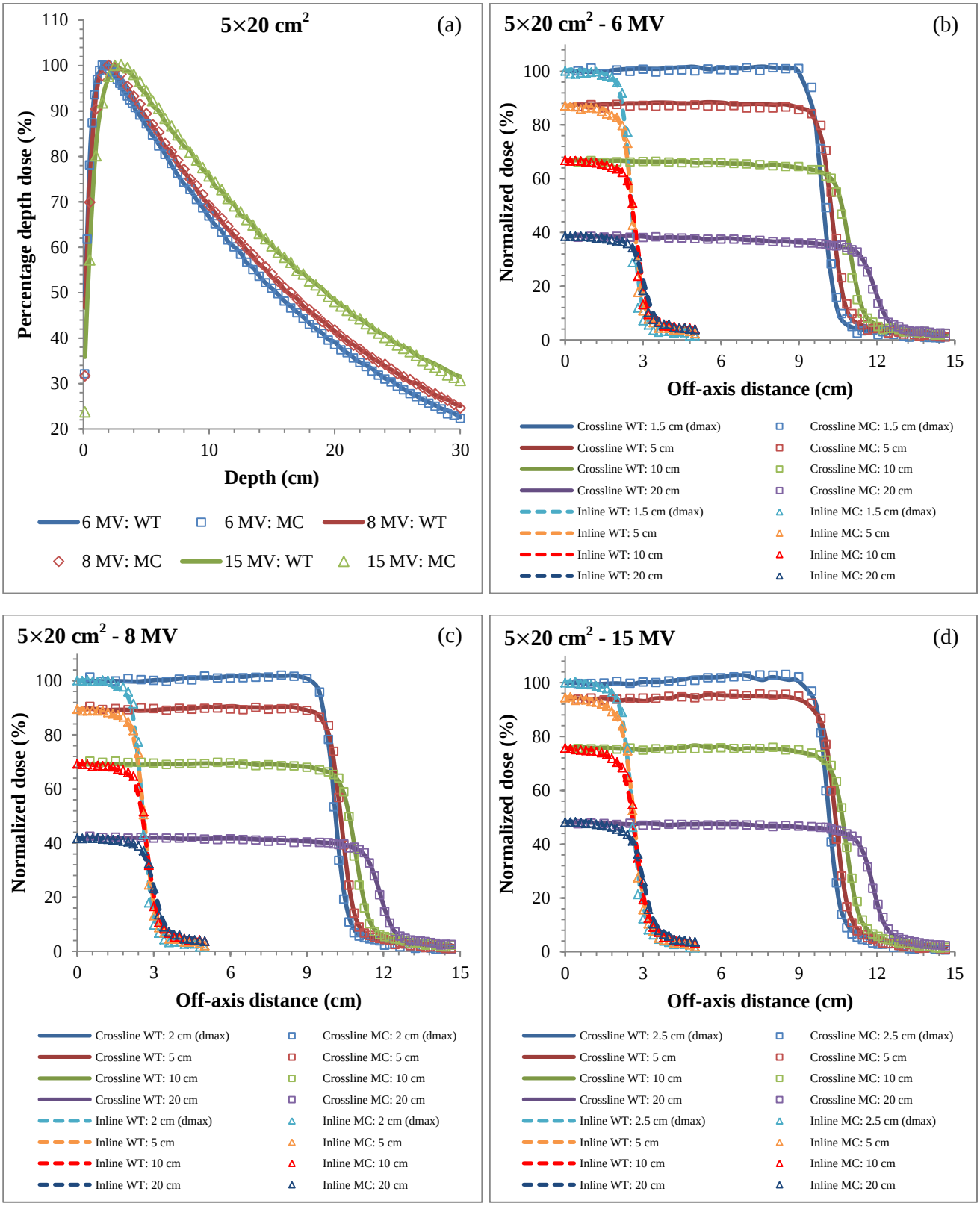

Fig. 4.19: Comparison dose data for a 5×20 cm^2 rectangular FS aperture (a) PDD curves for various energies and (b – d) crossline and inline profiles for the 6, 8 and 15 MV beams respectively.

4.2.2.2 Aperture size: 20×5 cm^2

Fig. 4.20 (a) displays the coronal slice at isocenter of the dose distribution in the water phantom for the 6 MV beam in *mcshow*. Fig. 4.20 (b) displays the transverse slice at d_{max} = 1.5 cm depth. The red dash lines indicate the dose extraction points in the water phantom.

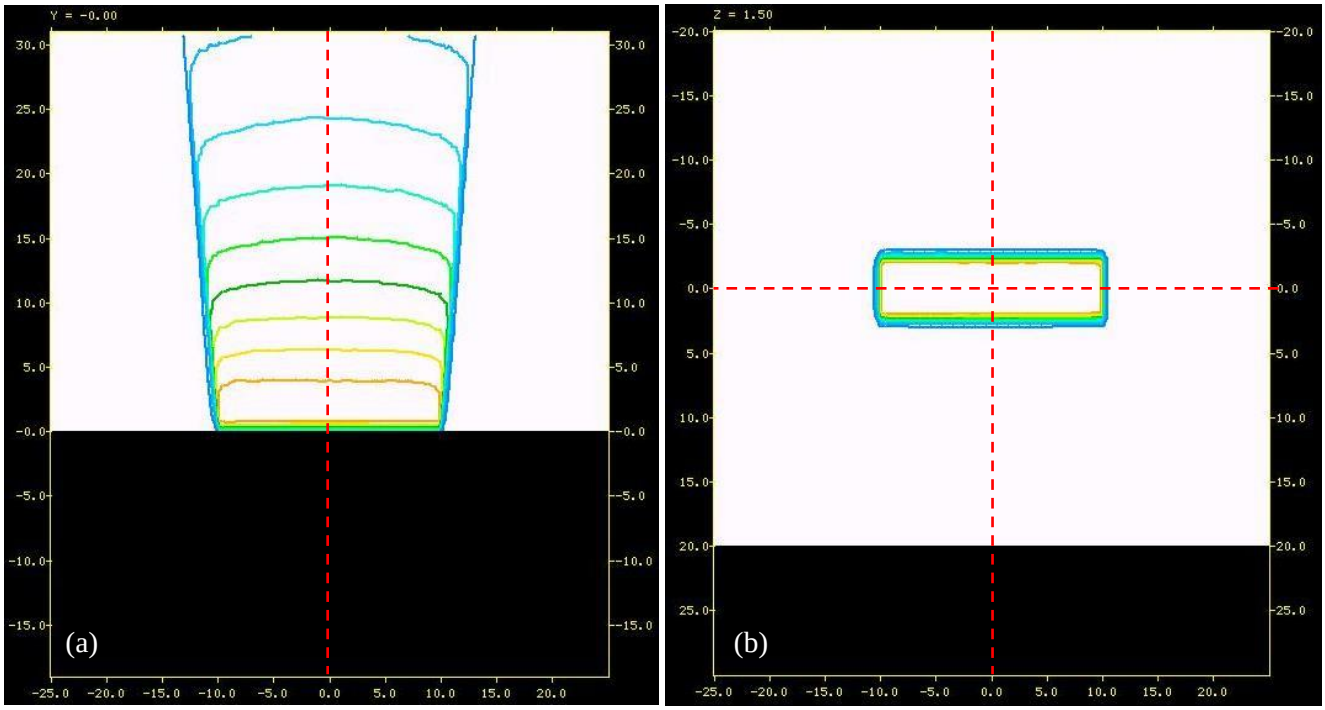

Fig. 4.20: (a) Coronal and (b) transverse slices displaying dose distributions for the 20×5 cm^2 FS for 6 MV beam in *mcshow*. The red dash lines display the dose extraction points for PDD and dose profile data comparison as shown in the next figure.

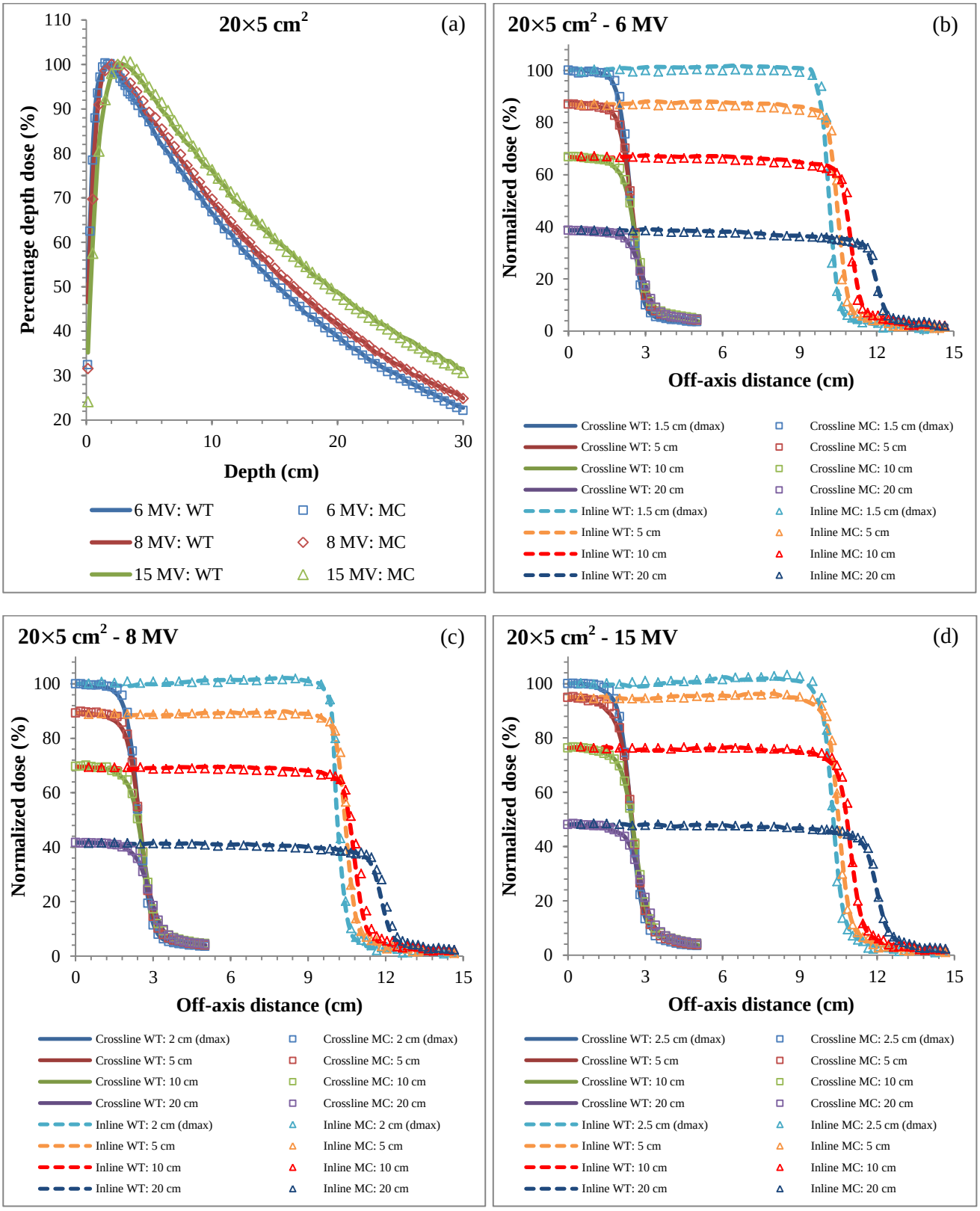

Fig. 4.21: Comparison dose data for a 20×5 cm^2 rectangular FS aperture (a) PDD curves for various energies and (b – d) crossline and inline profiles for the 6, 8 and 15 MV beams respectively.

4.2.2.3 Aperture size: 10×30 cm^2

Fig. 4.22 (a) displays similar data compared to Fig. 4.20 for the 10×30 cm^2 FS.

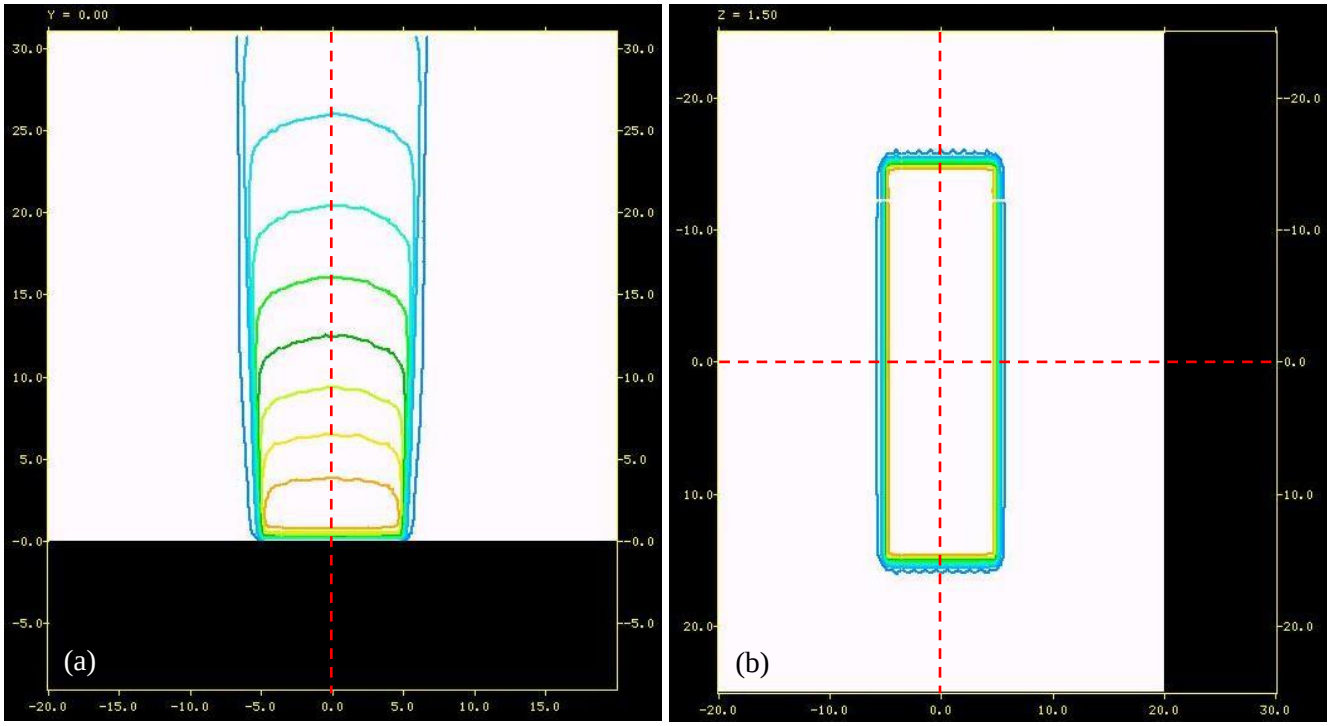

Fig. 4.22: (a) Coronal and (b) transverse slices displaying dose distributions for the 10×30 cm^2 FS for 6 MV beam in *mcshow*. PDD and dose profile data were extracted along the red dash lines and is shown in the next figure.

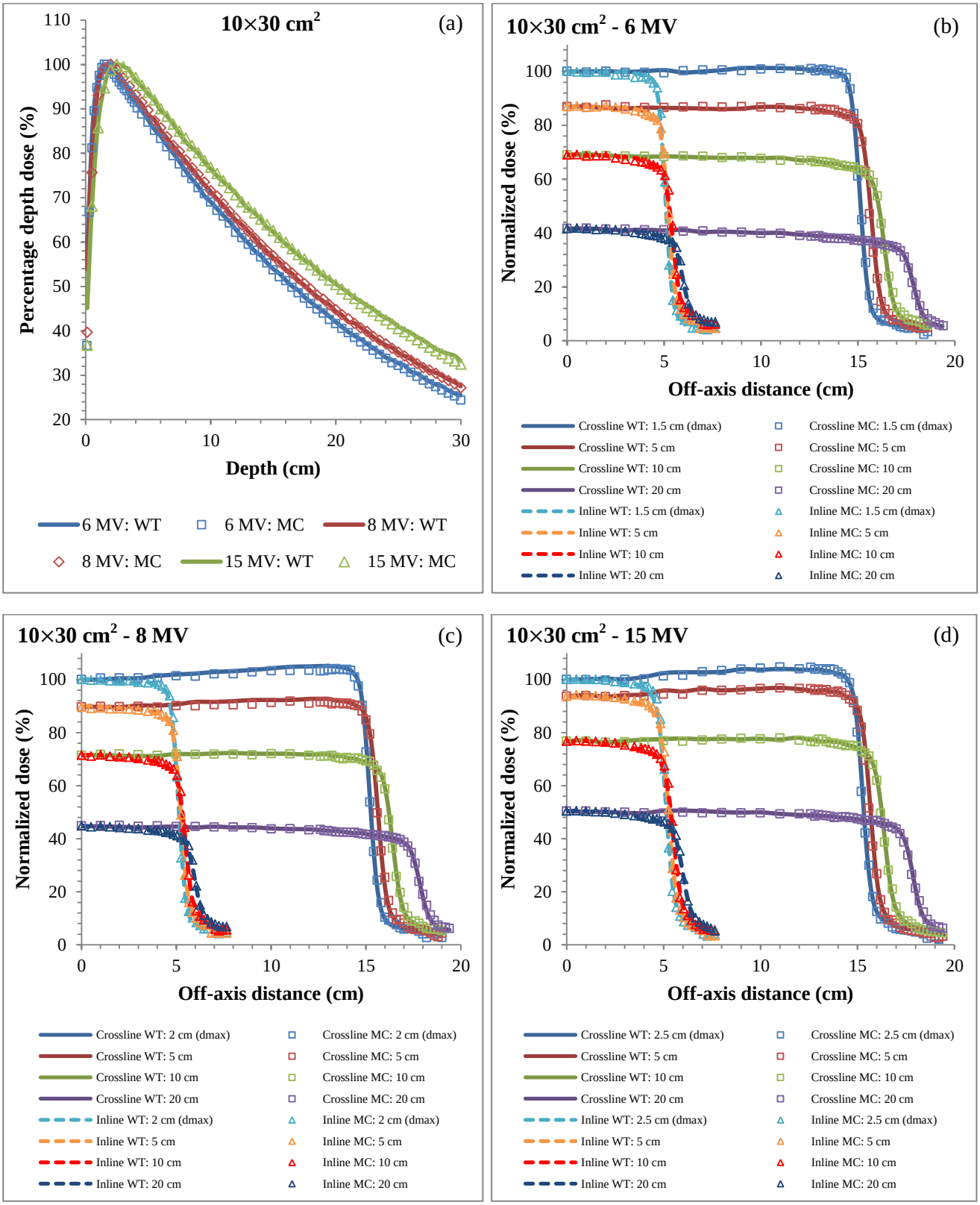

Fig. 4.23: Comparison of dose data for a 10×30 cm^2 rectangular FS aperture (a) PDD curves for various energies and (b – d) crossline and inline profiles for the 6, 8 and 15 MV beams respectively.

4.2.2.4 Aperture size: 30×10 cm^2

Fig. 4.24 (a) displays similar data compared to Fig. 4.22 for the 30×10 cm^2 FS.

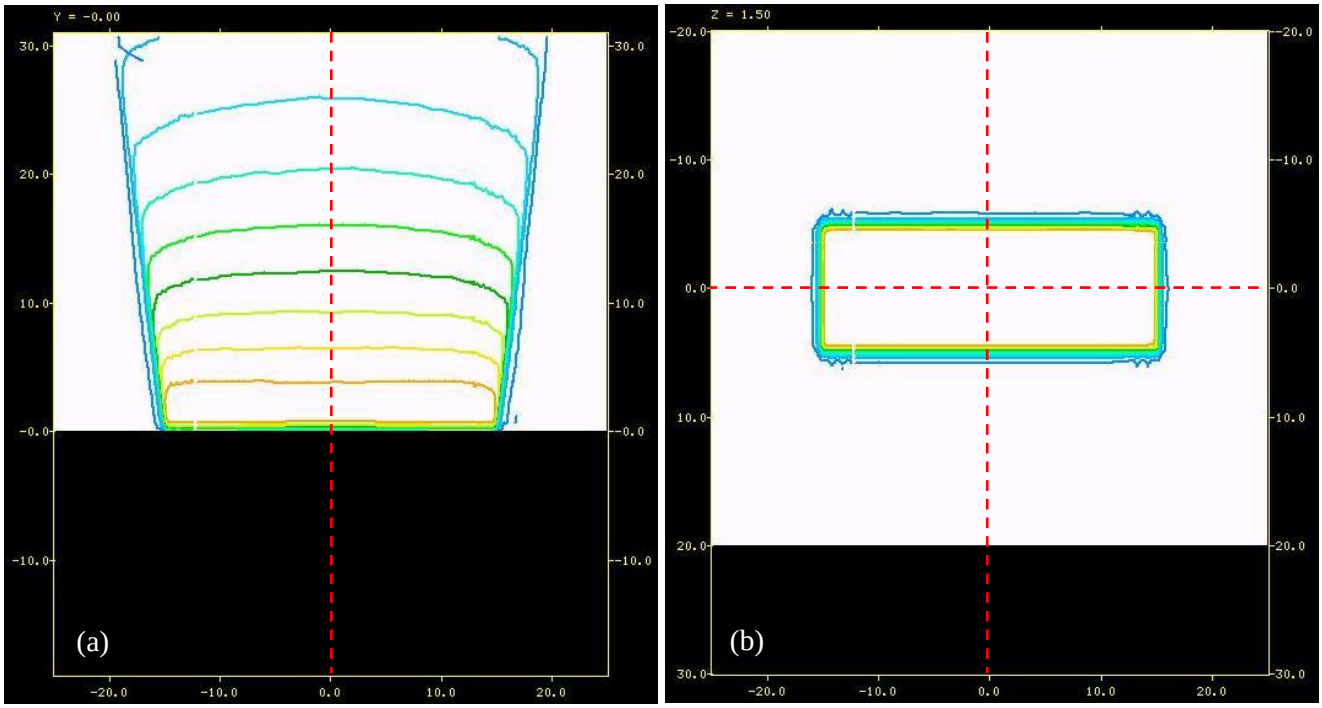

Fig. 4.24: (a) Coronal and (b) transverse slices displaying dose distributions for the 30×10 cm^2 FS for 6 MV beam in *mcshow*. PDD and dose profile data were extracted along the red dash lines and is shown in the next figure.

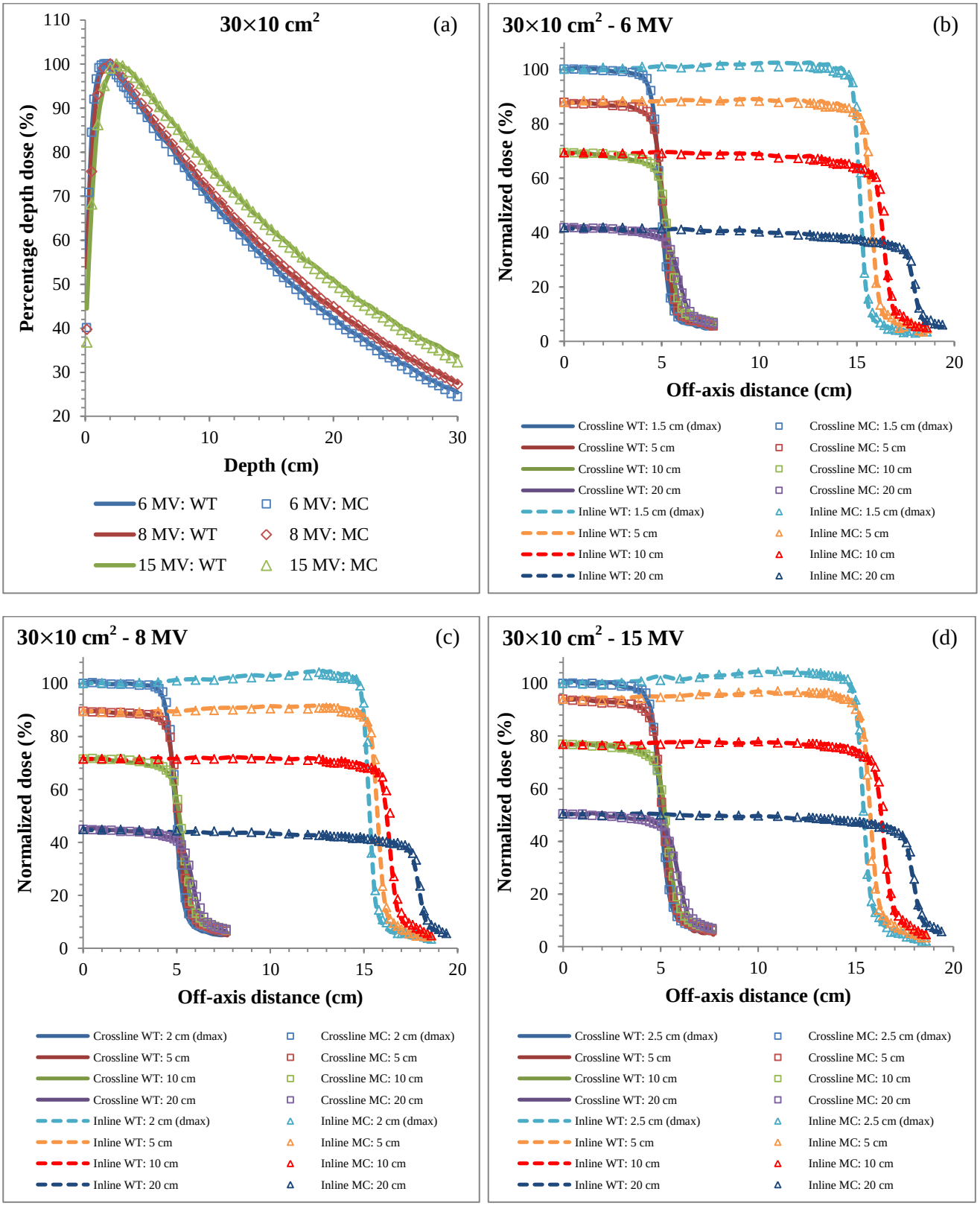

Fig. 4.25: Comparison dose data for a 30×10 cm^2 rectangular FS aperture (a) PDD curves for various energies and (b – d) crossline and inline profiles for the 6, 8 and 15 MV beams respectively.

4.2.3: Off-set field apertures

In order to test the model for asymmetrical geometries, off-set FS apertures were simulated and compared to measured data. Using the previously determined source model parameters derived from the square FS apertures, the following FS apertures were off-set and simulated and compared to measured data: 10×10, 15×15 and 20×20 cm^2. Apertures were off-set in both X- and Y-directions by various distances. PDD, crossline or inline profiles (depending on the direction of the off-set) are displayed in the figures below. The γ-index criteria was met in most cases (unless otherwise stated), with the MC variance below 1.0 %.

4.2.3.1 Aperture size: 10×10 cm^2 off-set 2.5 cm in X-direction

Fig. 4.26 (a) displays the coronal slice at isocenter of the dose distribution in the water phantom for 6 MV beam in *mcshow*. Fig. 4.29 (b) displays the transverse slice at d_{max} = 1.5 cm depth.

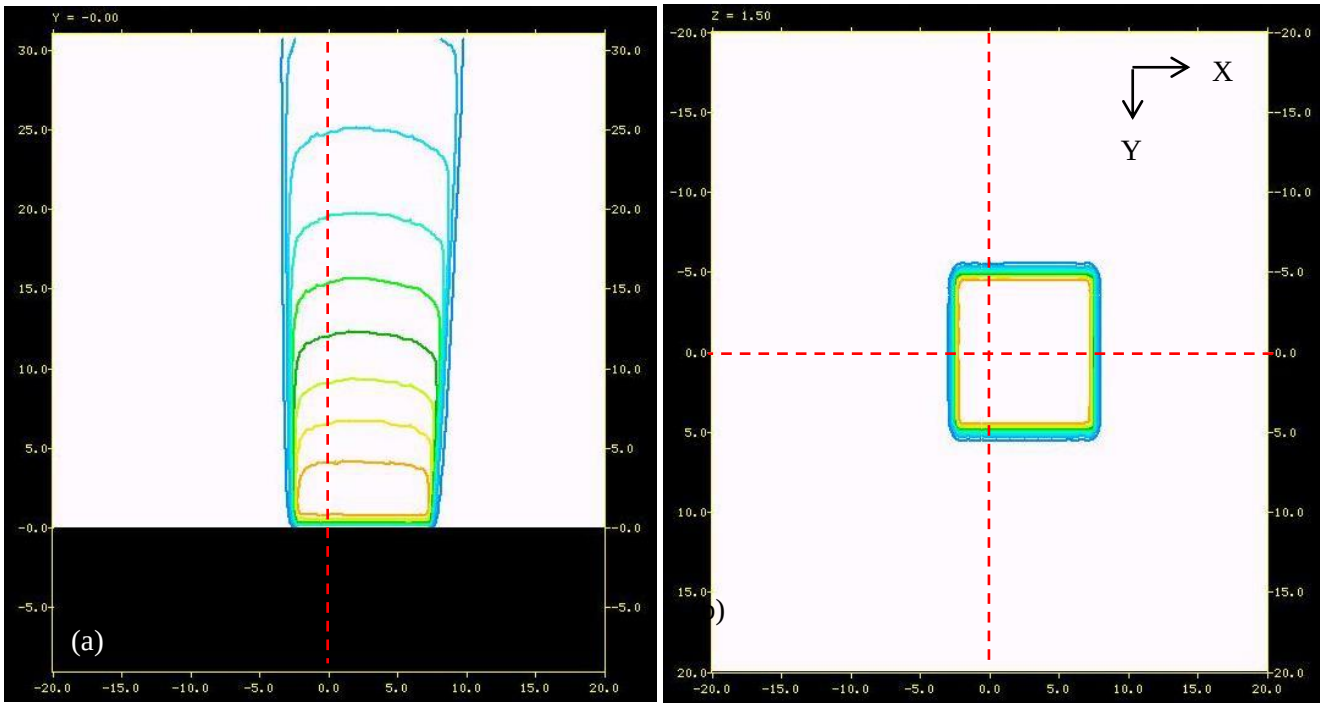

Fig. 4.26: (a) Coronal and (b) transverse slices displaying dose profiles of 10×10 cm^2 off-set aperture, which is set to 2.5 cm in the X-direction. Data were taken along the red dash lines.

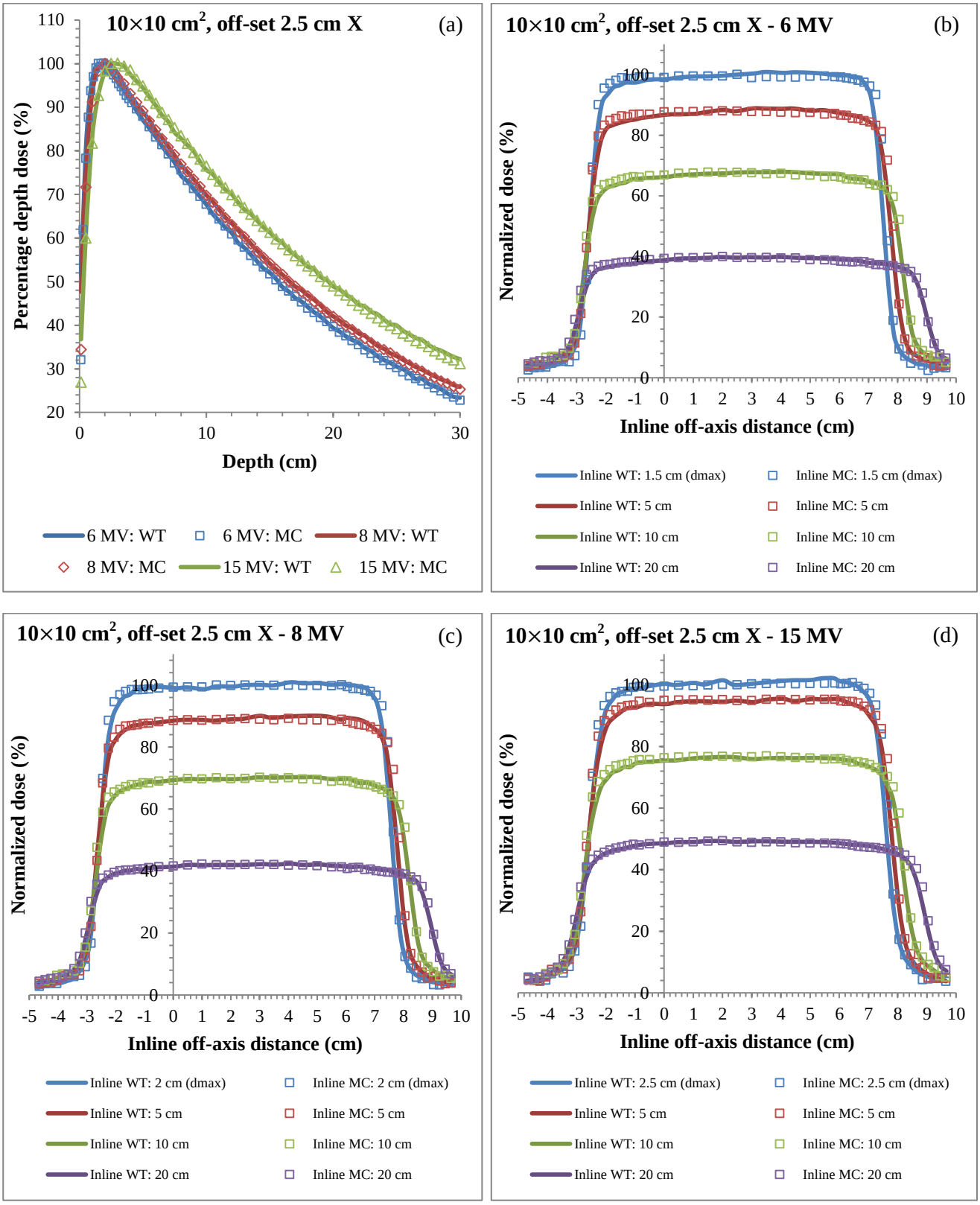

Fig. 4.27: Comparison of dose data for the 10×10 cm^2 off-set FS aperture, set to 2.5 cm in the X-direction (a) PDD curves for various energies and (b – d) inline profiles for the 6, 8 and 15 MV beams respectively.

4.2.3.2 Aperture size: 10×10 cm^2 off-set -5.0 cm in Y-direction

Fig. 4.28 displays similar data but this time for the -5.0 cm off-set case.

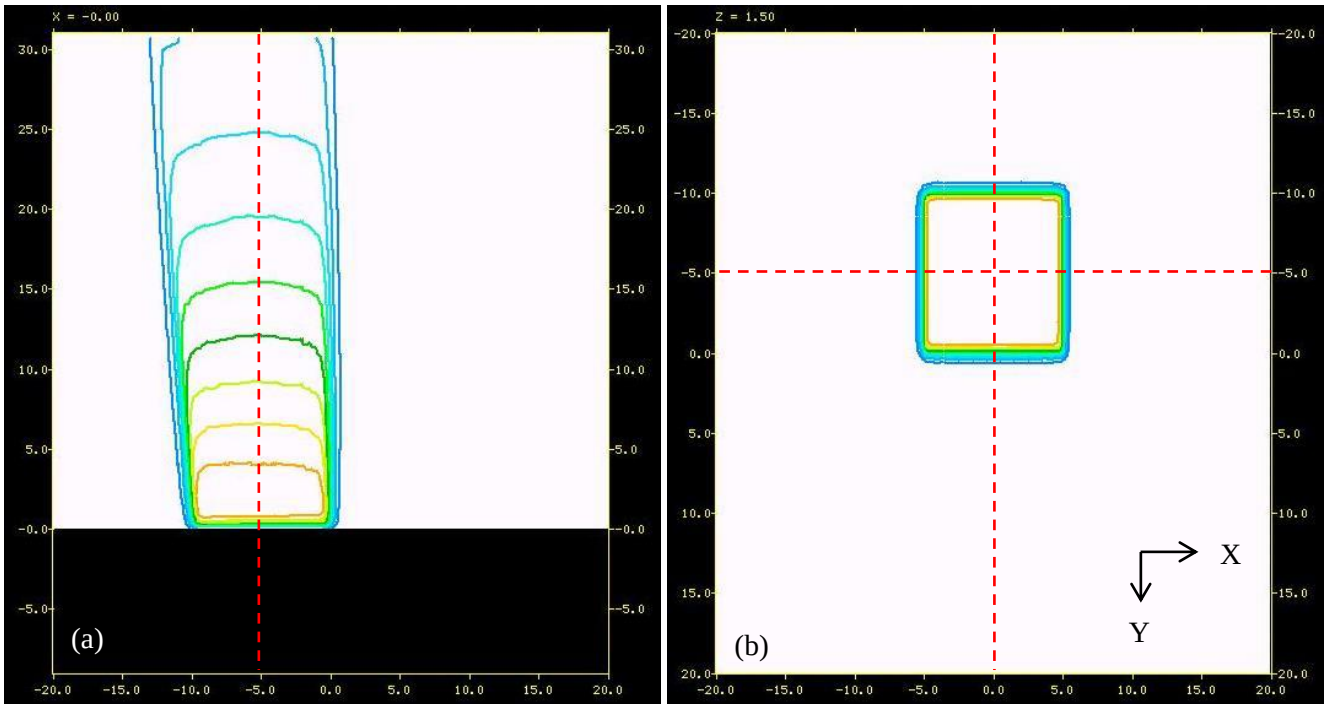

Fig. 4.28: (a) Coronal and (b) transverse slices displaying dose profiles of 10×10 cm^2 off-set aperture, -5.0 cm in the Y-direction.

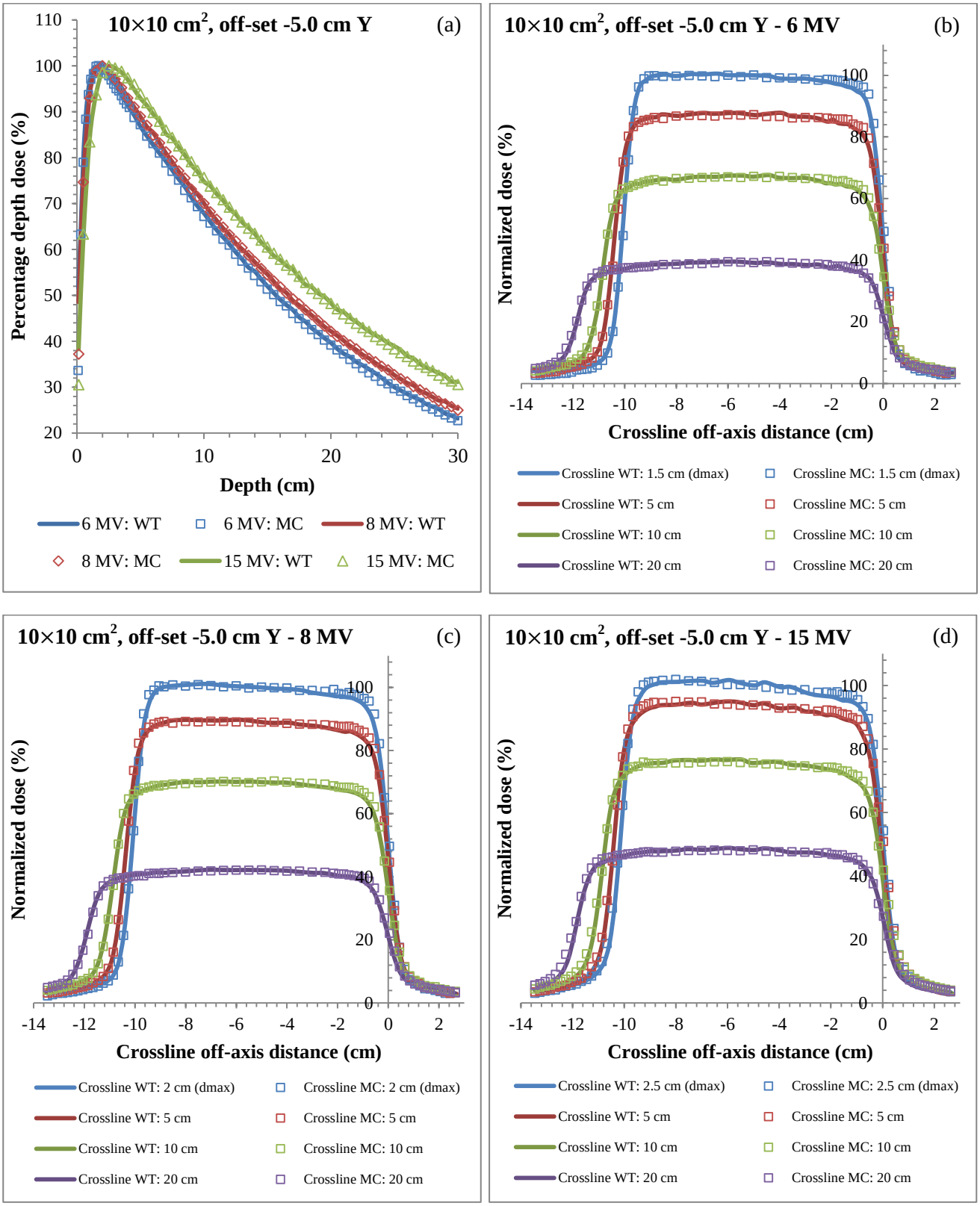

Fig. 4.29: Comparison of dose data for a 10×10 cm^2 off-set FS aperture, -5.0 cm in the Y-direction (a) PDD curves for various energies and (b – d) crossline profiles for the 6, 8 and 15 MV beams respectively.

4.2.3.3 Aperture size: 15×15 cm^2 off-set -3.0 cm in Y-direction

Fig. 4.30 display data for the 15×15 cm^2 FS which is off-set -3.0 cm in the Y-direction.

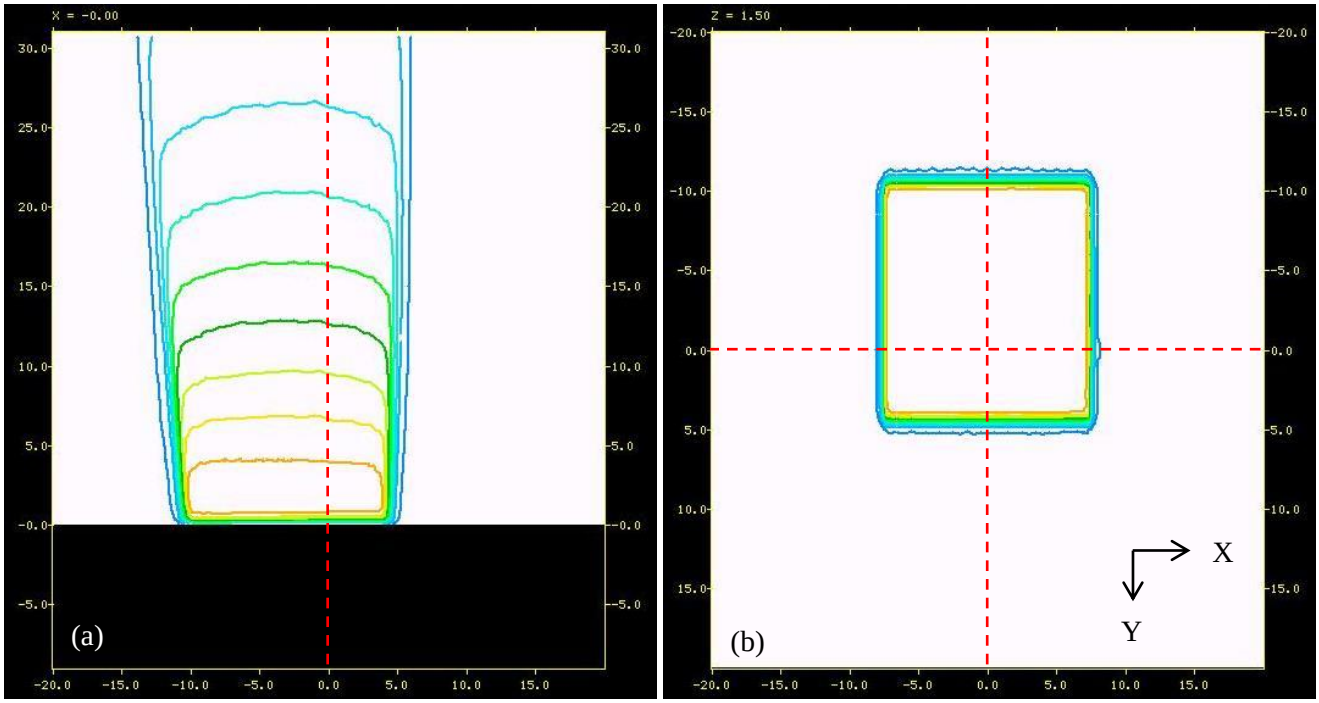

Fig. 4.30: (a) Coronal and (b) transverse slices displaying dose profiles of 15×15 cm^2 off-set aperture, -3.0 cm in the Y-direction.

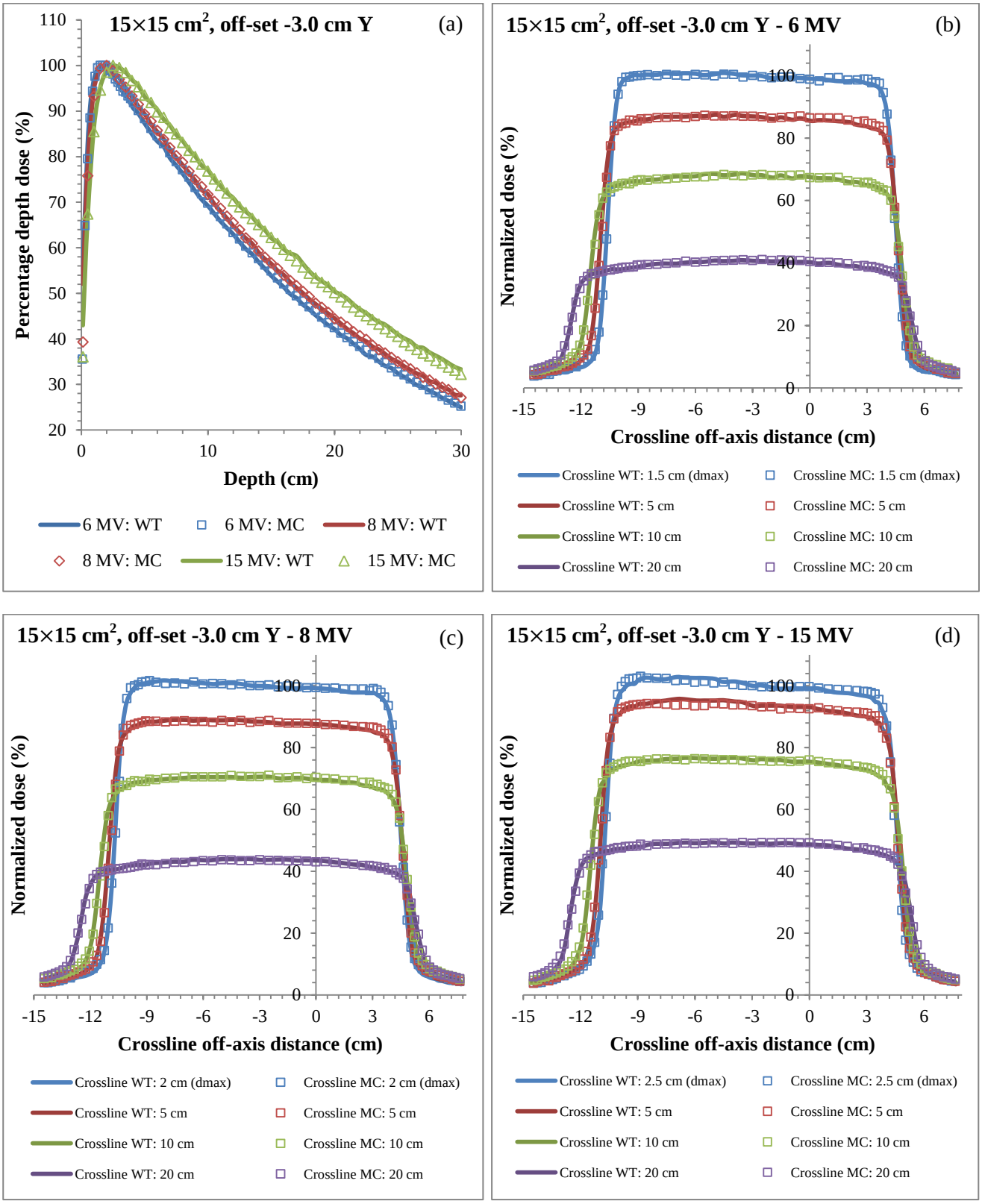

Fig. 4.31: Comparison of dose data for a 15×15 cm^2 off-set FS aperture, -3.0 cm in the Y-direction (a) PDD data for various energies and (b – d) crossline profiles for the 6, 8 and 15 MV beams respectively.

4.2.3.4 Aperture size: 15×15 cm^2 off-set 7.5 cm in X-direction

Fig. 4.32 displays similar data for the same field but now with an off-set of 7.5 cm in the X-direction.

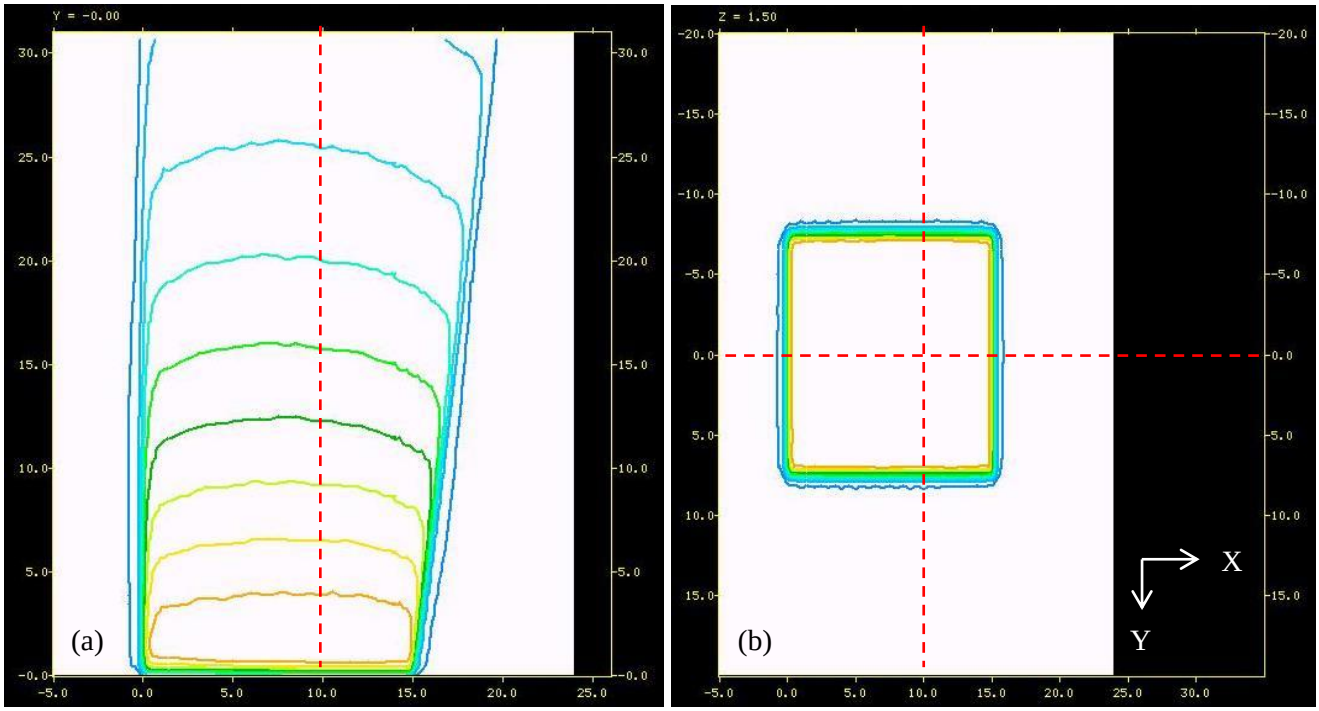

Fig. 4.32: (a) Coronal and (b) transverse slices displaying dose profiles for the 15×15 cm^2 off-set aperture, set at 7.5 cm in the X-direction.

The inline profiles from WT dose measurements and MC simulations for 6 MV at depths 1.5 and 20 cm are displayed in Fig. 4.33 (a) and (b) respectively. The dose profiles displayed were normalized to be 100 % at position 7.5 cm in the X-direction. The γ-index was not met for all dose points, where the green dash curves (γ-index of 2 % / 2 mm) cross the red dash lines. For a γ-index with criteria of 3 % / 2 mm, the criterion was met at all dose points.

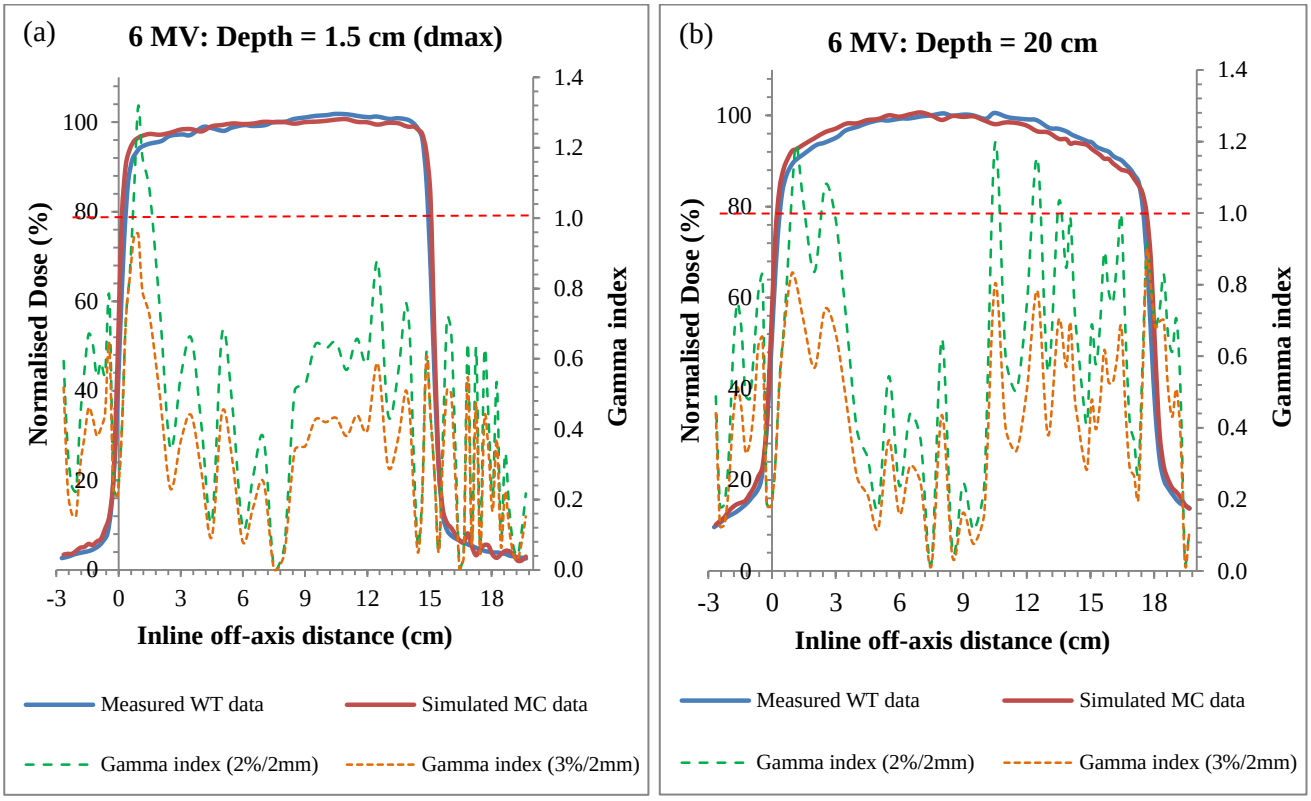

Fig. 4.33: Inline profiles for the 15×15 cm^2 off-set aperture, set to 7.5 cm in the X-direction, for 6 MV, at depth of (a) 1.5cm (d_{max}) and (b) 20 cm.

After additional simulations using various values for the *psig4* parameter, the γ-index passed with a *psig4* parameter value of 80. This parameter is the FWHM of the Gaussian function for the target fluence. By changing this parameter to a larger value, as described in section 2.2.3.1, the fluence will increase at the off-axis region. Although the aim was to keep this parameter constant for each energy, the change in parameter value was required for the comparison to pass the criteria. The final PDD and inline profiles for WT dose measurements and MC simulations for the various energies are displayed in Fig. 4.34. The dose profiles displayed are normalized to its local PDD, taken at position 7.5 cm in the X-direction.

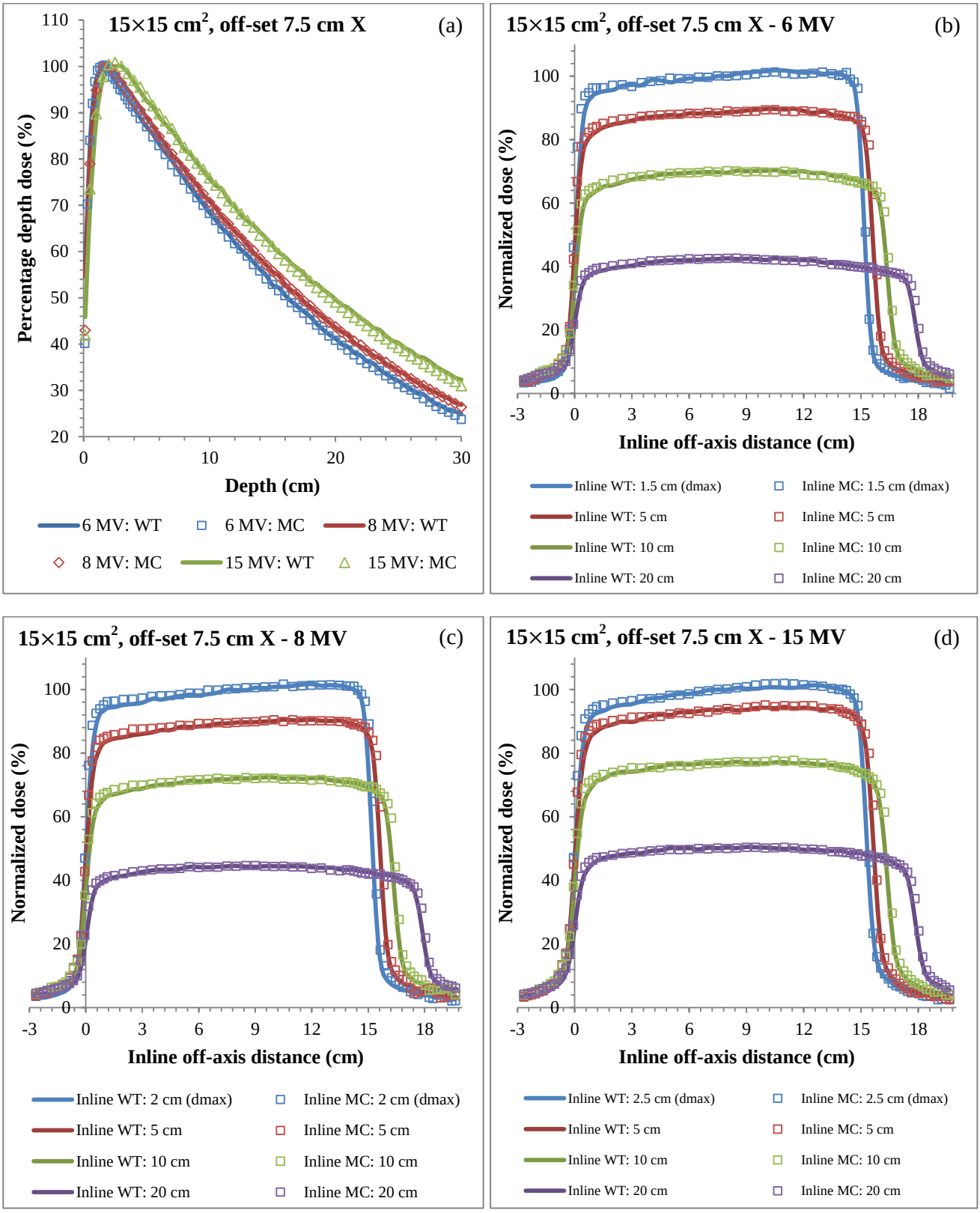

Fig. 4.34: Comparison of dose data for a 15×15 cm^2 off-set FS aperture, set to 7.5 cm in the X-direction (a) PDD data for various energies and (b – d) inline profiles for the 6, 8 and 15 MV beams respectively.

4.2.3.5 Aperture size: 20×20 cm^2 off-set -5.0 cm in X-direction

Fig. 4.35 shows the case for the 20×20 cm^2 field with an off-set of -5 cm in the X-direction.

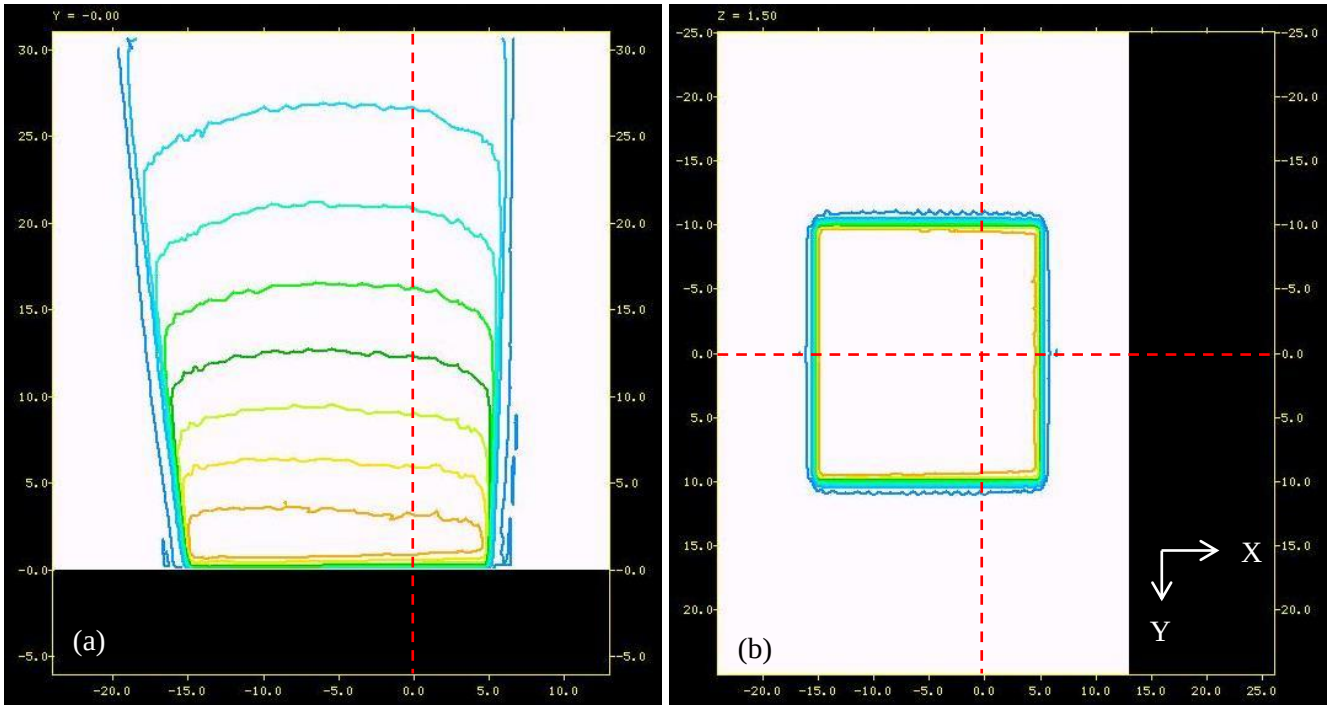

Fig. 4.35: (a) Coronal and (b) transverse slices displaying dose profiles for the 20×20 cm^2 off-set aperture, with an off-set of -5.0 cm in the X-direction, for a 6 MV beam in *mcshow*.

Inline profiles from WT dose measurements and MC simulations for a 6 MV at depths 5 and 10 cm are displayed in Fig. 4.36 (a) and (b) respectively. The dose profiles displayed were normalized to be 100 % at position -5.0 cm in the X-direction. The γ-index also failed as in the previous FS case, but passed at all points for criteria of 3 % / 2mm.

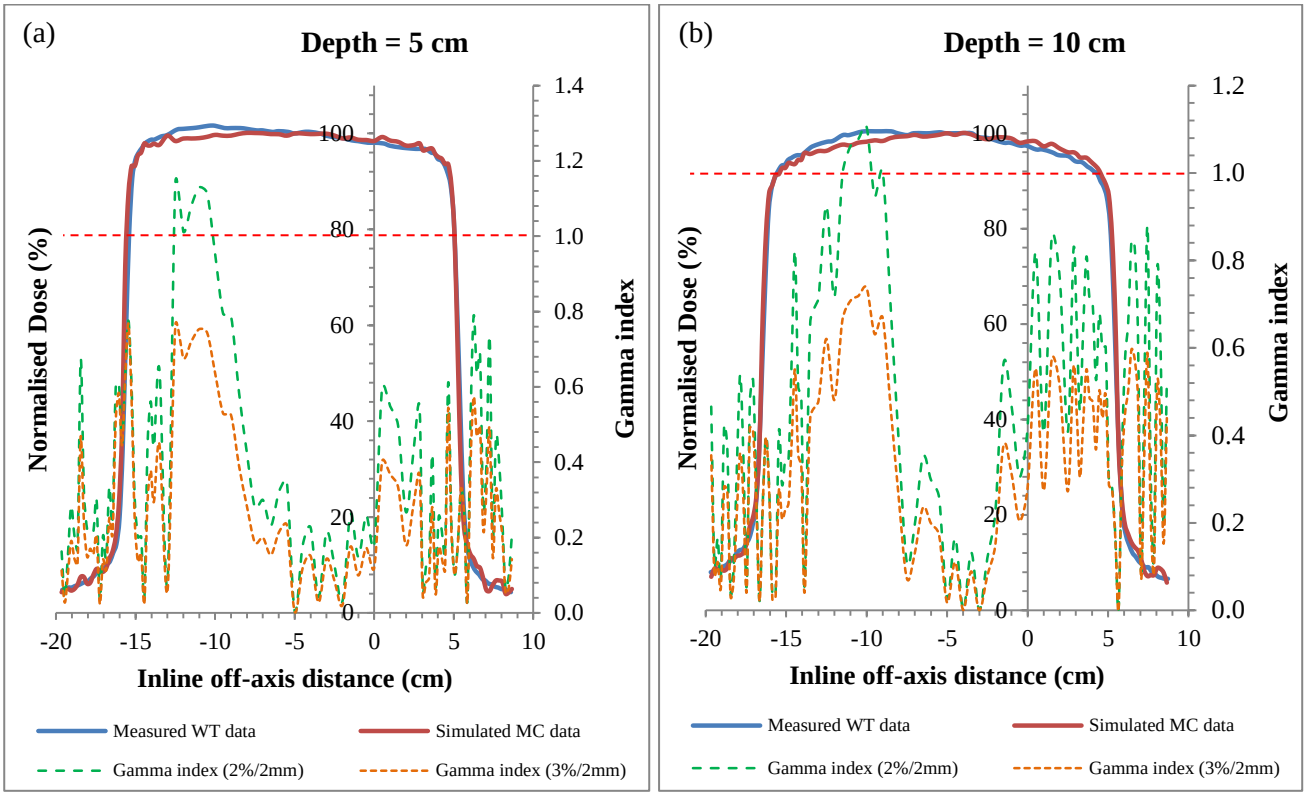

Fig. 4.36: Inline profiles for the 20×20 cm^2 off-set aperture, set to -5.0 cm in the X-direction, for 6 MV, at a depth of (a) 5 cm and (b) 10 cm.

A *psig4* parameter value of 80 could make the model fit with the WT data to satisfactory with criteria of 2 % / 2 mm, and is shown in Fig. 4.37. The various depth profiles were normalized to the local PDD taken at position -5.0 cm in the X-direction.

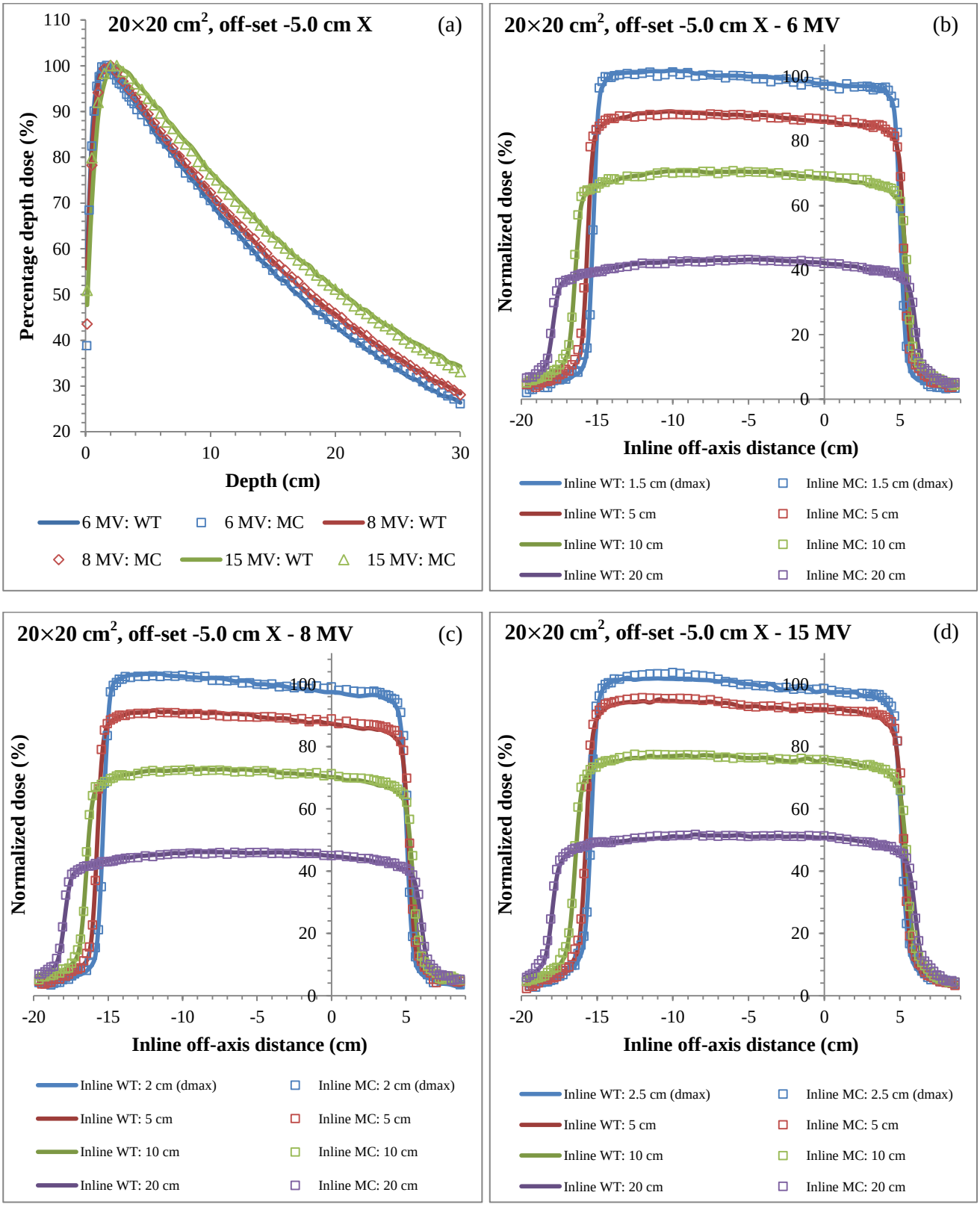

Fig. 4.37: Comparison of dose data for a 20×20 cm^2 off-set FS aperture, set to -5.0 cm in the X-direction (a) PDD data for various energies and (b – d) inline profiles for the 6, 8 and 15 MV beams respectively.

4.2.3.6 Aperture size: 20×20 cm^2 offset 10.0 cm in Y- direction

Fig. 4.38 shows data for the 20×20 cm^2 FS with an off-set of 10.0 cm in the Y-direction.

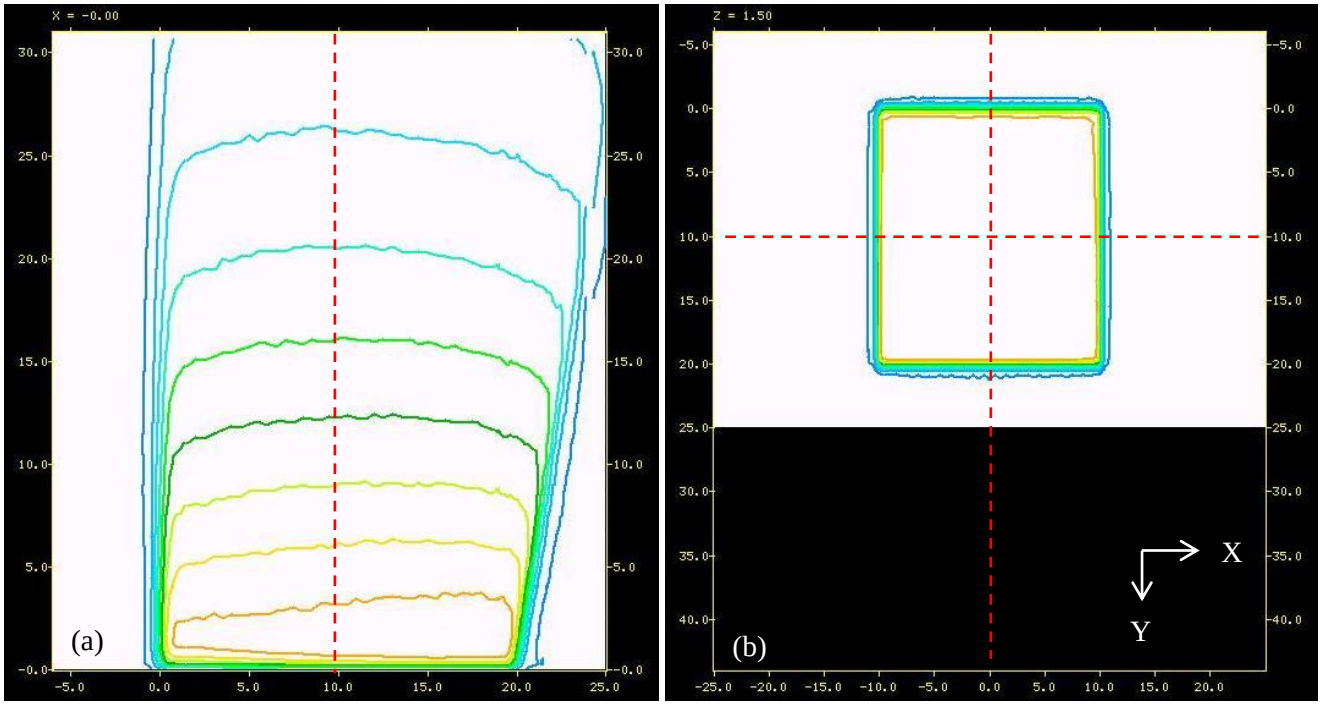

Fig. 4.38: (a) Coronal and (b) transverse slices displaying dose profiles of 20×20 cm^2 offset aperture, with an off-set of 10.0 cm in the Y-direction.

PDD profiles from WT dose measurements and MC simulations for all energies are displayed in Fig. 4.39, with the γ-index for all the comparisons performed passed.

Crossline profiles from WT dose measurements and MC simulations for 6 MV at depths of 1.5 and 20 cm are displayed in Fig. 4.40 (a) and (b) respectively. The various depth profiles displayed were normalized to 100 % at position y = 10.0 cm in the Y-direction. The γ-index criteria failed, where the green dash curves (γ-index of 2 % / 2 mm) cross the red dash lines. The γ-index with criteria of 3 % / 2 mm also failed.

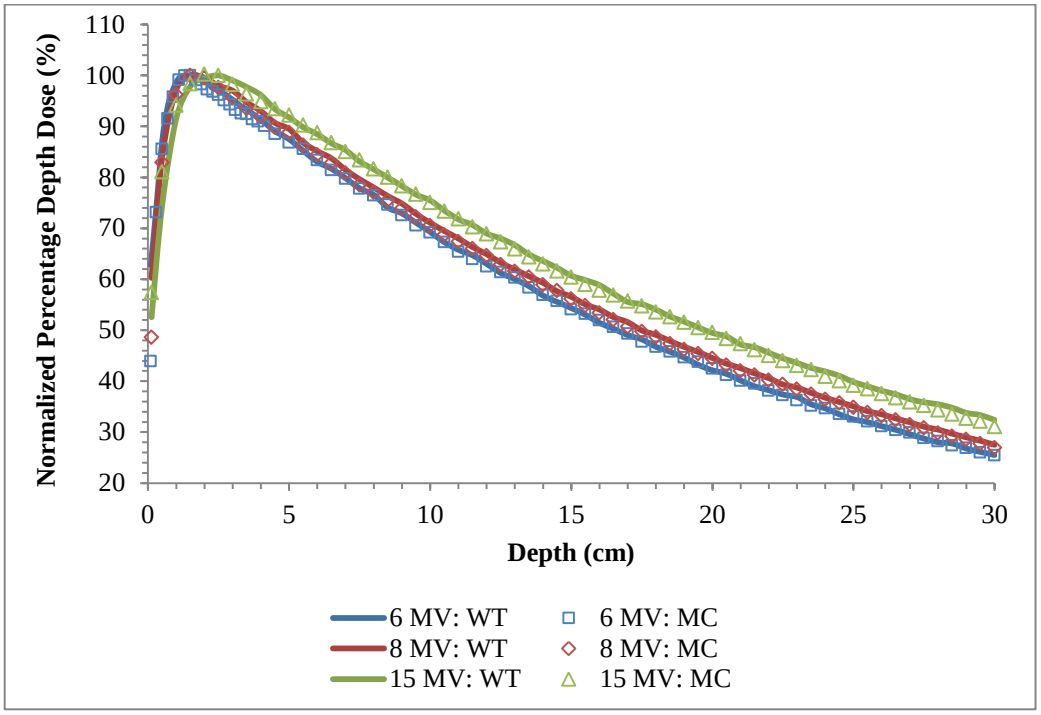

Fig. 4.39: PDD data for the 20×20 cm^2 off-set aperture, set to 10.0 cm in the Y-direction. The solid lines are the measured water tank (WT) dose data, with the square, diamond and triangle symbols the Monte Carlo (MC) dose data for 6, 8 and 15 MV respectively.

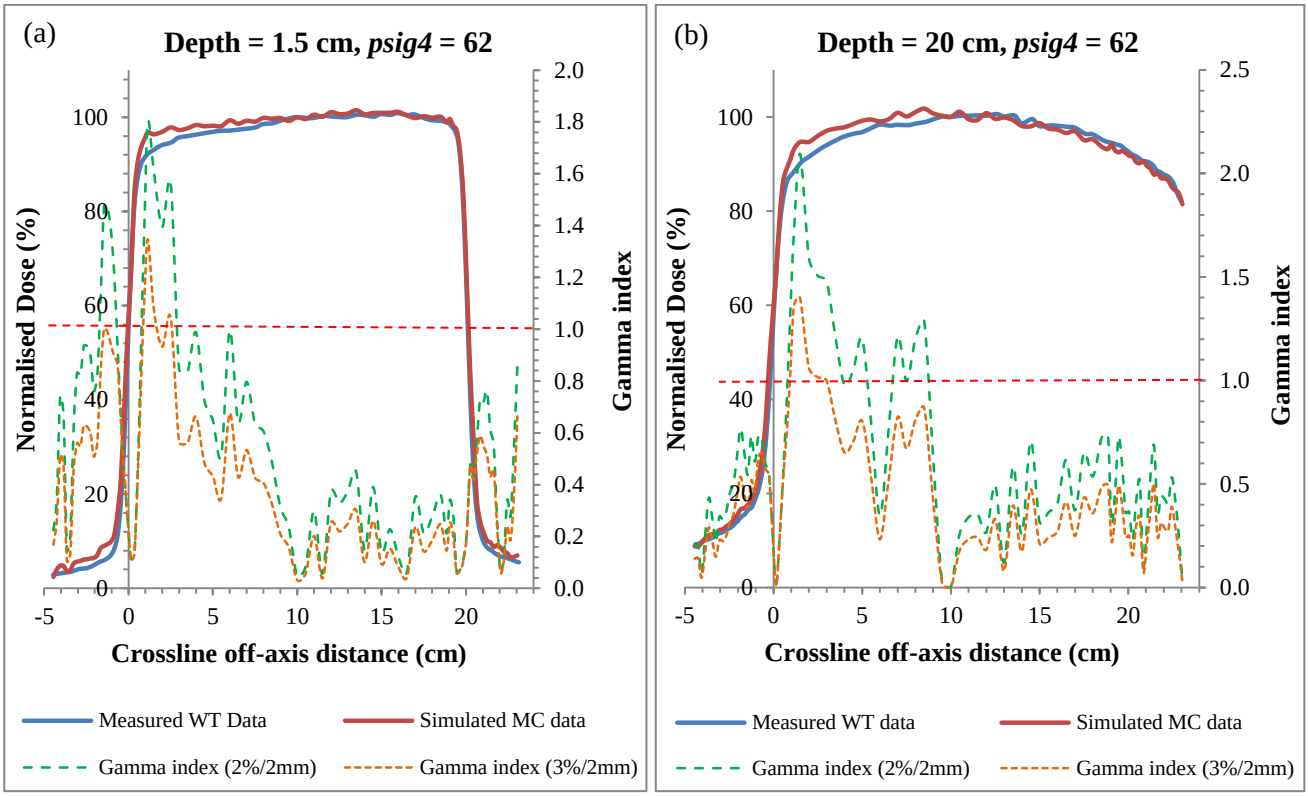

Fig. 4.40: Crossline profiles in the Y-direction for the 20×20 cm^2 off-set aperture, set to 10.0 cm for the 6 MV, at depth of (a) 1.5 cm (d_{max}) and (b) 20 cm. The green and orange dash lines indicate the γ-index values.

Various values for the *psig4* parameter ranging from 74 to 91 were simulated in order to find a suitable comparison for the off-set field aperture for 6 MV. No satisfactory solution was found. The *trans_jaw_Y* parameter value was also changed to 0.352 in order for the transmission to fit. The remaining depth crossline profiles failed the comparison at points mainly near the field edges, but passed over the central portion of the beam. The comparison of the inline profiles passed the γ-index criteria.

For the 8 MV beam, the crossline profiles from WT dose measurements and MC simulations at depths of 2 and 5 cm are displayed in Fig. 4.41 (a) and (b) respectively. The various depth profiles were normalized to 100 % at position y = 10.0 cm. The γ-index failed, as can be seen in Fig. 4.41 (b) at some dose points close to the field edge, where the green dash curves (γ-index of 2 % / 2 mm) cross the red dash line. The γ-index with criteria of 3 % / 2 mm failed in the same location as the 2 % / 2 mm case.

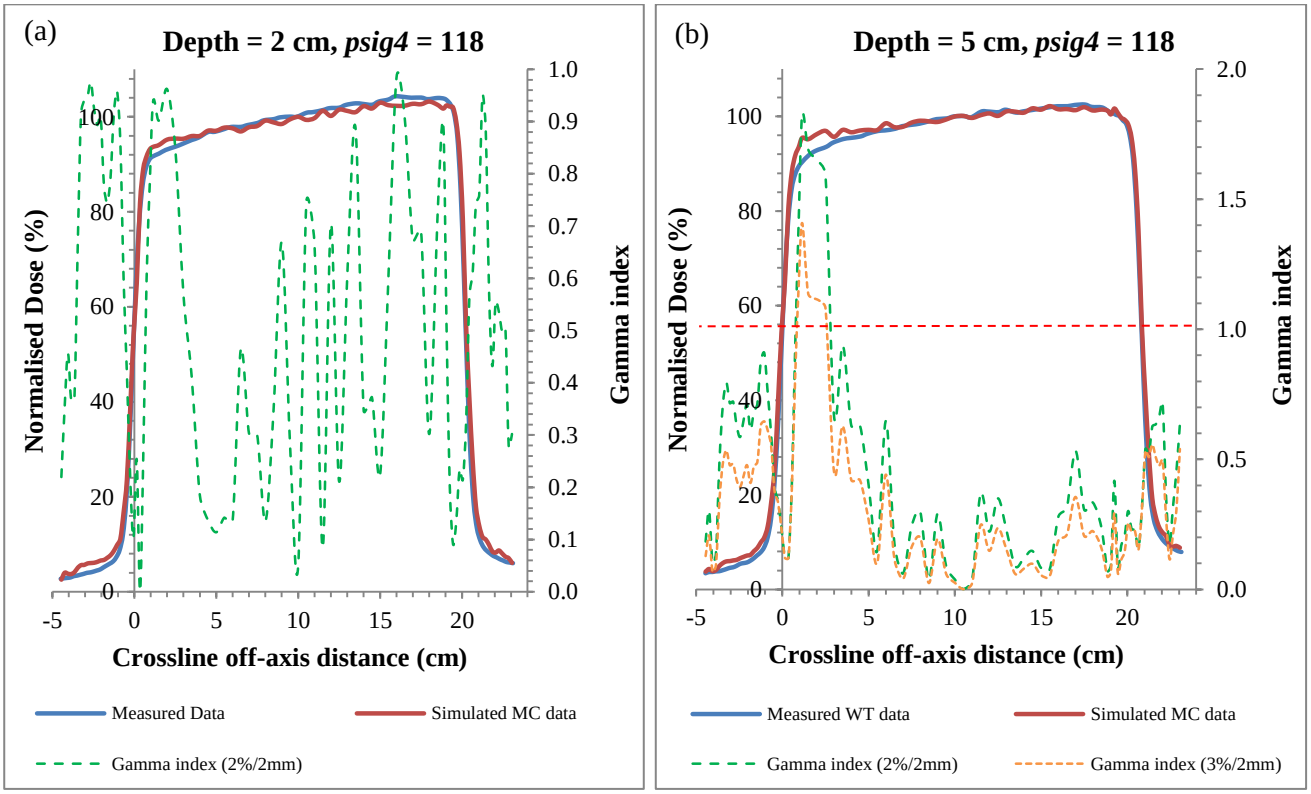

Fig. 4.41: Crossline profiles for the 20×20 cm^2 off-set aperture, set to 10.0 cm in the Y-direction, for the 8 MV beam, at depths of (a) 2 and (b) 5 cm.

From Fig. 4.41, it can be seen that the γ-index criteria is met for the d_{max} crossline profile (Fig. 4.41 (a)). Fig. 4.42 (a) and (b) displays the 2 and 5 cm depth crossline profiles respectively for the *psig4* parameter value of 150. The simulated data compared well with the WT data, except for a small region near the field edge at 5 cm depth.

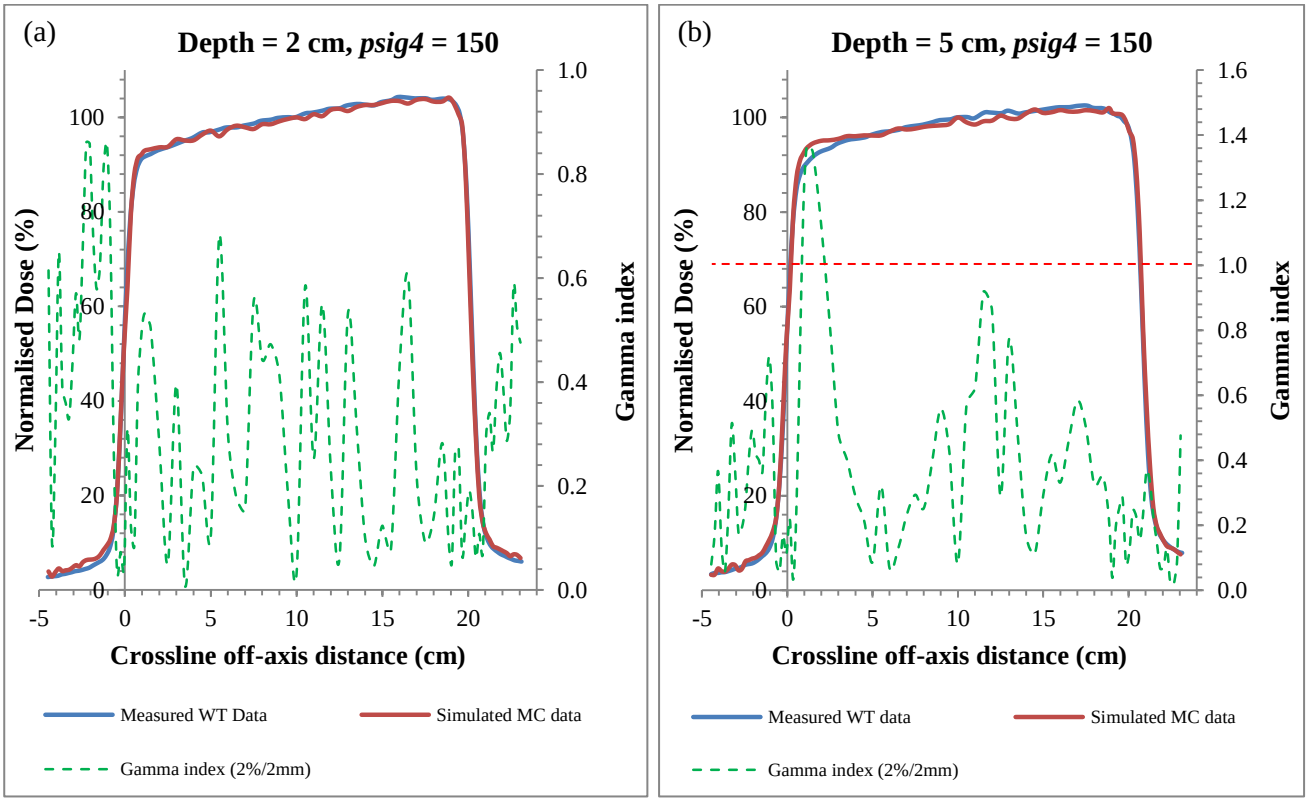

Fig. 4.42: Crossline profiles for the 20×20 cm^2 off-set aperture, set to 10.0 cm in the Y-direction, for the 8 MV beam, at depths of (a) 2 and (b) 5 cm for *psig4* = 150.

For the 15 MV beam, the crossline profiles from WT dose measurements and MC simulations at depths of 2.5 and 5 cm are displayed in Fig. 4.43 (a) and (b) respectively. The depth profiles displayed were normalized to be 100 % at position y = 10.0 cm. The γ-index criteria for the comparisons failed at nearly 25 % of data points near the field edge. It is indicated where the green dash curves (γ-index of 2 % / 2 mm) cross the red dash lines. The γ-index with criteria of 3 % / 2 mm showed similar failure regions.

From Fig. 4.43 (a) and (b), it can be seen that the comparison failed for the d_{max} and 5 cm depth crossline profiles. 10 and 20 cm depth crossline profiles (not shown) also failed their γ-index criteria, even with an index value set at 3 % / 2 mm. Various values for the *psig4* parameter were used in simulations in order to find a suitable comparison for the 15 MV's off-set field apertures. However, all depth crossline profiles failed the evaluation criteria in some regions of the field edge.

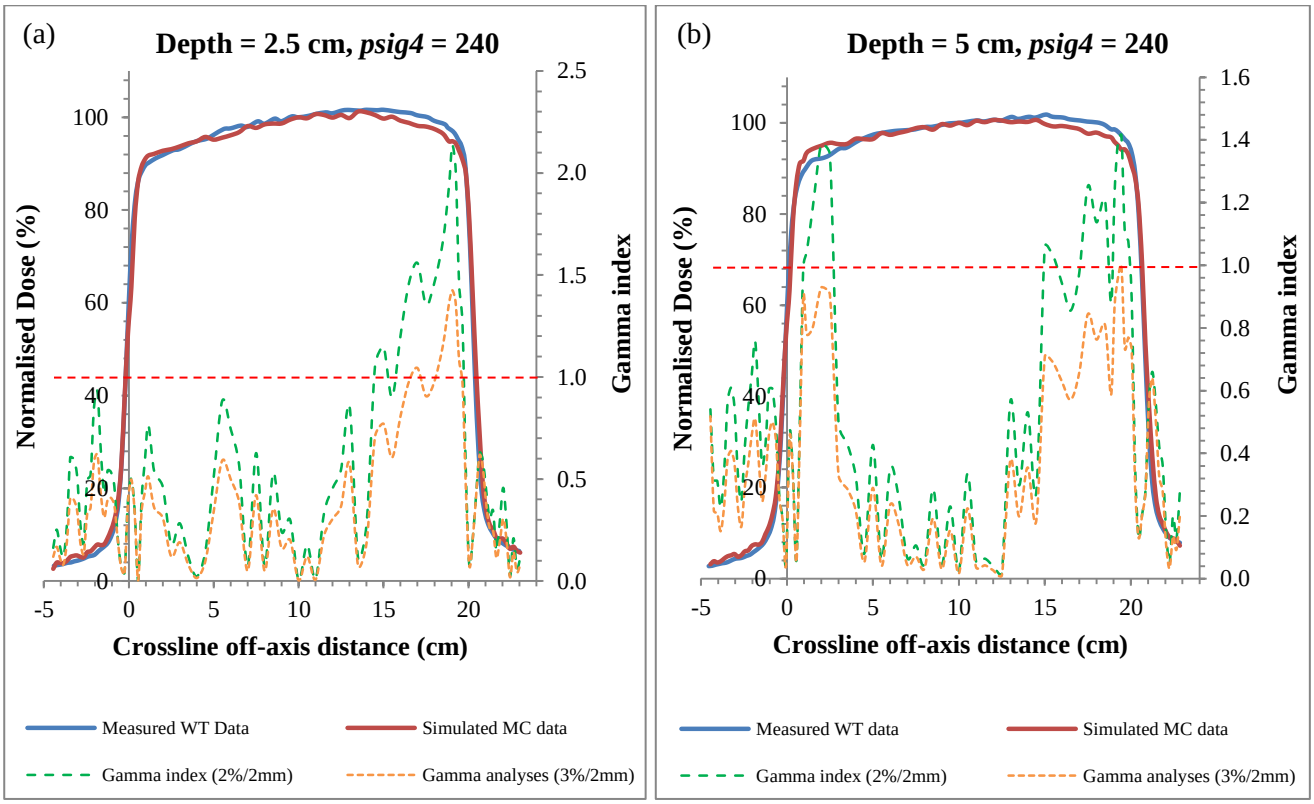

Fig. 4.43: Crossline profiles for the 20×20 cm^2 off-set aperture, set at 10.0 cm in the Y-direction, for 15 MV, at depths of (a) 2 and (b) 5 cm for *psig4* = 240.

It can be concluded that the source model is not ideal for large FS apertures that are off-set over large distances further away from the CAX, as the comparison between the measured WT and simulated MC dose distributions failed the evaluation criteria of 2 % / 2 mm. The source model is very accurate for symmetrical geometries, which includes the square and rectangular FS apertures using the benchmarked parameters as illustrated in the previous sections. For the asymmetrical geometries, for example the small and medium size apertures, the model performs very well. However, for the larger

size apertures, the model struggles to accurately replicate the true beam data. Possible reasons for this can be attributed to the fact that a point source is used for photons with no extra-focal scatter sources. This source model incorporates collimator scatter as adjustment of the beam penumbra. For extreme conditions, e.g. large field problems begin to develop at the field edges in the off-set cases.

4.2.4: Irregular field apertures

4.2.4.1 Film calibration

In section 4.1 the properties of the film scanners were determined in their use in GAFCHROMIC® EBT2 film dosimetry. For the irregular FS aperture study, film measurements were taken and the process and results of the film dosimetry used are now described.

The average red pixel values for the 6, 8 and 15 MV energy beams are displayed in Table 4.8. To obtain this, a ROI of 40×40 pixels was drawn in using ImageJ software to calculate the average pixel values for the film pieces scanned. These film pieces were irradiated according to the values indicated in the left column in Table 4.8.

Table 4.8: Average red pixel values from 6, 8 and 15 MV photon energies, as well as their average over the three beam energies and their standard deviation.

Dose (cGy)	**Energy (MV)**			**Average**	**Standard Deviation**
	6	**8**	**15**		
0	87.02	88.07	89.49	**88.19**	*1.24*
10	101.73	103.49	103.81	**103.01**	*1.12*
20	114.04	116.73	117.09	**115.95**	*1.67*
40	128.76	132.23	132.59	**131.19**	*2.12*
80	153.32	155.75	154.69	**154.59**	*1.22*
120	169.18	171.34	171.02	**170.51**	*1.17*
160	183.44	184.99	184.32	**184.25**	*0.78*
200	193.37	195.59	194.52	**194.49**	*1.11*
250	204.31	206.07	205.47	**205.28**	*0.89*
300	213.21	213.11	212.19	**212.81**	*0.53*

The average red pixel values among the three energies compared well with each other at the corresponding doses under consideration, as shown in Table 4.8. A maximum standard deviation value of 2.12 occurs at 40 cGy absorbed dose. From the data in Table 4.8, calibration curves for each energy (Fig. 4.44) were drawn to convert pixel values to absorbed dose. A third degree polynomial function was fitted through the data points, to relate a given red pixel value to its corresponding absorbed dose value.

From the results in Table 4.8 the film is nearly energy independent for MV photon energies, which are also stated by ISP[36]. Butson *et al* reported a 6.5% dose difference between energies ranging from 50 kVp to 10 MV. This value is smaller and more energy independent than its predecessor, EBT film, with a dose difference of 7.7% over the same energy range[72]. Here we have much less deviation among the data since all energies are in the low MV range.

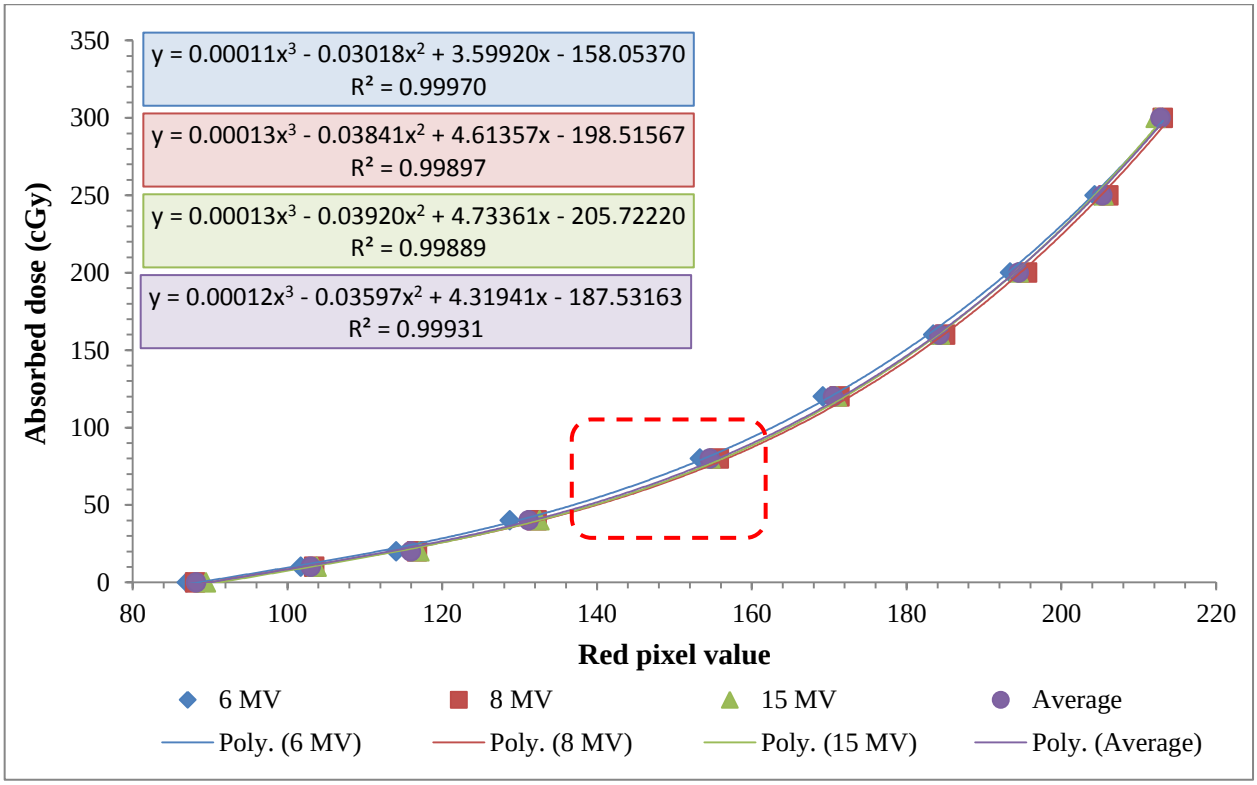

Fig. 4.44: Calibration curves of absorbed dose vs. red pixel value for the 6, 8 and 15 MV photon energy beams, along with the average. The fitted curves are third degree polynomial functions. The red dashed box indicates the area where the fitted curves, used for output factor dose conversion, will produce different dose values for the same pixel values.

4.2.4.2 Dose comparison using benchmarked parameters

Using the source modelling parameters derived from the square FS data, a *Triangle*, *Arrow* and *Mirror E* irregular FS shapes were simulated and evaluated against measured film data. The film response was converted using a pixel-to-dose calibration curve (Fig. 4.44) for each energy. Crossline and inline profiles were obtained from both the film and MC simulation data, and compared to one another.

A. Triangle field

Fig. 4.45 (a) and (b) shows the scanned film image and sagittal slice for 6 MV in *mcshow* for the *Triangle* FS aperture. Fig. 4.45 (c) and (d) shows the crossline and inline profiles comparison between the converted film dose and the MC dose.

The crossline profile failed the γ-index criteria at some points (Fig. 4.45 (c)). This is due to the transmission through the MLC's which is higher for the MC dose compared to the film data. The model overestimated the transmission through the MLC's. To correct for this, *sigmax_mlc*, *sigmay_mlc* and *trans_mlc* parameters were adjusted and compared with the film dose data until the evaluation criteria was met.

Fig. 4.46 (a) and (b) shows the crossline and inline comparison profiles after adjustments were made to the above parameters. The parameter values, along with their respective benchmarked values, are displayed in Table 4.9.

Table 4.9: Benchmarked and final parameter values for MLC and jaw fluence for creating irregular FS apertures

Parameter	Head component	Benchmark	Final
sigmax_mlc	MLC's	0.400	0.028
sigmay_mlc		0.400	0.296
trans_mlc		0.020	0.070
trans_jaws_X	XY jaws	0.039	0.076
trans_jaws_Y		0.211	0.564

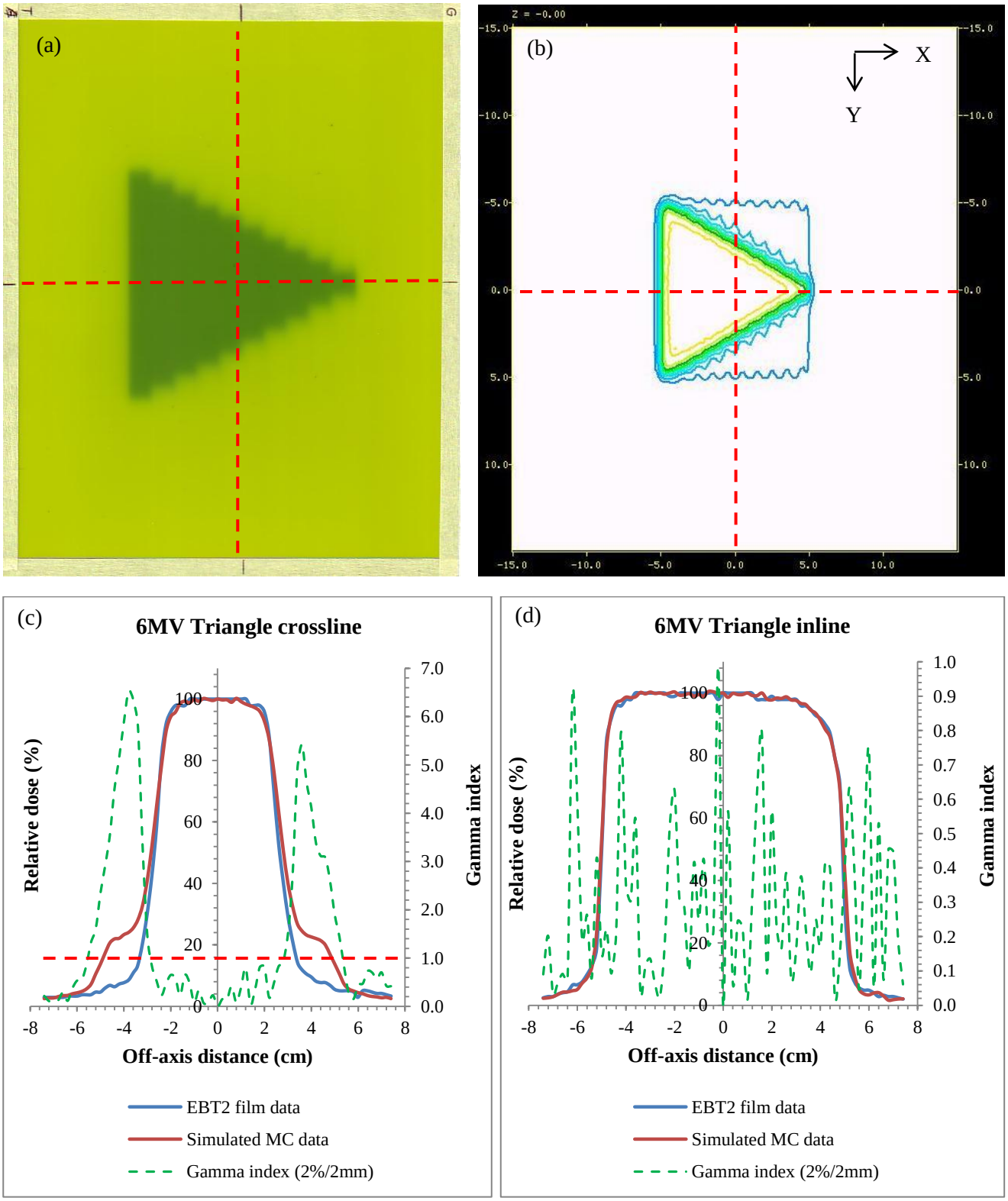

Fig. 4.45: Triangle FS aperture geometry for 6 MV: (a) film OD before conversion to dose; (b) sagittal slice at CAX displays in *mcshow*, the red dash lines indicated where the profile data were taken; (c) crossline and (d) inline profile comparisons. The crossline profile failed the evaluation at the field edges.

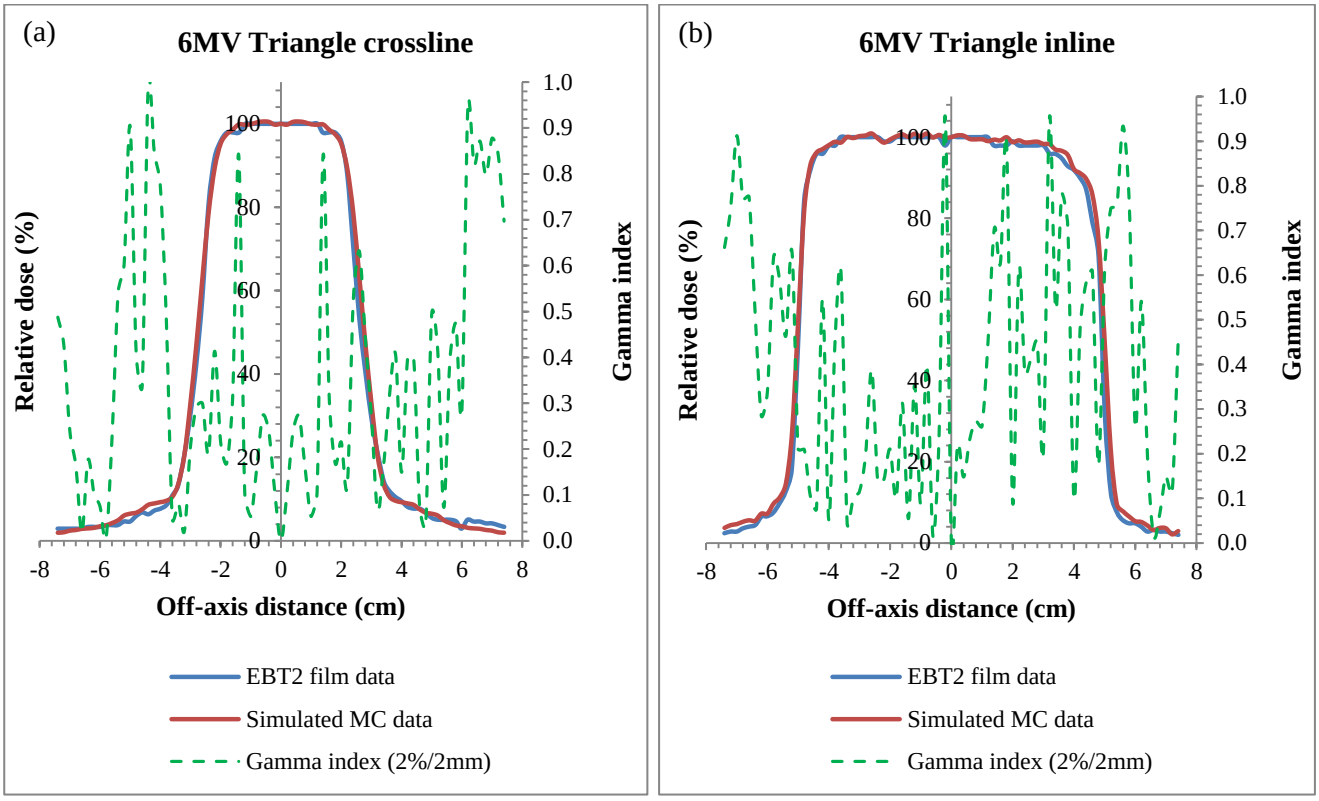

Fig. 4.46: Triangle FS aperture geometry for 6 MV (a) crossline and (b) inline profile comparisons with the γ-index criteria now passed.

Looking at the parameters in Table 4.9, the transmission parameter values for the X- and Y-jaws are higher compared to their benchmarked values. This is due to the fact that the MLC fluence is decreased and the fluence of the jaws needed to compensate for the loss in MLC fluence. To illustrate the differences between the benchmarked and final MLC and jaw parameters, 3D fluence maps were generated in the GUI and shown in Fig. 4.47 for a 10×10 cm^2 jaws FS, with the MLC closed. The MLC is unable to close completely, leaving a gap of 6 mm between the MLC edges. In Fig. 4.47 (a) the MLC fluence maps generated using the benchmarked parameters creates pronounced interleaf leakage, which is not visible in Fig. 4.47 (b) after adjustment of source parameters.

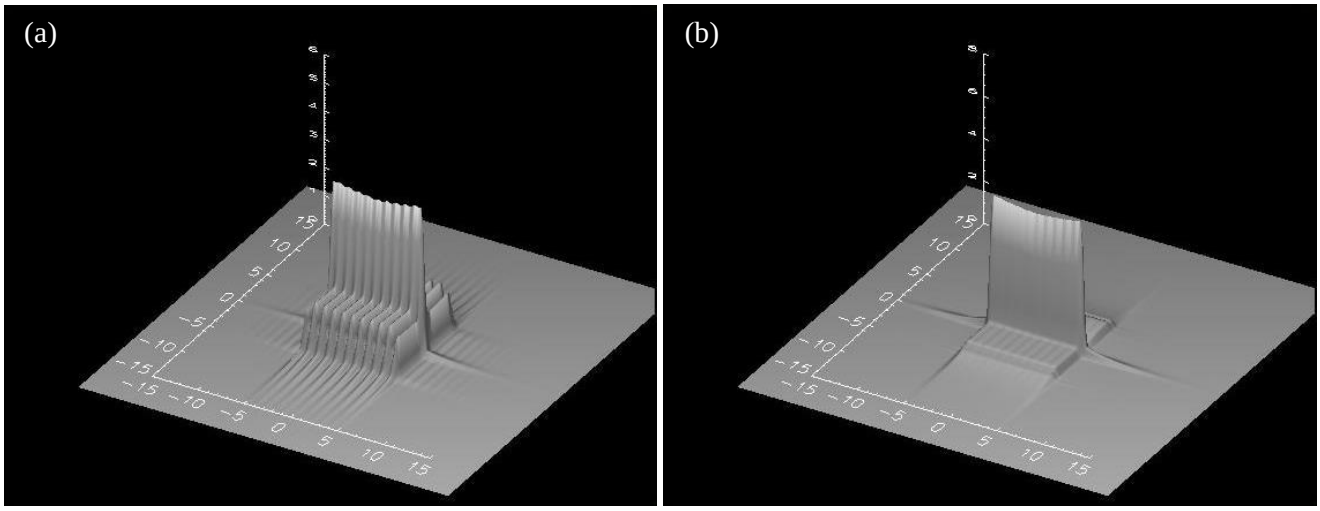

Fig. 4.47: 3D fluence maps generated in the GUI for a 10×10 cm^2 jaws FS, with all the MLC closed to leave a 6 mm gap, using the (a) benchmarked and (b) final parameter values.

B. Arrow field

Fig. 4.48 (a) and (b) shows the scanned film image and sagittal slice in *mcshow* for the *Arrow* FS aperture for the 8 MV beam.

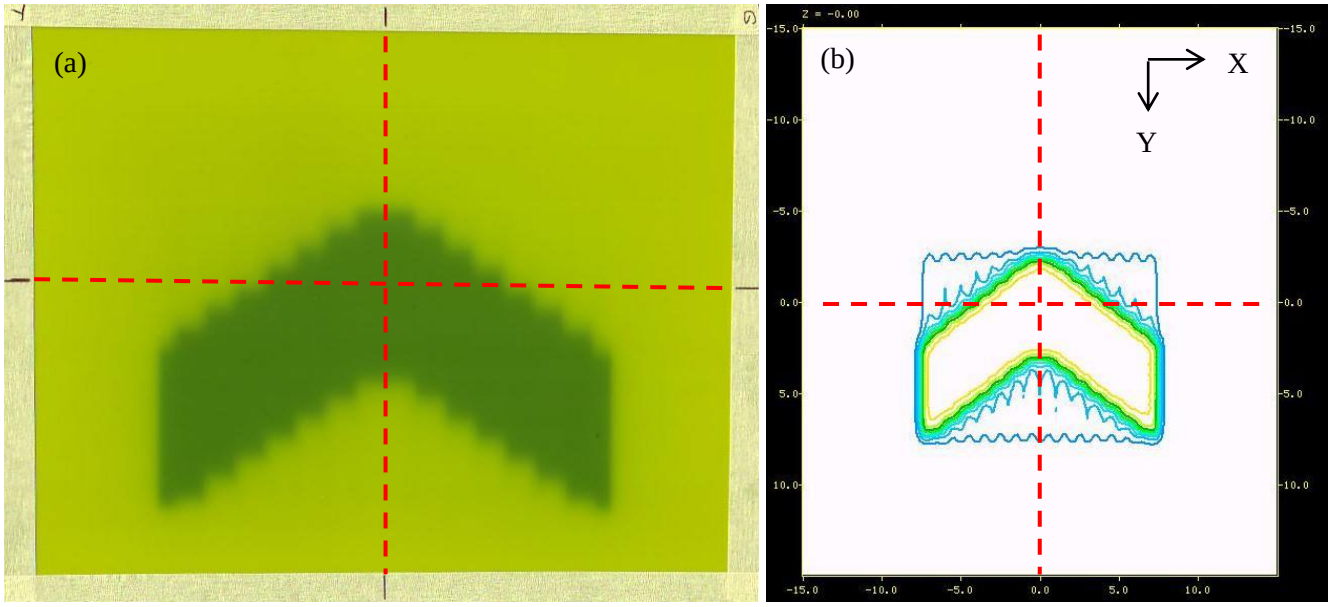

Fig. 4.48: Arrow shaped FS for 8 MV: (a) film OD before conversion to dose; (b) sagittal slice at CAX displays in *mcshow*.

Fig. 4.49 (a) and (b) shows the crossline and inline comparison profiles after adjustments were made to the *sigmax_mlc*, *sigmay_mlc*, *trans_mlc*, *trans_jaws_X* and *trans_jaws*_Y parameters, using the parameter values from Table 4.9.

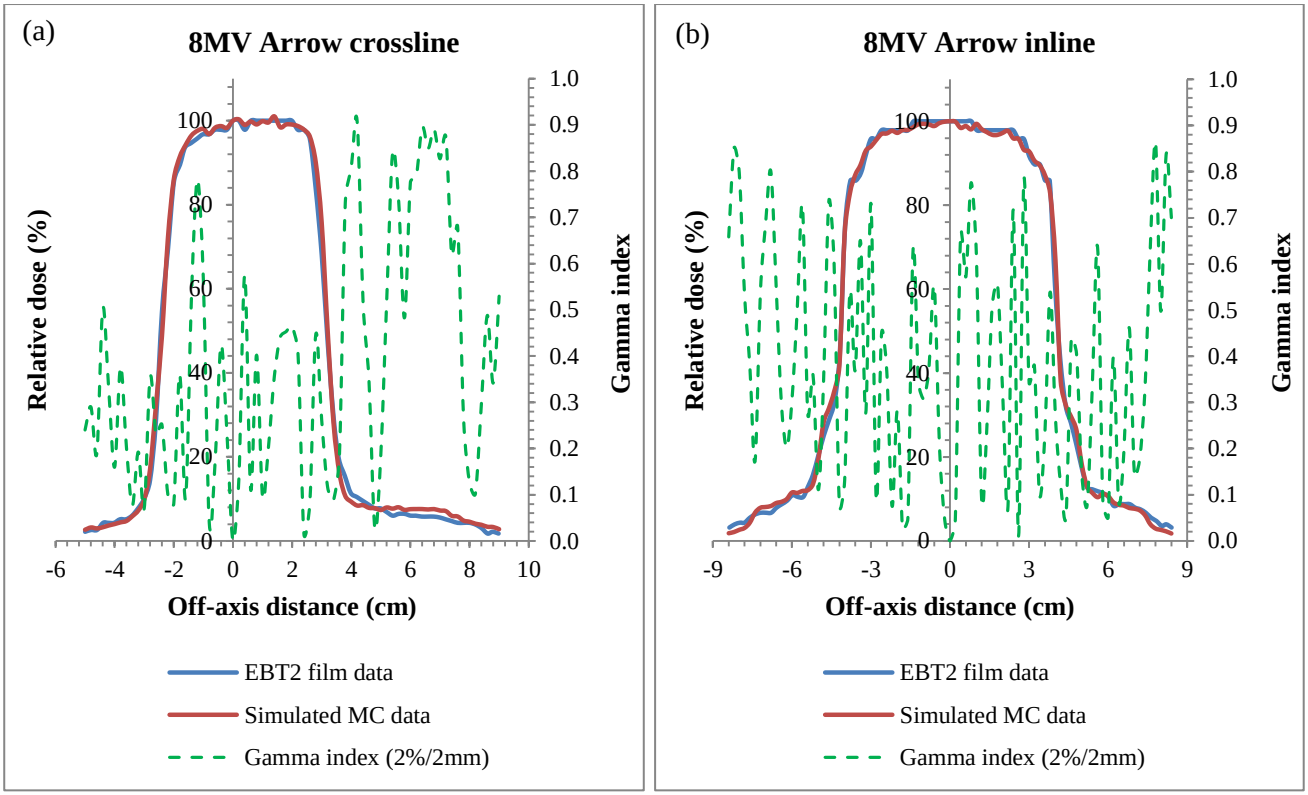

Fig. 4.49: Arrow shaped FS for 8 MV (a) crossline and (b) inline profile comparisons with the γ-index criteria of 2 % / 2 mm passed.

C. Mirror E field

Fig. 4.50 (a) and (b) shows the scanned film image and sagittal slice in *mcshow* for the *Mirror E* FS aperture respectively for the 15 MV beam.

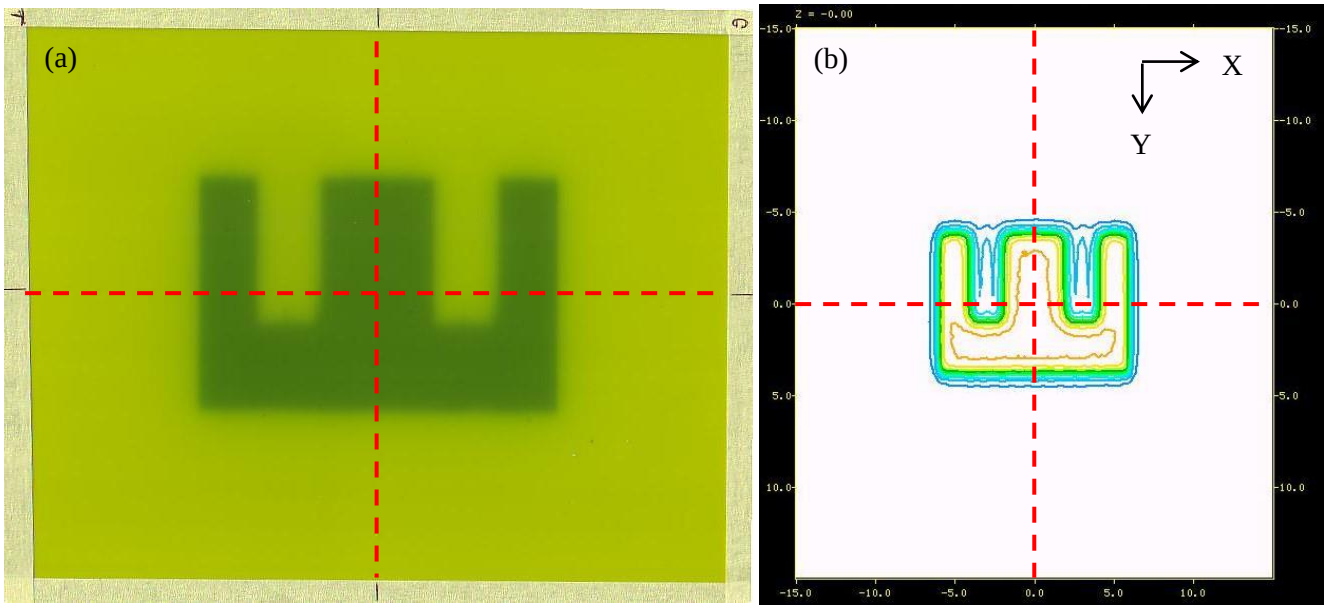

Fig. 4.50: Mirror E shaped FS for 15 MV: (a) film OD before conversion to dose; (b) sagittal slice at CAX displays in *mcshow*.

Fig. 4.51 (a) and (b) shows the final crossline and inline comparison profiles after adjustments were made to the *sigmax_mlc*, *sigmay_mlc*, *trans_mlc*, *trans_jaws_X* and *trans_jaws*_Y parameters, using the parameter values from Table 4.9.

From the results for the irregular geometries with the final MLC and jaw parameter values one can conclude that the model performs satisfactorily up to the conditions over which it was tested. For more accurate analysis, 3D comparison can be performed. The single crossline and inline profiles did however indicate the differences in dose below the MLC's and guided the adjustments to the source model leading to final parameters as shown in Table 4.9. The accuracy of the comparison also depends on the film dose conversion, where the film pieces used for the calibration and measurements are simultaneously scanned and aligned correctly in order to produce the correct calibration curve, and the characteristics of the scanner like uniformity, etc. This will ensure that the reference dose data obtained from the film is stable and reproducible.

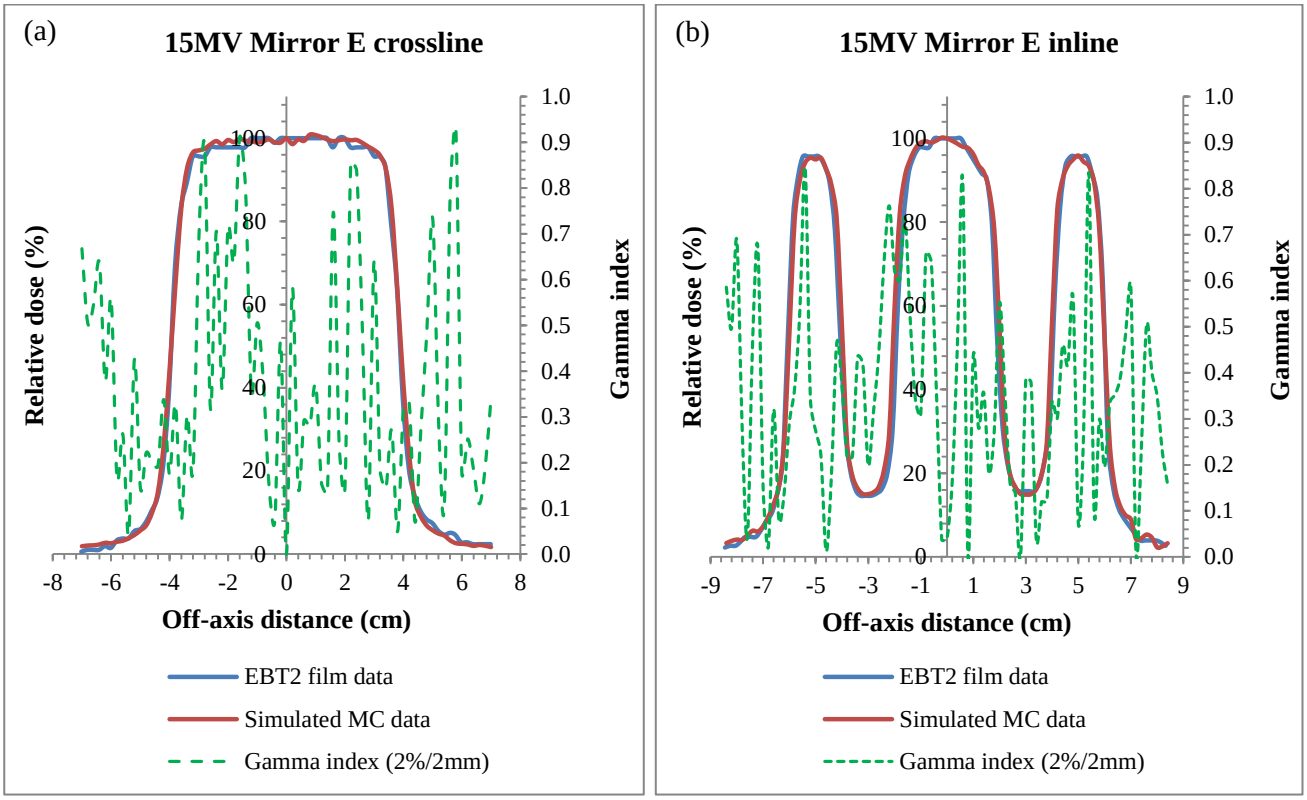

Fig. 4.51: Mirror E FS aperture geometry for 15 MV (a) crossline and (b) inline profile comparisons with the γ-index criteria passed.

With the MLC fluence parameters adjusted and set, the transmission parameter values for the X- and Y-jaws were increased, as seen in Table 4.9. At this stage, the benchmarked jaw and MLC parameter values are used for the square, rectangular and off-set geometries, with the final jaw and MLC parameter values used for the irregular geometries.

4.2.5: Output factors

Due to the fact that the source model cannot simulate scatter from different parts of the Linac head explicitly, output factors (OF's), which are necessary for MU calculations, had to be measured.

4.2.5.1 Large field size OF values

The OF for the large fields are displayed in Table 4.10.

Table 4.10: OF for 6, 8 and 15 MV photon energies for the Linac under consideration.

Square FS (cm^2)	6 MV	8 MV	15 MV
4×4	0.879	0.887	0.895
5×5	0.906	0.912	0.923
6×6	0.930	0.936	0.944
8×8	0.969	0.971	0.976
10×10	1.000	1.000	1.000
12×12	1.025	1.023	1.019
15×15	1.056	1.050	1.041
20×20	1.097	1.086	1.068
25×25	1.122	1.109	1.085
30×30	1.142	1.129	1.100
35×35	1.154	1.140	1.108
40×40	1.160	1.147	1.112

4.2.5.2 Small field size OF values

Pixel values from the irradiated small FS film pieces were converted to absorbed dose and are displayed in Tables 4.11 – 4.13 for 6, 8 and 15 MV energy beams respectively. In the tables, the difference between the dose value for the energy under consideration and the average dose over all three energies are presented. However, the OF's differ with 5%, 3% and 1% between the calibration curves for the 6, 8 and 15 MV energy beams respectively. The largest difference is observed for the 1×1 cm^2 FS over all energies. The red pixel values in Tables 4.11 – 4.13 ranges between 140.26 and 161.00 for the same dose value, as shown in Fig. 4.44 (indicated by red dashed box). This results in dose differences for the same pixel value over different beam energies. A weak energy dependency of the EBT2 film is responsible for this.

Table 4.11: OF data calculated for energy-specific dose and average dose data for 6 MV beams.

Square FS (cm^2)	Red pixel value	Absorbed Dose (cGy)		Output Factor	
		6 MV Cal. Curve	Ave. Cal. Curve	6 MV Cal. Curve	Ave. Cal. Curve
1×1	140.74	57.35	42.43	0.632	0.606
2×2	149.32	72.70	54.96	0.801	0.785
3×3	150.61	75.84	57.55	0.836	0.822
4×4	151.60	78.87	58.71	0.869	0.839
5×5	153.75	81.69	62.42	0.901	0.892
10×10	157.84	90.71	69.99	1.000	1.000

Table 4.12: OF data calculated for energy-specific dose and average dose data for 8 MV beams.

Square FS (cm^2)	Red pixel value	Absorbed Dose (cGy)		Output Factor	
		8 MV Cal. Curve	Ave. Cal. Curve	8 MV Cal. Curve	Ave. Cal. Curve
1×1	140.26	51.66	41.79	0.612	0.594
2×2	150.79	69.53	57.35	0.824	0.815
3×3	152.14	72.13	59.62	0.855	0.847
4×4	153.28	74.38	61.59	0.881	0.875
5×5	154.27	76.39	63.35	0.905	0.900
10×10	158.03	84.39	70.36	1.000	1.000

Table 4.13: OF data calculated for energy-specific dose and average dose data for 15 MV beams.

Square FS (cm^2)	Red pixel value	Dose (cGy)		Output Factor	
		15 MV Cal. Curve	Ave. Cal. Curve	15 MV Cal. Curve	Ave. Cal. Curve
1×1	141.14	47.00	42.96	0.568	0.563
2×2	151.73	64.15	58.93	0.775	0.772
3×3	155.99	72.26	66.48	0.873	0.871
4×4	156.84	73.97	68.08	0.893	0.892
5×5	157.65	75.63	69.62	0.913	0.912
10×10	161.00	82.81	76.31	1.000	1.000

Fig. 4.52 displays the OF's for the small fields, using each individual energy beam's calibration curve, along with the large FS's data.

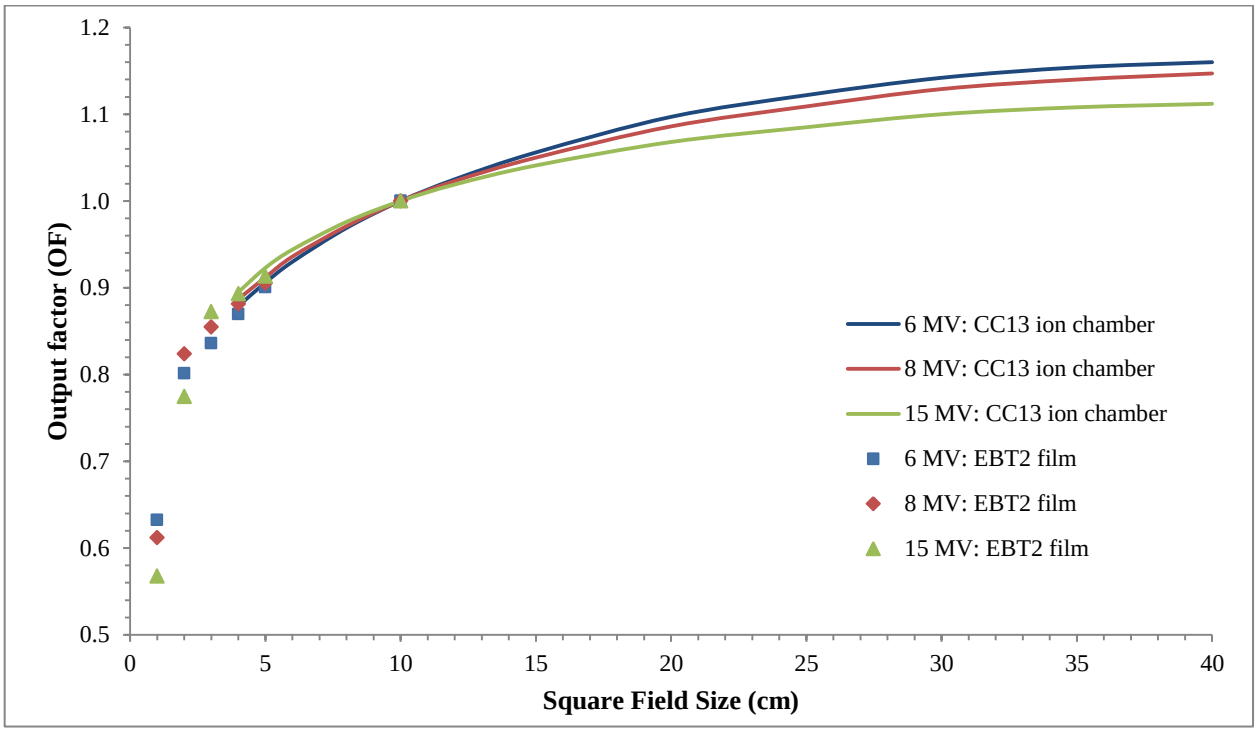

Fig. 4.52: Output factors for the 6, 8 and 15 MV photon energy beams; CC13 ionization chamber was used for the large fields and EBT2 film for small fields.

Chapter 5 – Conclusion

The primary focus of this study was to continue the development and test a MC particle source model for an Elekta^{TM} Precise Linac. In order to investigate the effectiveness and accuracy of the model, a film dosimetry procedure was developed using GAFCHROMIC® EBT2 film, since it is the first time it's been used in this institution. This formed part of the first objective of the project. A flatbed document scanner was used to digitize exposed EBT2 film; properties like scanner uniformity, film orientation, film scanning side and repeatability were investigated. This was done to establish the influence of these properties on the uncertainty of the scanned data results. The scanner uniformity was approximately 1 % over the total scanning area. The influence of film orientation from portrait to landscape was found to vary by 3.5 %, which can influence the results significantly. The effect of scanning side and scanner repeatability were found to be less than 1 % each, thus producing negligible differences. Film orientation was the most influential property to be considered in film dosimetry. Therefore it is recommended that the orientation of all films should be the same. Calibration films were also scanned in the same location to avoid uniformity variation. Since only the repeatability was the remaining factor it was assumed that the uncertainty due to the scanner was 1 %. The EBT2 film uncertainty was taken as 1 % as well, leading to the lower limit for γ-index criterion of 2 % / 2 mm for film and MC data comparison.

The second objective of the study involved the determination of the source model parameters with the aid of the developed IDL GUI. As explained previously, this GUI can calculate the exit fluence at a reference plane at a predefined distance from the target. The source model parameter values, which were obtained for square fields, produced satisfactory comparisons for symmetrical geometries, which include other square and rectangular fields. A γ-index evaluation criterion of 2 % / 2 mm was used for all comparisons. This lower limit was set since the MC simulations were run until a 1 % variance was reached in the useful part of the beam, and the WT measurement data also had a 1 %

noise component. For asymmetrical geometries, e.g. off-set apertures, the model performed well for small and medium size fields. However, while the model fitted the larger fields it failed at the edges where a few dose points failed the γ-index criterion. Finally, dose distributions for irregular FS apertures were simulated and measured to evaluate the MLC parameters of the model. Initially, the fluence was overestimated beneath the MLC's, which meant that the MLC parameters were adjusted until the evaluation criterion was met.

As part of the third objective of the study, dose distributions were measured and compared with MC simulations, especially for irregular MLC shaped fields. The three cases discussed in the study, namely the *Triangle*, *Arrow* and *Mirror E*, showed that a fix set of penumbra modelling parameters and transmission levels can yield accurate results compared with film dosimetry. The goal was to have a few variable source parameters for a range of fields for a specific energy, to keep the source model simple. However, the model could not replicate the field edges for large fields in all the off-axis cases. The model has variable collimator jaw transmission parameters to model beam penumbra and out-of-field dose for field sizes ranging from 1×1 to 40×40 cm^2. This can be regarded as a short-coming in the model, as the model makes use of a single point source for photons and contamination electrons. The model also cannot calculate OF's accurately. The model thus requires extra-focal scatter sources to model the field edges of the off-axis cases accurately. This will in turn increase the complexity of the model.

No wedges were modelled and validated in this study. This was due the fact that the aim of this project was to use the model for IMRT patient verification, with wedge fields not present in IMRT planning. A short-coming of the project is that the model was not validated clinically; where a patient's CT data are used to simulate a prescribed dose and to compare it with the TPS's dose distribution. This can be regarded as a topic for future studies and to continue the development of the model. It is also important for future studies to expand the model to include scatter from the head components. This will in turn improve the accuracy of the asymmetrical fields which struggled with the larger field edges.

References

1: Glasser O. *Wilhelm Conrad Röntgen and the early history of the roentgen rays.* Norman Publishing, p. 10-15 (1934)

2: Fraass B A. *The development of conformal radiation therapy.* Medical Physics, Vol. **22**, No. 11 Pt. 2, p. 1911-1921 (1995)

3: Webb S. *Intensity-Modulated Radiation Therapy.* Series in Medical Physics, Institute of Physics Publishing, Philadelphia, USA (2001)

4: Rana S. *Intensity modulated radiation therapy versus volumetric intensity modulated arc therapy.* Journal of Medical Radiation Sciences, Vol. **60**, No. 3, p. 81-83 (2013)

5: Dunscombe P, Arsenault C, Bissonnette J P, Johnson H, Mawko G and Seuntjens J. *The development of quality control standards for radiation therapy equipment in Canada*. Journal of Applied Clinical Medical Physics, Vol. **8**, No. 1, p. 108-118 (2007)

6: Khan F M, Pine J, Standen M, Kairis L R, Boyce T and Rivera B. *The Physics of Radiation Therapy, Third Edition.* Chapter 20: Intensity-Modulated Radiation Therapy, p. 482-506. Williams & Wilkins, Baltimore, USA (2003)

7: Ahmad S, Young J, Syzek E, Herman T D L, Schnell E, Hildebrand K, Algan Ö and Herman T. *Dosimetric comparison between IMRT delivery modes: Step-and-shoot, sliding window, and volumetric modulated arc therapy – for whole pelvic radiation therapy of intermediate-to-high risk prostate adenocarcinoma.* Journal of Medical Physics, Vol. **38**, No. 4, p. 165-172 (2013)

8: Tan Y I, Metwaly M, Glegg M, Baggarley S and Elliott A. *Evaluation of six TPS algorithms in computing entrance and exit doses.* Journal of Applied Clinical Medical Physics, Vol. **15**, No. 3, p. 229-240 (2014)

9: Arnfield M R, Siantar C H, Siebers J, Garmon P, Cox L and Mohan R. *The impact of electron transport on the accuracy of computed dose.* Medical Physics, Vol. **27**, No. 6, p. 1266-1274 (2000)

10: Wang L, Chui C S and Loverock M. *A patient specific Monte Carlo dose-calculation method for photon beams.* Medical Physics, Vol. **25**, No. 6, p. 867-878 (1998)

11: Ahnesjõ A, Andreo P and Brahme A. *Calculation and application of point spread functions for treatment planning with high energy photon beams.* Acta Oncologica, Vol. **26**, p. 49-56 (1987)

12: Mohan R, Chui C and Lidofsky L. *Differential pencil beam dose computation model for photons.* Medical Physics, Vol. **13**, No. 1, p. 64-73 (1986)

13: Mackie T R, Scrimger J W and Battista J J. *A convolution method of calculating dose for 15 MV x-rays.* Medical Physics, Vol. **12**, No. 2, p. 188-196 (1985)

14: Vanderstraeten B, Reynaert N, Paelinck L, Madani I, De Wagter C, De Gersem W, De Neve W and Thierens H. *Accuracy of patient dose calculation for lung IMRT: A comparison of Monte Carlo, convolution/superposition, and pencil beam computations.* Medical Physics, Vol. **33**, No. 9, p. 3149-3158 (2006)

15: Van Esch A, Tillikainen L, Pyykkonen J, Tenhunen M, Helminen H, Siljamäki S, Alakuijala J, Paiusco M, Lori M and Huyskens D P. *Testing of the analytical anisotropic algorithm for photon dose calculation.* Medical Physics, Vol. **33**, No. 11, p. 4130-4148 (2006)

16: Fogliata A, Nicolini G, Vanetti E, Clivio A and Cozzi L. *Dosimetric validation of the anisotropic analytical algorithm for photon dose calculation; fundamental characterization in water.* Physics in Medicine and Biology, Vol. **51**, No. 6, p. 1421-1438 (2006)

17: Ahnesjõ A. *Collapsed cone convolution of radiant energy for photon dose calculation in heterogeneous media.* Medical Physics, Vol. **16**, No. 4, p. 577-592 (1989)

18: Hissoiny S, Bouchard H, Ozell B and Després P. *GPUMCD: a new GPU-oriented Monte Carlo dose calculation platform*. Medical Physics, Vol. **38**, No. 2, p. 754-782 (2011)

19: Adeel A. *Handbook of Radiotherapy Physics: Theory and Practice.* Chapter 5: The Monte Carlo Simulation of Radiation Transport, p. 75-87. Taylor & Francis Group, LLC. USA (2007)

20: Sarrut D, Bardiès M, Boussion N, Freud N, Jan S, Létang J-M, Loudos G, Maigne L, Marcatili S, Mauxion T, Papadimitroulas P, Perrot Y, Pietrzyk U, Robert C, Schaart D R, Visvikis D and Buvat I. *A review of the use and potential of the GATE Monte Carlo simulation code for radiation therapy and dosimetry applications.* Medical Physics, Vol. **41**, No. 6, p. 064301 (2014)

21: Ferrari A, Sala P R, Fasso A and Ranft J. *FLUKA: a multi-purpose transport code.* CERN 2005 (10), INFN/TC 05/11, SLAC-R-773 (2005)

22: Hofmann W, Winkler-Heil R, Truta L A and Tschiersch J. *Application of a Monte Carlo lung dosimetry code to the inhalation of thoron progeny.* Radiation Protection Dosimetry, Vol. **160**, No. 1-3, p. 96-99 (2013)

23: Salvat J, Fernández-Varea J M and Sempau J. *PENELOPE-2011: A Code System for Monte Carlo Simulation of Electron and Photon Transport.* Organization for Economic Co-operation and Development: Nuclear Energy Agency (2011)

24: Taylor R E P, Yegin G and Rogers D W O. *Benchmarking brachydose: Voxel based EGSnrc Monte Carlo calculations of TG-43 dosimetry parameters.* Medical Physics, Vol. **34**, No. 2, p. 445-457 (2007)

25: Ma C-M and Rogers D W O. *BEAMDP Users Manual.* Ionizing Radiation Standards National Research Council of Canada (NRCC), Ottawa. Report PIRS-0509 (C) rev A, (last edited: September 21, 2006)

26: Rogers D W O, Walters B and Kawrakow I. *BEAMnrc Users Manual*. Ionizing Radiation Standards National Research Council of Canada (NRCC), Ottawa. Report PIRS-0509 (A) rev K, (last edited: September 27, 2006)

27: Walters B, Kawrakow I and Rogers D W O. *DOSXYZnrc Users Manual*. Ionizing Radiation Standards National Research Council of Canada (NRCC), Ottawa. Report PIRS-794 rev B, (last edited: September 21, 2006)

28: Nelson W R and Namito Y. *The EGS4 Code System: Solution of Gamma-ray and Electron Transport Problems.* Stanford Linear Accelerator Centre (SLAC), Stanford University, Stanford, California, USA. SLAC PUB 5193 (February 9, 1990)

29: Tyagi N, Moran J M, Litzenberg D W, Bielajew A F, Fraass B A and Chetty I J. *Experimental verification of a Monte Carlo-based MLC simulation model for IMRT dose calculation.* Medical Physics, Vol. 34, No. 2, p. 651-663 (2007)

30: Sikora M, Dohm O and Alber M. *A virtual photon source model of an Elekta linear accelerator with integrated mini MLC for Monte Carlo based IMRT dose calculation.* Physics in Medicine and Biology, Vol. 52, p. 4449-4463 (2007)

31: Liu H H, Mackie T R and McCullough E C. *A dual source photon beam model used in convolution/superposition dose calculations for clinical megavoltage x-ray beams.* Medical Physics, Vol. **24**, No. 12, p. 1960-1974 (1997)

32: Cho W, Kielar K N, Mok E, Xing L, Park J-H, Jung W-G and Suh T-S. *Multisource modeling of flattening filter free (FFF) beam and the optimization of model parameters.* Medical Physics, Vol. **38**, No. 4, p. 1931-1942 (2011)

33: Yan G, Liu C, Lu B, Palta J R and Li J G. *Comparison of analytic source models for head scatter factor calculations and planar dose calculation for IMRT*. Physics in Medicine and Biology, Vol. **53**, No. 8, p. 2051-2067 (2008)

34: Chetty I J, Curran B, Cygler J E, DeMarco J J, Ezzell G, Faddegon B A, Kawrakow I, Keall P J, Liu H, Ma C-M, Rogers D W O, Seuntjens J, Sheikh-Bagheri D and Siebers J V. *Report of the AAPM Task Group No. 105: Issues associated with clinical implementation of Monte Carlo-based photon and electron external beam treatment planning.* Medical Physics, Vol. **34**, No. 12, p. 4818-4853 (2007)

35: Healy B J and Murry R I. *Testing of a treatment planning system with beam data from IAEA TECDOC 1540*. Journal of Medical Physics, Vol. **36**, No. 2, p. 107 (2011)

36: International Specialty Products (ISP) Corporation. *GAFCHROMIC® EBT2: Self-developing film for Radiotherapy Dosimetry.* Wayne, NJ, USA (February 19, 2009)

37: Arjomandy B, Tailor R, Zhao L and Devic S. *EBT2 film as a depth-dose measurement tool for radiotherapy beams over a wide range of energies and modalities.* Medical Physics, Vol. **39**, No. 2, p. 912-921 (2012)

38: Kairn T, Hardcastle N, Kenny J, Meldrum R, Tomé WA and Aland T. *EBT2 radiochromic film for quality assurance of complex IMRT treatments of the prostate: micro-collimated IMRT, RapidArc and Tomotherapy.* Australasian Physical & Engineering Sciences in Medicine, Vol. **34**, No. 3, p. 333-343 (2011)

39: 62A, IEC TC/SC. *IEC 60601-1-6 Ed. 1.0 b: 2004, Medical electrical equipment – Part 1-6: General requirements for safety – Collateral standard: Utility.* Multiple. Distributed through American National Standards Institute (2007)

40: Townson R W, Jia X, Tian Z, Graves Y J, Zavgorodni S and Jiang S B. *GPU-based Monte Carlo radiotherapy dose calculation using phase-space sources.* Physics in Medicine and Biology, Vol. **58**, No. 12, p. 4341-4356 (2013)

41: Desobry G E and Boyer A L. *Bremsstrahlung review: an analysis of the Schiff spectrum*. Medical Physics, Vol. **18**, No. 3, p. 497-505 (1991)

42: Patridge M. *Reconstruction of Megavoltage photon spectra from electronic portal imager derived transmission measurements.* Physics in Medicine and Biology, Vol. **45**, p. N115 – N131 (2000)

43: National Institute of Standards and Technology. *NIST: X-ray mass attenuation coefficients – Tungsten.* Accessed on: http://physics.nist.gov/PhysRefData/XrayMassCoef/ElemTab/z74.html on 24 May 2009

44: National Institute of Standards and Technology. *NIST: X-ray mass attenuation coefficients – Iron.* Accessed on: http://physics.nist.gov/PhysRefData/XrayMassCoef/ElemTab/z26.html on 24 May 2009

45: Brooks R A, Chiro G D. *Beam hardening in X-ray reconstructive tomography.* Physics in Medicine and Biology, Vol. **21**, p. 390-398 **(**1976)

46: International Atomic Energy Agency (IAEA). *Radiation Oncology Physics: A Handbook for Teachers and Students.* Vienna, Austria (2005)

47: Khan F M, Higgins P D. *Field equivalence for clinical electron beams.* Physics in Medicine and Biology, Vol. **46**, p. N9–N14 **(**2001)

48: Bielajew A F. *Fundamentals of the Monte Carlo method for neutral and charged particle transport.* Ann Arbor, Michigan, USA (2000)

49: Kawrakow I and Rogers D W O. *The EGSnrc Code System: Monte Carlo Simulation of Electron and Photon Transport.* (2003)

50: Seco J and Verhaegen F. *Monte Carlo Techniques in Radiation Therapy.* CRC Press (2013)

51: Metcalfe P, Kron T and Hoban P. *The Physics of Radiotherapy X-rays from Linear Accelerators.* Medical Physics Publishing Corporation (1997)

52: Jabbari K. *Review of Fast Monte Carlo Codes for Dose Calculation in Radiation Therapy Treatment Planning.* Journal of Medical Signals and Sensors, Vol. **1**, No. 1, p. 73-86 (2011)

53: Bielajew A F and Rogers D W O. *PRESTA: The Parameter Reduced Electron-Step Transport Algorithm for Electron Monte Carlo Transport.* Nuclear Instruments and Methods in Physics Research, Vol. **B18**, p. 165-181 (1987)

54: James F. *A review of pseudorandom number generators*. Computer Physics Communications, Vol. **60**, p. 329-344 (1990)

55: Hongo K, Maezono R and Miura K. *Random number generators tested on quantum Monte Carlo simulations.* Journal of Computational Chemistry, Vol. **31**, No. 11, p. 2186-2194 (2010)

56: Hongo K and Maezono R. *Quantum Monte Carlo Simulations with RANLUX Random Number Generator*. Progress in Nuclear Science and Technology, Vol. **2**, p. 51-55 (2011)

57: Lippuner J and Elbakri I A. *A GPU implementation of EGSnrc's Monte Carlo photon transport for imaging applications.* Physics in Medicine and Biology, Vol. **56**, No. 22, p. 7145-7162 (2011)

58: Aluru S. *Lagged Fibonacci Random Number Generators for Distributed Memory Parallel Computers.* Journal of Parallel and Distributing Computers, Vol. **45**, No. 1, p. 1-12 (1997)

59: Ljungberg M, Strand S-E and King M A. *Monte Carlo Calculations in Nuclear Medicine, Second Edition: Applications in Diagnostic Imaging.* CRC Press (2012)

60: Rogers D W O and Bielajew A F. *Monte Carlo Techniques of Electron and Photon Transport for Radiation Dosimetry.* National Research Council of Canada Ottawa, Canada. K1A OR6 (1990)

61: Ju T, Simpson T, Deasy J O and Low D A. *Geometric interpretation of the γ dose distribution comparison technique: Interpolation-free calculation*. Medical Physics, Vol. **35**, No. 3, p. 879-887 (March 2008)

62: Low D. *Gamma Dose Distribution Evaluation Tool.* Journal of Physics: Conference Series, Vol. **250**, No. 1, p. 012071 (2010)

63: Collins TJ. *ImageJ for Microscopy.* BioTechniques **43** (1 Suppl): 25–30 (July 2007)

64: Chang L, Chui C-S, Ding, H-J, Hwang, I-M and Ho S-Y. *Calibration of EBT2 film by the PDD method with scanner non-uniform correction.* Physics in Medicine and Biology, Vol. **58**, No. 18, p. 5875-5887 (2012)

65: Park S, Kang S-K, Cheong K-H, Hwang T, Kim H, Han T, Lee M-Y, Kim K, Bae H, Su Kim H, Han Kim J, Jae Oh, S and Suh J-S. *Variations in dose distribution and optical properties of Gafchromic™ EBT2 film according to scanning mode.* Medical Physics, Vol. **39**, No. 5, p. 2524-2535 (2012)

66: Fanning DW. *IDL Programming Techniques, 2nd Edition.* Fort Collins, USA (2000)

67: Georg D, Olofsson J, Künzler T and Karlsson M. *On empirical methods to determine scatter factors for irregular MLC shaped beams.* Medical Physics, Vol. **31,** No. 8, p. 2222-2229 (2004)

68: Fujita Y, Tohyama N, Myojoyama A and Saitoh H. *Depth Scaling of Solid Phantom for Intensity Modulated Radiotherapy Beams.* Journal of Radiation Research, Vol. **51**, No. 6, p. 707-713 (2010)

69: Ma C-M, Li J S, Pawlicki T, Jiang S B, Deng J, Lee M C, Koumrian T, Luxton M and Brain S. *A Monte Carlo dose calculation tool for radiotherapy treatment planning.* Physics in Medicine and Biology, Vol. **47**, No. 10, p. 1671-1689 (2002)

70: Vaught A. *Graphing with Gnuplot and Xmgr*. Linux Journal, (1 Aug 1998) http://www.linuxjournal.com/article/1218 (article accessed on 13 Nov 2014)

71: Aldrich J. *Doing Least Squares: Perspectives from Gauss and Yule.* International Statistical Review, Vol. **66**, No. 1, p. 61-81 (1998)

72: Butson M J, Yu P K N, Cheung T and Alnawaf H. *Energy response of the new EBT2 radiochromic film to x-ray radiation.* Radiation Measurements, Vol. **45**, p. 836-839 (2010)

Summary

Introduction & Aim

Linear accelerators (Linacs) produce megavoltage (MV) energy photon and electron beams to irradiate tumour volumes in patients. More complex field shapes can be setup quickly with multileaf collimators (MLC's), thus more advanced treatments like intensity-modulated radiation therapy (IMRT) are possible. This is one of the reasons why treatment planning models should be accurately commissioned and accurate dose calculation algorithms employed. Monte Carlo (MC) based dose calculations are very suitable to solve this issue. The aim of this project was to continue the development of an X-ray source model for MC dose calculations for an Elekta^{TM} Precise MLC Linac.

Methods & Materials

An in-house developed graphical user interface (GUI) was used to calculate exit fluence based on a mathematical model and energy spectra derived from the Schiff formula. This produced an input source file for source number 4 in the DOSXYZnrc code. DOSXYZnrc was used to calculate X-ray dose distributions in water and RW3 solid water phantoms. These dose distributions were compared to actual measured film or water tank dose data. A gamma (γ) index was calculated to compare the MC and measured dose. The criteria used for the γ-index was 2 % dose / 2 mm distance-to-agreement. Dose distribution data for square, rectangular and off-set fields were compared.

Results & Discussion

Prior to source commissioning a GAFCHROMIC® EBT2 film dosimetry system, that entails using a film scanner, was setup. With the use of the EBT2 film, scanner properties like scanner uniformity, film orientation, film scanning side and repeatability were investigated. Film orientation produced the largest discrepancy of 3.5 % between portrait and landscape orientation. The remaining properties were within 1 % variation. A range of fields for 6, 8 and 15 MV beams were modelled, simulated and

compared to corresponding measured water tank data. Parameters in the MC source model were adjusted until the γ-index criteria were met for each comparison. These source parameter values were retained for further more complex field simulation and evaluation against measurements. Rectangular, small and medium sized off-set fields met the γ-index criteria. For off-set fields greater than 15×15 cm^2, the model failed the criteria at some dose points at the field edges. The jaws and MLC transmission parameters required adjustments for the irregular MLC field shapes comparisons.

Conclusion

The source model performed well and can be employed for dose verification ranging from simple regular fields to conformal treatments. In order to use the model for IMRT treatment verification, the model needs to be validated clinically. The only requirement is that Linac scatter factors must be measured separately to calculate the correct amount of monitor units necessary for patient treatment. Additional scatter sources can be implemented in the model to increase the accuracy at the field edges of the off-axis cases, which will require verification.

Keywords: Source model, Monte Carlo simulations, linear accelerator, multileaf collimators, GAFCHROMIC® EBT2 film, intensity-modulated radiation therapy

Opsomming

Inleiding & Doel

Lineêre versnellers produseer megavolt (MV) energie foton en elektron bundels om tumor volumes in pasiënte te bestraal. Meer komplekse behandelingsvelde kan vinnig opgestel word deur gebruik te maak van veelsegment kollimatore (VSK's), om sodoende meer gevorderde behandelings, soos intensiteit-gemoduleerde bestraling (IGB), moontlik te maak. Dit is een van die redes waarom beplannings modelle so akkuraat as moontlik opgestel moet wees sodat akkurate dosis berekening algoritmes gebruik kan word. Monte Carlo (MC) gebaseerde dosis berekeninge is geskik om hierdie probleem op te los. Die doel van hierdie projek was om 'n X-straal bron model verder te ontwikkel vir MC gebaseerde dosis berekeninge vir 'n Elekta^{TM} Precise VSK lineêre versneller.

Metodes & Materiale

'n Plaaslik ontwikkelde grafiese gebruikerskoppelvlak was gebruik om uitgangs tydvloed te bereken, wat gebaseer is op 'n wiskundige model en energie spektra wat afgelei is vanaf die Schiff formule. Dit het 'n invoer bron lêer geskep vir bron nommer 4 in die DOSXYZnrc kode. DOSXYZnrc was gebruik om X-straal dosis verspreidings in water en RW3 soliede water fantome te bereken. Hierdie dosis verspreidings was vergelyk met gemete film of watertenk dosis data. 'n Gamma (γ) indeks was bereken om die MC en gemete dosis met mekaar te vergelyk. Die kriteria wat gebruik word vir die γ-indeks was 2 % dosis / 2 mm afstand-tot-ooreenkoms. Dosis verspreiding data vir vierkantige, reghoekige en ongesentreerde velde was vergelyk.

Resultate & Bespreking

Voordat die bron ingebruikneming begin is, is 'n GAFCHROMIC® EBT2 film dosimetrie stelsel opgestel wat die gebruik van 'n film skandeerder behels. Met die gebruik van die EBT2 film, is skandeerder eienskappe soos skandeerder eenvormigheid, film oriëntasie, film skanderings kant en

herhaalbaarheid ondersoek. Film oriëntasie het die grootste verskil gelewer van 3.5 % tussen portret en landskap-oriëntasie. Die oorblywende eienskappe was binne 1 % variasie. ‘n Verskeidenheid van velde vir 6, 8 en 15 MV bundels was gemodelleer, gesimuleer en vergelyk met ooreenstemmende gemete watertenk data. Parameters in die MC bron model is aangepas totdat die γ-indeks kriteria vir elke vergelyking bevredig is. Hierdie bron parameter waardes is behou vir verdere komplekse veld simulasies en ge-evalueer teen ooreenstemmende metings. Reghoekige, klein en medium grootte ongesentreerde velde het die γ-indeks evaluering geslaag. Vir ongesentreerde velde groter as 15×15 cm^2, het die model nie die evaluering geslaag by sekere dosis punte op die veldrandte nie. Die kollimator en VSK transmissie parameters het aanpassings vereis vir onreëlmatige VSK grootte velde wat vergelyk was.

Gevolgtrekking

Die bron model het goed presteer en kan gebruik word vir dosis bevestiging wat wissel van eenvoudige gereelde velde tot konforme behandelings. Dit is belangrik om die model klinies te toets en te bekragtig om die model vir IGB behandelings te bevestig. Die enigste vereiste is dat die lineêre versneller verstrooings faktore afsonderlik gemeet moet word sodat die korrekte aantal monitor eenhede bereken word wat nodig is vir pasiënt behandeling. Bykomende verstrooings bronne kan in die model geïmplementeer word om die akkuraatheid van die ongesentreerde gevalle te verhoog, wat verdere bevestiging gaan vereis.

Sleutel woorde: Bron model, Monte Carlo simulasies, lineêre versneller, veelsegment kollimatore, GAFCHROMIC® EBT2 film, intensiteit-gemoduleerde bestraling

Acknowledgements

I would like to thank my supervisor, Dr Freek du Plessis, for his guidance during the course of the project. I have learned and gained knowledge and skills that is of great value. Also to my colleagues; Dr Willie Shaw, Mrs Dedri O'Reilly, Mr Lourens Strauss and Mr Itumeleng Setilo for their support throughout the duration of the project. They always made time to answer a question and give advice and assistance. Special thanks to retired Prof Casper Willemse who developed the IDL GUI and made it available for the department to use. This research project was funded by the South African Medical Research Council (MRC) with funds from National Treasury under its Economic Competitiveness and Support package.

I have great appreciation for the support and love from my fiancée, Dr Selma Basson. She never stopped believing in me and was always delighted in my progress and achievements. To my parents, Willie and Erika Smit, words cannot describe the appreciation I have for them. They always placed their children before themselves and always aspired to give the best for their children. They supported me unconditionally throughout my life. Also to my future parents-in-law, Poena and Melanie Basson, for their support.

Lastly but not least, I thank my Lord God Almighty. He granted me the knowledge and talents to be an example to others.